Summer 2020

Room Temperature Semiconductor Radiation Detectors Based on CdZnTe and CdZnTeSe

Mohsin Sajjad

ROOM TEMPERATURE SEMICONDUCTOR RADIATION DETECTORS BASED ON CDZNTE AND CDZNTESE

by

Mohsin Sajjad

Bachelor of Science
Bangladesh University of Engineering & Technology, 2012

Submitted in Partial Fulfillment of the Requirements

For the Degree of Doctor of Philosophy in

Electrical Engineering

College of Engineering and Computing

University of South Carolina

2020

Accepted by:

Krishna C. Mandal, Major Professor

Xiaofeng Wang, Committee Member

Seongtae Bae, Committee Member

Fanglin (Frank) Chen, Committee Member

Cheryl L. Addy, Vice Provost and Dean of the Graduate School

DEDICATION

I dedicate my research study to my loving parents, Muhammad Ali Khan and Chand Sultana for their love, endless guidance, and encouragement. To my wife, Dr. Rubaiya Jesmin for her constant care and love that helped me to complete this journey.

ACKNOWLEDGMENTS

I express my deep sense of gratitude to my advisor and committee chair, Professor Krishna C. Mandal for contributing his expert knowledge and stimulating discussions with him at every stage of this research. I would never have made this happen without his extremely valuable time, support, and guidance. My development within his research group has allowed me to undertake this work with the proper knowledge and skillset I otherwise would not have.

I would like to thank my Ph. D. committee members, Professors Xiaofeng Wang, Seongtae Bae, and Fanglin (Frank) Chen, for their guidance and constructive criticism.

I would also like to thank the following persons and programs for the contributions to the research performed in this work:

- Dr. Sandeep K. Chaudhuri, for his assistance in radiation measurements and digital pulse-shape analysis.
- Dr. Cihan Oner, whose guidance helped me to understand the details of crystal growth, surface preparation, and different characterizations.
- Joshua Kleppinger, who assisted me heavily to perform different tasks as a fellow lab member and shared a lot of knowledge regarding this research study.
- Dr. Stavros G. Karakalos, who performed the XPS characterization on the CZT and CZTS crystal samples.
- The Electron Microscopy Center at the University of South Carolina, for their assistance with SEM and EDS studies on the grown CZT and CZTS crystals.

- Nuclear Engineering University Program (NEUP) sponsored by U.S. Department of Energy, for providing me the necessary funding for doing this research.
- Support to Promote Advancement of Research and Creativity (SPARC) Graduate Research Grant sponsored by the Office of the Vice President for Research, for supporting the research with additional funding.

I would also like to thank my other fellow lab members, Dr. Rahmi O. Pak, Dr. Towhid A. Chowdhury, and OmerFaruk Karadavut for their support and friendship throughout this process.

ABSTRACT

In recent years, there have been considerable interests in nuclear radiation detectors for national security and nuclear safeguard including monitoring special nuclear materials and nuclear waste characterization, for medical imaging devices using nuclear medicine such as positron emission tomography (PET), and for NASA space astronomy. One of the most promising semiconductors being considered for the field-deployable nuclear detector is cadmium zinc telluride (CdZnTe or CZT). CZT is a ternary semiconductor that can efficiently stop and detect high-energy gamma-rays at room temperature. CZT has desirable properties for efficient nuclear radiation detection and imaging due to high atomic number (Z ~ 50, high stopping power), high density (5.8 g/cm^3), high resistivity ($\geq 10^{10}$ Ω-cm), wide bandgap (~1.6 eV at 300K), low leakage current, high gamma-ray absorption coefficient, and good electron transport properties. However, there are considerable difficulties in growing large volume, homogeneous, and defect-free CZT single crystals. These difficulties enhance the cost of CZT detectors for industrial mass-production. Furthermore, CZT suffers from poor hole transport properties, which creates significant problems as a high-energy gamma-ray detector.

In the present work, a comprehensive investigation is undertaken to develop a successful growth method for CZT at the University of South Carolina (UofSC). The method is called vertical Bridgman solvent-growth technique which reduces the complexity of growing detector-grade CZT single crystals at high temperature. The new

method we developed is a low-temperature growth using tellurium (Te) as a solvent while maintaining crystal homogeneity and took the advantages of other modern CZT growth techniques. Large diameter (up to 3.0-inch diameter and 4.8 inches in length) detector grade CZT boules (≥ 75% singularity) have been grown using in-house zone-refined precursor materials loaded into carbon-coated quartz ampoules. Ampoules were sealed under ultra-high vacuum and crystal growth was performed using temperature profiled furnaces built in-house at UofSC. The grown ingots were cut into wafers and chemo-mechanically polished for structural, optical, electrical, and spectroscopic characterization. The bulk resistivity of the as-grown crystal was found to be ~ 5×10^{10} Ω-cm from current-voltage (I-V) measurements. Infrared transmission imaging revealed an average tellurium inclusion size of < 8 microns. Nuclear radiation detectors were fabricated and characterized using analog and digital radiation detection systems integrated with front-end readout electronics developed at UofSC. Block of CZT crystals of dimensions ~20 × 20 × 5 mm^3 were used to fabricate detectors with 10 × 10 pixelated anode configuration integrated with inter-pixel guard rings and were tested for their radiation detection properties using 662 keV gamma rays from ^{137}Cs gamma sources. The pixels exhibited well-resolved gamma pulse-height spectra with energy resolution ~ 1.5% at 662 keV. A few pixels exhibited tailing of the photopeak on the lower energy side indicating the presence of hole traps. Biparametric plots (BP) were generated from digitally recorded pre-amplifier pulses. The BPs showed anomalous behavior, which was correlated to the gamma interactions in the active region of the detector. The biparametric plots also enabled to extract the pulse-height spectra free from the extensive tailing of the photopeak. A

Matlab software code was developed to apply correction schemes to the biparametric plots and to improve the results acquired from the detectors.

$Cd_xZn_{1-x}Te_ySe_{1-y}$ (CZTS) has emerged in the last couple of years as a next-generation high-yielding material for the fabrication of room temperature high energy gamma detection. We report for the first time, the hole transport property measurements in CZTS based gamma-ray detectors in planar configuration. I-V measurements revealed detector grade bulk resistivity and the fabricated detectors produced well-resolved 5486 keV alpha peaks, for both electrons and holes drifting alike, when PHS was recorded using a ^{241}Am radiation source. The PHS measurements enabled to measure the charge transport properties for both the charge-carriers. The mobility-lifetime product ($\mu\tau$) for electrons and holes were calculated using a single-polarity Hecht plot regression method. The pre-amplifier pulses were recorded and processed digitally to obtain electron and hole drift mobilities using a time-of-flight method. The measured transport properties indicated the hole lifetime to be greater than the electron lifetime by a factor of ~1.5. Gamma-ray PHS were recorded on the fabricated detectors which showed tailing of the ^{137}Cs (662 keV) photopeak due to hole-trapping effects. Depth dependent PHS were digitally generated from 2D biparametric plots to reveal the effects of hole trapping on the gamma PHS at different detector depths and multiple defect energy levels. A digital correction procedure was applied to generate well-resolved PHS with an energy resolution of $\leq$2% for 662 keV γ-rays and to investigate the kinetics of charge trapping. Finally, a novel charge-trapping model has been developed for the first time which explained the entire duration of the pulse-shapes from CZTS based radiation detectors and could be applied to other wide band-gap semiconductors.

TABLE OF CONTENTS

LIST OF TABLES

LIST OF FIGURES

LIST OF ABBREVIATIONS

CdTe..... Cadmium Telluride

CdZnTe .....Cadmium Zinc Telluride

CdZnTeSe .....Cadmium Zinc Telluride Selenide

μτ.....Mobility-Lifetime Product

THM..... Traveling Heater Method

HPB.....High-Pressure Bridgman

LPB ..... Low-Pressure Bridgman

VB ..... Vertical Bridgman

VGF..... Vertical Gradient Freeze

CRSS.....Critical Resolved Shear Stress

PSD .....Pulse-Shape Discrimination

PRC..... Pulse Rise-time Compensation

BP..... Bi-Parametric

HBM .....Horizontal Bridgman Method

GR ..... Guard-Ring

DI .....De-Ionized

GDMS ..... Glow Discharge Mass Spectroscopy

ZR .....Zone Refined

PHS .....Pulse Height Spectra

SEM ..... Scanning Electron Microscope

EDS ..... Energy-dispersive X-ray spectroscopy

IR..... Infra-Red

XPS ..... X-ray Photoelectron Spectroscopy

P/B..... Peak-to-Background

P/V ..... Peak-to-Valley

XRD ..... X-Ray Diffraction

PCB ..... Printed Circuit Board

CCE..... Charge Collection Efficiency

CHAPTER 1

INTRODUCTION

1.1 Introduction to Radiation Detectors

Nuclear radiations play a significant role in building our modern society. Nuclear materials in a reactor produce electricity and supplied at homes with pollution free power. Radiation detectors has improved the technology of nuclear physics and space astronomy. Radiation is being used to detect and image cancer cells. The proliferation of nuclear materials by various entities has enabled the development of nuclear arsenals. Hence, the demand has vastly increased for developing new generation of radiation detectors for high energy x-rays and gamma-rays for various demanding applications [1, 2].

In recent years, semiconductor based nuclear radiation detectors have shown rapid development [3]. Different types of radiation detectors, such as gas detectors and scintillators, are available in the market. Gas-based detectors cannot distinguish alpha, beta, and gamma radiations, can give a rough estimate only. Scintillation detectors, made of sodium iodide (NaI) or bismuth germanate (BGO), are slow in response and exhibit poor energy resolution. Semiconductor based radiation detectors exhibit good energy resolution, high-quality imaging capabilities, and can be fabricated in low power consuming compact systems. Radiation detectors based on several semiconductors, such as silicon (Si), high-purity germanium (HPGe), mercuric iodide (HgI_2), and cadmium telluride (CdTe) have

been developed. However, due to low bandgap, these materials (such as Si, HPGe) require cryogenic cooling which makes the system bulky, show poor resolution, has less stopping power due to low atomic number and these detectors are not suitable for many types of applications [4]. HgI_2 exhibits poor charge transport properties, so it cannot be used as a high-energy gamma-ray detector and it needs encasement as it is a soft hygroscopic material [3]. CdTe is a preferable choice but suffers from low resistivity resulting in high leakage current. For these reasons, a good choice of semiconductor material for radiation detection should have a wide bandgap, high atomic number for high stopping power, and can be made in a compact size. For room-temperature applications, the most commercially pursued detector material for x-ray and gamma-ray detection is cadmium zinc telluride (CdZnTe, or CZT). In recent years, break-through studies have revealed a novel quaternary material cadmium zinc telluride selenide (CdZnTeSe, or CZTS), which can eliminate some limitations of CZT for good detection properties [5, 6]. These findings have opened a wide range of possibilities for fabricating new generation room temperature radiation detectors based on CZTS. This work contributes to developing novel radiation detectors based on CZT and CZTS.

1.2 Dissertation Overview

This work contributes to key areas of ongoing research to make CZT and CZTS based radiation detectors for cost effective and widespread applications. In chapter 1, requirements and background of radiation detectors have been discussed. The advantages of using CZT and CZTS as radiation detection materials are elaborated. Chapter 2 discusses about the different crystal growth processes. The pre-growth and post-growth steps are

extensively explained. In chapter 3, grown CZT crystals are examined by various optical, compositional, and electrical characterizations to ensure its quality. Also, a pixelated CZT detector fabrication and its performance evaluation was discussed. Chapter 3 exhibits similar examinations on laboratory grown CZTS crystals and discussed about the potential of this material to be used for practical applications. Later, a planar CZTS detector was fabricated and evaluated. In chapter 5, the photopeak tailing effect and correction scheme on CZTS detectors were discussed. A novel a charge-trapping model is established for explaining the entire duration of pulse-shape.

1.3 CZT based Radiation Detectors

There are a small number of semiconductor materials for direct read-out nuclear radiation exist, which can provide a compact, portable, lightweight detector. The material should exhibit several qualities to perform as a high-performance radiation detector. As a semiconductor-based radiation detector, it must be able to absorb the nuclear radiation by generating electron-hole pairs, and it must transport the charge pairs through the detector material to the front-end readout electronic circuit. This schematic of the operation is shown in Figure 1.1, where the incoming radiation is absorbed by the radiation detector material. There are three effects which play an important role in radiation measurements. These effects are photoelectric absorption, Compton scattering, and pair production. The photon transfers all its energy to an atomic electron which is photoelectric absorption. Through the Compton process, a photon interacting transfers only a fraction of its energy to an outer electron, producing a hot electron and a degraded photon. A photon with energy above threshold energy of 1.02 MeV interacts within the Coulomb field of the nucleus

producing an electron and positron pair is called the pair production. Among these, the total absorption of the incident energy happens only in the photoelectric effect and thus gives useful information about the photon energy [7]. The atomic number of the material highly affect the interaction cross section. An external bias is applied to separate the electron-hole pairs, and the resultant signal is transferred to detection readout electronics.

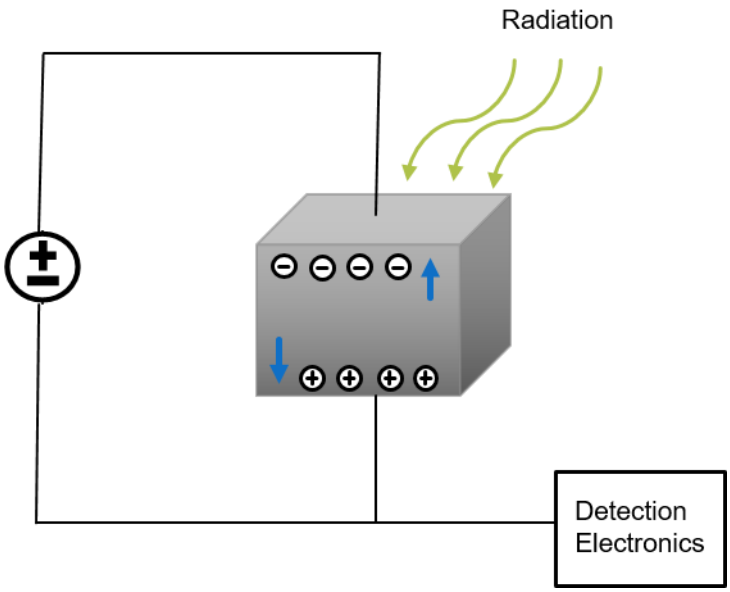

Figure 1.1: Schematic diagram showing the basic principle of a semiconductor-based radiation detector

The ideal characteristics of a material for the use of radiation detectors are summarized in Table 1.1. The semiconductor must have a high atomic number and density, to be capable of stopping high-energy x-rays and gamma-rays, which increases the probability of the radiation interacting with the material. To ensure the transportation of the generated charge from interaction to the readout circuit, the material should have a high mobility lifetime product ($\mu\tau$) and high mobility (μ) for both electrons and holes. The material must have a high resistivity, which reduces the detector leakage current and

therefore the amount of noise present in the entire detection system will be minimum. The material should have wide-bandgap to reduce thermal noise. As CZT is the only semiconductor, which meets all the above properties, it has been the most popular choice for fabricating room temperature radiation detectors in recent years [8-11]. CZT has the necessary stopping power to absorb high energy gamma-rays, with a high atomic number and density. The wide bandgap at ~300K allows operating as a nuclear detector below, at, and slightly above room temperature. Very high resistivity of $\sim 10^{10}$ Ω-cm reduces noise due to leakage current. It has good electron charge transport properties, meaning that electrons can travel through the bulk material without being lost or trapped.

Table 1.1: Requirements of Semiconductor Radiation Detectors and CZT properties.

Qualities	**Requirements**	**$Cd_{0.9}Zn_{0.1}Te$**
Capable of stopping x-rays and gamma-rays	High atomic number	48, 30, 52
	High density	5.78 g/cm^3
High resistivity	$\geq 10^{10}$ Ω-cm	$\geq 10^{10}$ Ω-cm
High electron mobility lifetime product (μτ)	$\geq 10^{-3}$ cm^2/V	$10^{-3} - 10^{-2}$ cm^2/V
High energy resolution	~ 0.5 % or better for High energy gamma rays (i.e. 662 keV)	~1%
High bandgap to reduce thermal noise	1.5 eV or higher	1.6 eV at 300K

CZT crystals are usually grown by using the traveling heater method (THM), high-pressure Bridgman (HPB), low-pressure Bridgman (LPB), vertical Bridgman (VB), and vertical gradient freeze (VGF) methods. However, the yield of detector-grade high-quality

material remains low for CZT crystals grown by various methods due to the presence of various difficulties. The difficulty of growing seed crystals requires superheating. CZT crystal tends to incorporate tellurium inclusions/precipitations and the formation of many types of dislocations. Therefore, the growth of high-yield, low-cost, efficient CZT crystals is still under constant research and development. In the later chapter, we will discuss various growth methods of CZT in detail.

Grown CZT crystals generally exhibit some common issues which can hinder its effectiveness for the use of radiation detector. Various defects in the grown crystals can act as charge trapping centers or generation/recombination centers [12]. Poor hole transport properties of CZT greatly degrades its performance as an efficient radiation detector. The performance of CZT based detectors is however limited by the presence of intrinsic defects like compositional nonuniformity due to Zn segregation, high concentrations of sub-grain boundary networks, and presence of Te inclusions/precipitations [13-15]. The presence of secondary phases like Te inclusions/precipitations can act as charge trapping centers. This attributes to poor charge transport properties such as low drift-mobility and short lifetime resulting in the reduction of the energy resolution of the devices [15-17]. Therefore, it is an utmost requirement to overcome hole trapping to improve detector performance. This problem is addressed by three different approaches: by configuring the radiation detection, by applying pulse shape correction, and by designing unipolar charge sensing devices.

As shown in Figure 1.2, in the presence of hole trapping, a long tail is produced in the measured spectrum due to incomplete charge collection. If the counts of events that are excited near the cathode are increased by irradiation from the cathode side, the probability

of hole trapping can be minimized. This is especially useful for thin detectors. Besides, an uniform trigger rate effect can be obtained by using a cathode electronic signal to trigger the acquisition of electrode pulse heights. Therefore, a more uniform pulse height acquisition response can be achieved than anode side irradiation [18, 19].

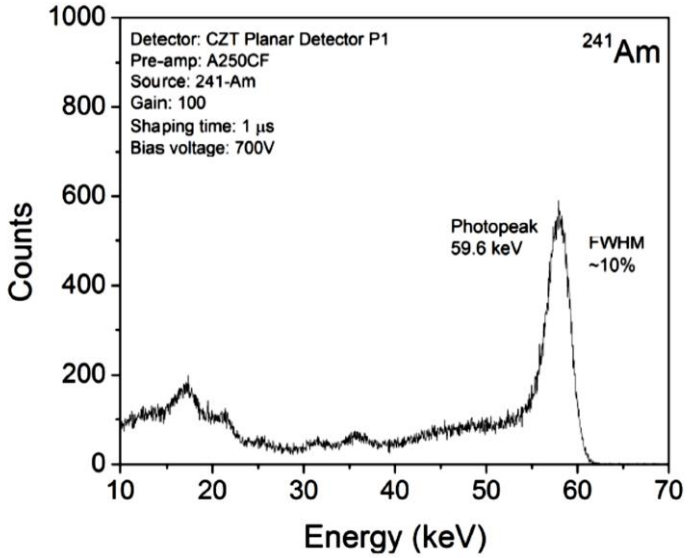

Figure 1.2: ^{241}Am pulse height spectrum obtained from a CZT based planar detector.

Various electronic methods such as pulse-shape discrimination (PSD), pulse rise-time compensation (PRC), etc. have been applied to improve the spectrometric performance of CZT. PSD method can differentiate events with a large contribution from hole trapping. A fraction of the pulses with long rise-times is eliminated [20-23]. On the other hand, the PRC method can reduce the loss of efficiency while obtaining energy resolution improvement. The amplitudes associated with severe hole trapping events are compensated [22, 24, 25]. For rejecting the incomplete charge collection events in CZT, bi-parametric (BP) analysis had been applied which correlates the ratio of the cathode to

anode signal and drift times measured for each detected event. Hence, without affecting the photopeak efficiency significantly, the low-energy tail and the Compton continuum of the energy spectrum can be greatly reduced [26, 27].

Both techniques (configuring the irradiation detection and applying pulse shape correction) still suffer insufficient energy resolution. Single charge carrier sensing techniques are widely employed by developing careful electrode designs such as Frisch-grid, pixelated configuration, coplanar grids, strips, multiple electrodes, and drift-ring detectors (Figures 1.3 – 1.6). Frisch-grid based design was introduced by Frisch [28]. A general configuration of a Frisch-grid is shown in Figure 1.3a [29]. A Frisch grid is placed close to the anode. The region between the cathode and Frisch grid is called the interaction region where most gamma-rays interact. The weighting potential at the interaction region is invariable so that charge transportation has no contribution to the induced charge on the anode which is shown in Figure 1.3b [30, 31]. Therefore, the detector primarily functions as electron charge carriers pass through the measurement region [16, 32, 33]. However, poor detector response in the pulse-height spectra often occurs due to the slow-rising events. Pixelated detectors (shown in Figure 1.4) are widely used for position-sensitive applications because it can provide excellent energy resolution [31, 34-38]. The charge extraction becomes more localized near the anode and it is inversely proportional to the ratio of width to thickness of the pixel cell. Therefore, the weighting potential distribution is like Frisch-grid based design. However, pixelated devices suffer from charge sharing problems among pixels which is difficult to solve. The coplanar grid was first reported by Luke [39, 40]. The schematic is shown in Figure 1.5a [37]. These strip electrodes are

connected alternately to form two banks of grid electrodes. The weighting potential distribution is shown in Figure 1.5b. the carriers drifting near the anode will contribute a lot to the induced charge on the electrode as the weighting potential abruptly changes near the area of the anode. Therefore, the charge collecting effect is much like that of a Frisch grid detector. Shaping the electric field can lead to reduction of noise. Also, by channeling charge in to a small readout anode with a capacitance can increase the signal-to-noise (SNR) ratio. In a drift-ring device (Figure 1.6), several concentric ring electrodes are fabricated. A potential gradient is applied along these rings which induces a transverse electric field. This field pushes the electrons towards the central anode. Therefore, by shaping the electric field and channeling charge to a small central readout anode high-quality spectroscopic performance can be achieved [41, 42]. With further study and continued research, it is anticipated that CZT will become more cost effective to produce and will exhibit better energy resolution for high energy x-ray and gamma-ray radiation.

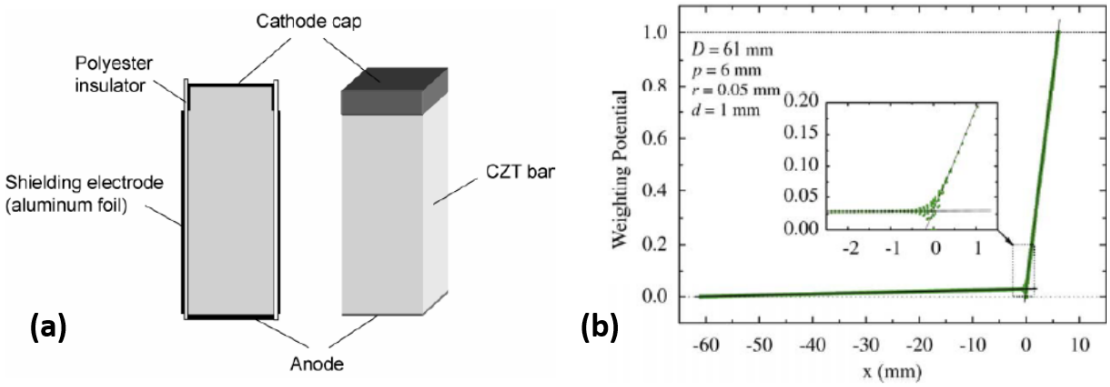

Figure 1.3: (a) Schematic of a Frisch-grid detector, and (b) 2-D map of weighting potential around the Frisch grid [29, 31]

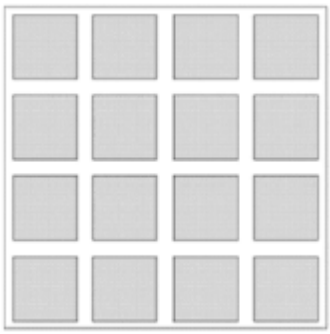

Figure 1.4: Geometry design of pixelated CZT detector configuration [37].

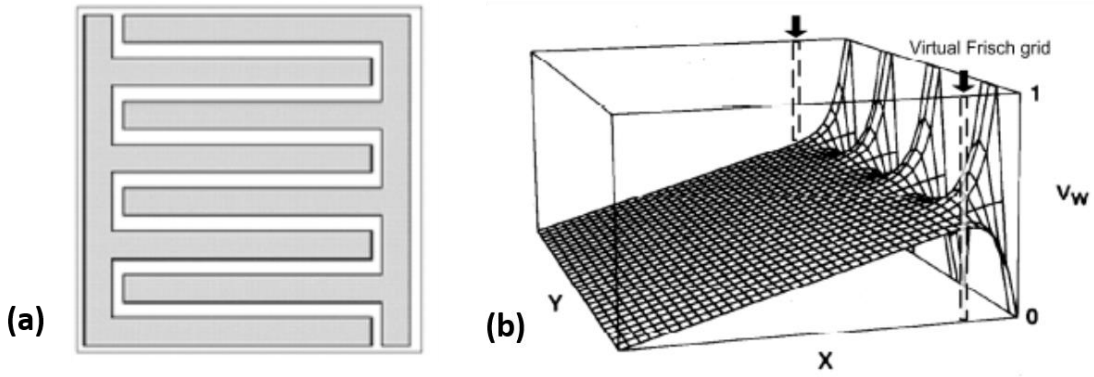

Figure 1.5: (a) Schematic of a coplanar grid detector, and (b) 2-D map of weighting potential around the coplanar grid. [37, 39, 40]

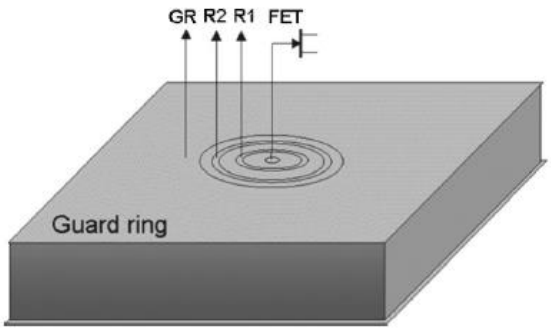

Figure 1.6: Schematic of a drift-ring detector showing two rings R1, R2 and guard-ring (GR) [42]

1.4 CZTS based Radiation Detectors

Recent break-through studies have shown that the inclusion of Se to the CZT matrix can lead to a reduction of the density of Te inclusions/precipitates and formation of subgrain boundaries [5, 6]. The novel quaternary CdZnTeSe (CZTS) material is found to be effective for better compositional uniformity and minimizing the formation of sub-grain boundaries and its networks. Also, CZTS has the potential to prevent the formation of Cd vacancies as Se has the highest partial pressure among group VI elements [43]. Techniques like traveling heater method (THM) [5, 6], horizontal Bridgman method (HBM) [44], have been adopted for the growth of CZTS. In this work, we will further discuss the growth techniques, characterization, and fabrication of CZTS crystals in subsequent chapters.

CHAPTER 2

CRYSTAL GROWTH

2.1 Introduction

New growth techniques are investigated for the development of CZT and CZTS as room-temperature semiconductor radiation detector materials. Defects and single crystallinity make CZT very expensive to produce and use [13]. The effects of impurities and oxidation become more prominent as growth temperature increases [45]. One of the most important problems limiting the widespread applications of CdZnTe based devices is the associated cost inherited from low single crystal yield from the crystal growth processes. Defects in grown crystals can act as charge trapping centers or generation/recombination centers. In this chapter, we will discuss about preparations of precursor materials and crystal growth ampoule. We will discuss about various crystal growth processes and our modified growth process for growing CZT and CZTS crystal boules.

2.2 Precursor Material Preparation

Material impurities create a strong negative impact on CZT or CZTS detector's performance [13, 46, 47]. Hence, very high purity precursor materials are needed to use for growing CZT crystals. However, the highest purity that is readily commercially available for elemental precursors (cadmium, zinc, tellurium, and selenium) is 5N (or 99.999% pure).

Therefore, further purifications of these precursors were carried out using an in-house multi-pass horizontal zone refining system. Figure 2.1 shows a horizontal, two-heater zone refining system. The zone-refining system consists of a two-zone heater with each heater connected to a computerized process controller, a data acquisition system that can precisely control the temperatures and the horizontal movement of the materials inside the heater rings.

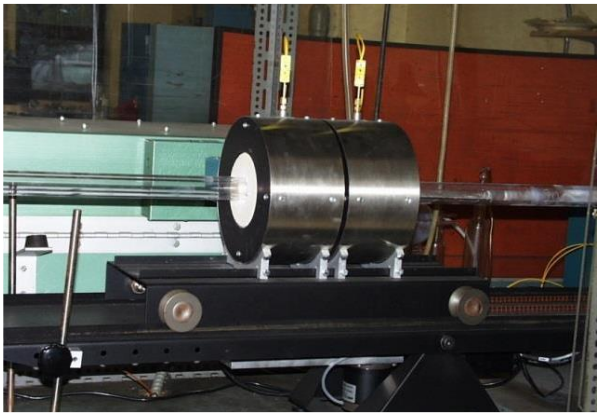

Figure 2.1: In-house horizontal zone-refining system used to purify precursors [38].

Zone refining is a technique developed to purify semiconductor materials in 1950s by Bell Labs scientists. Inside a material, the impurities are distributed differently in their solid and liquid phases at equilibrium. When a long tube filled with solid materials is passed through a ring heater, a small zone of material is melted with the remainder of the material remaining solid. The impurities will be collected in this molten zone as it moves through the solid. All the impurities will eventually gather to one end of the material, and the remainder of the material will be highly pure. Figure 2.2 shows a schematic of a two-

zone horizontal zone-refining system and the corresponding states of a material (e.g., Se in this case) [48].

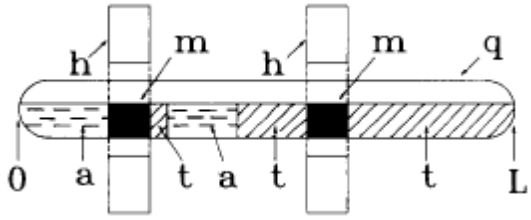

Figure 2.2: Different phases of selenium during horizontal zone refining where, a= amorphous Se, t-trigonal Se, m-molten Se, h-heater, q- quartz tube, 0-starting point, L-finishing point [48].

For zone refining, the quartz tubes used were manufactured by Omni Glass, Inc. The quartz tube (length = 60 cm, OD = 28 mm, and ID = 25 mm) was first closed at one end to make an open ampoule. The empty ampoule was cleaned using successive washes with acetone, methanol, isopropanol, 10% HF aqueous solution and de-ionized (DI) water (18 MΩ). Then, the ampoule was baked for 12 hours at ~ 1000 °C under constant nitrogen flow (~0.25 liter/min). The cleaned and dry quartz ampoule was filled up to the first 18″ of the length with individual precursor feed material (~500 grams Cd, Zn, Te, and/or Se of 5N purity). After that, the open side of the ampoule was sealed and then suspended over the tracking actuator in the horizontal zone refining furnace. The furnace temperature was slowly ramped up (at a rate of 10 °C per minute) to a temperature which is slightly above the melting point of the precursor material. The melting points of precursor materials Cd, Zn, Te, and Se are 321.1 °C, 419.6 °C, 449.5 °C, and 220 °C respectively. The furnace was

moved horizontally along the ampoule length at a rate of 30 mm per day by using a tracking actuator. The furnace made 40-45 passes from one end of the ampoule to the other.

Inside the solid precursor material, the ring furnace melted a small zone. The heat source was slowly translated horizontally, and due to that the melted precursor material re-solidifies after the heat source moves from that position. Due to the solid-liquid phase transition, impurities got segregated from the solid phase to the molten zone. As the furnace slowly shifted horizontally along the ampoule, the molten zone got shifted from one side to another resulting the expelled impurities to be accumulated at the end of the ampoule. After multiple passes (~45 passes), most of the material became highly pure (~7N purity) while most of the impurities were collected into a small portion of the solid at one end.

After completion of the ZR process, the ampoule was cut, and the zone-refined material was removed inside an argon-controlled glove box. Depending on the uniformity of transparency, a length of the ingot was considered 'pure' material and cropped from the impure end of the ingot. The removed 'pure' precursor material was then stored in argon-filled polyethylene bottles until they were ready to be used in the CZT or CZTS crystal growth. Glow discharge mass spectroscopy (GDMS) analysis was performed on the zone refined (ZR) precursor materials (Cd, Zn, Te, and Se) and compared with the pre-ZR data to evaluate the effectiveness of the ZR purification. Table 2.1 shows the results of the GDMS analysis performed on the zone-refined Cd, Zn, Te, and Se materials. Samples were tested for various elements. The relative error associated with the GDMS technique is reported to be ~ 20%. The GDMS data showed that the zone refining process has segregated out a diverse amout of impurity materials. The concentrations of the common

elemental impurities in the zone refined precursor Cd, Zn, Te, and Se material were 3-12 times less compared to samples before zone purification. For example, after zone purification, the concentration of Ni impurity in Cd decreased from 3.5 ppb to 0.3 ppb.

Table 2.1: GDMS impurity analysis for zone refined materials.

Impurity	**Cd**	**Zn**	**Te**	**Se**
O	2.8 (< 0.5)	2.4 (< 0.4)	4.6 (< 0.6)	n/m
Na	1.5 (0.5)	1.7 (0.2)	1.6 (<0.4)	9.5 (<1.2)
Sn	1.5 (< 0.5)	1.6 (< 0.2)	1.2 (< 0.2)	12 (<0.5)
Al	2.3 (0.3)	1.4 (n/d)	1.6 (n/d)	2.2 (1.0)
Cd	Major	1.3 (0.3)	1.5 (0.3)	n/m
Li	4.1 (1.4)	4.5 (1.2)	2.2 (<0.3)	0.5 (<0.5)
Mn	5.5 (1.5)	1.2 (<0.3)	1.4 (<0.3)	1.0
Zn	1.2 (0.6)	Major	n/m	10 (1.0)
Te	4.4 (0.6)	0.6 (<0.1)	Major	8.0 (0.35)
Cu	4.2 (1.2)	2.4 (0.2)	1.6 (<0.3)	25 (0.2)
Pd	1.6 (<0.3)	1.5 (<0.2)	1.9 (<0.2)	n/m
Co	2.1 (<0.2)	1.9 (<0.4)	1.4 (<0.2)	1.0 (<0.2)
Ni	3.5 (0.3)	1.6 (n/d)	1.4 (n/d)	5.0 (0.2)
Fe	0.8 (0.2)	0.5 (n/d)	0.6 (n/d)	10 (n/d)
Hg	4.4 (0.3)	4.1 (<0.5)	4.5 (<0.3)	7.0 (<0.4)
Si	5.4 (1.6)	2.5 (0.6)	2.3 (1.2)	5.0 (<0.4)

Note: Impurity concentration in parts per billion (ppb). Parenthesis data are after ZR showing the effectiveness of ZR process.

2.3 Crystal Growth Ampoule Preparation

The crystal-crucible interaction can lead to formation of twins and grain boundaries. The quartz crucibles can ease the problem of sticking of the crystal to the

crucible walls. Due to this reason, many authors have suggested the use of graphite crucibles [49], carbon-coated quartz crucibles [50], or pBN crucibles [51]. Cd susceptible to adhere to the inside wall of the quartz ampoule. Cd can react with the SiO_2 (quartz) material due to with high thermal conductivity (0.9 $W/cm^{-1}K^{-1}$), low melting point (321 °C) and volume expansion on melting. The adherence of CZT with the inner wall of the quartz ampoule one of the major issues with this crystal growth. To protect the CZT ingot from interaction with the quartz surface, the interior of the quartz ampoule was coated with thin layers of carbon [45]. This process also helps to prevent wearing of the ampoule surface. Carbon coating also prevents the outgassing of impurities from the inner wall of the ampoule and the reaction of materials with quartz inside the ampoule. It does not influence the electrical properties of the grown crystals as carbon is a neutral impurity element. Any water vapor or residual oxygen present inside the quartz ampoule walls also gets trapped in the carbon layer.

Figure 2.3 shows the schematic of the carbon coating system. Before carbon coating, quartz ampoule was successively rinsed with acetone, methanol, isopropanol, and de-ionized (DI) water. Next, the ampoule was etched using 10% hydrofluoric acid and rinsed with DI water several times. The ampoule was then inserted into a stainless-steel encasement inside the furnace as shown in Figure 2.4 and purged with argon gas for 15 minutes. The quartz ampoule wall is then coated with carbon by n-Hexane (HPLC grade, 95+%) vapors at about 800 ºC within a furnace under constant argon flow. Figure 2.4 shows the installed carbon coating system at our laboratory.

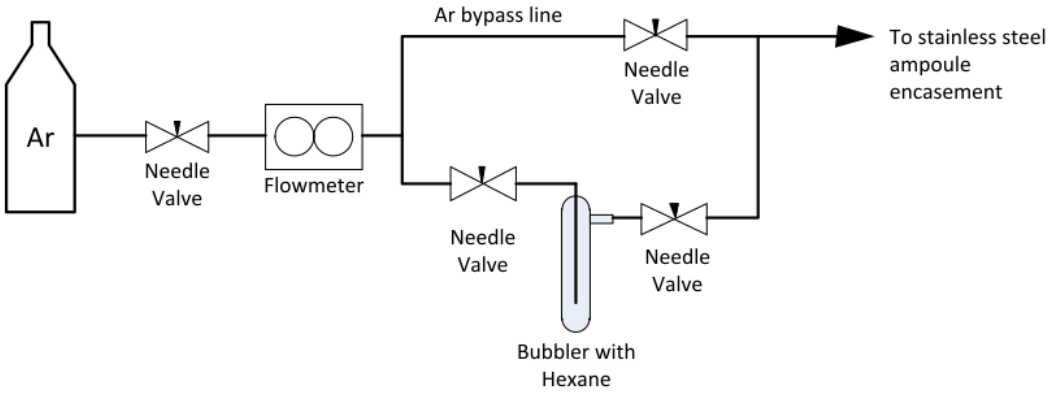

Figure 2.3: Schematic diagram of the basic principle of a carbon coating system [38].

Figure 2.4: A picture of the carbon coating system at our laboratory [38].

For carbon coating, the furnace temperature was ramped up to 1100 ºC at a rate of 10 ºC per minute, under constant argon flow. Then the ampoule was baked for 3 hours. After that, the temperature was ramped down to 800 ºC. After purging with argon for 15 minutes at 800 ºC, argon flow through the normal hexane (n-hexane) bubbler is enabled. The hexane flow rate was constantly maintained at 7 mL/minute for 2.5 hours. The inner wall of a 1″ diameter ampoule was coated with ~1 μm thick carbon layer. After coating, the ampoule is purged off the hexane gas by flowing argon for 30 minutes. The carbon-coated ampoule is then annealed at 1100 ºC for 1 hour. The location of the ampoule inside

the furnace and the argon flow rate were adjusted to find the optimum conditions. Figure 2.5 shows a picture of a carbon-coated ampoule.

Figure 2.5: Quartz ampoule with carbon coating (top) and without coating (bottom).

2.4 Overview on Crystal Growth Methods

For the development of CZT as a room-temperature semiconductor gamma-ray detector material, new growth techniques are constantly being investigated. CdTe is alloyed with zinc to grow cadmium zinc telluride. This creates a ternary compound consisting of CdTe with Zn atoms occasionally replacing Cd atoms in the lattice structures. The ratio of Cd: Zn is commonly 90%:10% for detector grade CZT crystals [9]. The resulting material is referred to as $Cd_{0.9}Zn_{0.1}Te$. From the phase diagram shown in Figure 2.6, the melting point of $Cd_{0.9}Zn_{0.1}Te$ is ~1120°C. The most common techniques used for growing large II-VI compounds (like CdTe, CZT, CZTS) are the melt-growth ones, encompassing the high-pressure Bridgman (HPB) and low-pressure Bridgman (LPB) method , the vertical Bridgman (VB), and the horizontal Bridgman method (HBM) [44, 52-56]. Other approaches include the vertical gradient freeze (VGF) [57, 58], traveling

heater method (THM) [59] and boron oxide encapsulated vertical Bridgman technique [60, 61].

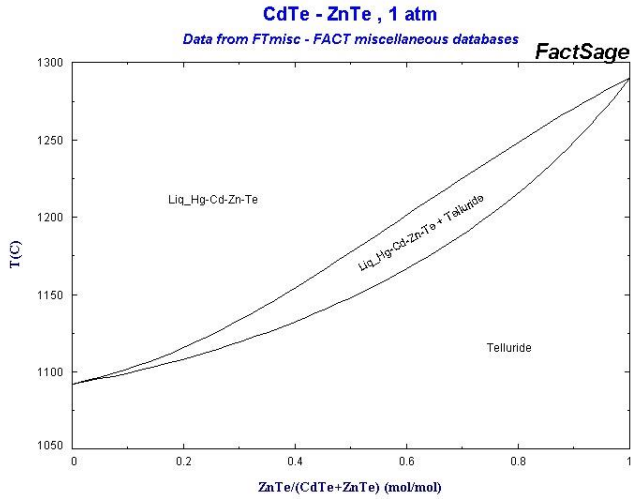

Figure 2.6: Phase Diagram for CdZnTe. Topline indicates liquidus temperatures, the bottom line indicates solidus temperatures [62].

The HPB and LPB methods suffer from various defects which prevent widespread application of CZT as a room temperature semiconductor detector. CZT crystals grown by HPB are inhomogeneous, due to macro-defects such as small grain sizes and greater subgrain boundaries. Furthermore, Zn segregation results significant variations in the concentration of zinc present from one end of the ingot to another [4, 13]. Therefore, HPB results in only 25% of an ingot yielding sizeable single crystals and only 10% of the ingot yielding detector-grade CZT. The LPB method requires a simpler furnace setup than the HPB method. It uses ampoules which are held under vacuum and sealed. However, yields are like the HPB method. Both methods suffer from large amounts of defects due to impurities introduced because of the high growth temperature [4, 13].

The THM allows the growth of CdTe and CZT at much lower temperatures than other in melt growth methods. Also, the solubility of excess tellurium within the solid CdTe crystal is decreased at low enough growth temperatures enabled by sufficiently high tellurium levels in the liquid zone [63]. Hence THM can limit the formation of tellurium precipitates in the crystal as it cools. However, THM is the slowest growth process among others which is on the order of millimeters per day. It also suffers from growth interface instabilities [64-67]. Besides, the number of second-phase tellurium particles are less in THM grown ingots compared to other growth processes [67]. However, many THM ingots still contain levels of these particles that are unacceptable for detector applications.

In this dissertation work, we have adopted a modified vertical Bridgman solvent growth method for growing detector grade CZT and CZTS crystals. This growth method is based on the conventional vertical Bridgman method incorporating a modified solvent growth method. During the past two decades, the Bridgman method has been used successfully to grow detector grade CZT crystals. This technique was at first demonstrated by Harvard physicist Percy Williams Bridgman. For III-V and II-VI compounds (smaller thermal conductivity), it has been used to grow single crystals. The process is explained in Figure 2.7. The Bridgman technique uses a “hot” and “cold” zone to create a temperature difference within a furnace. The hot zone of a VB apparatus consists of several separate resistance heaters with a temperature above the melting point of the substance to be crystallized. The polycrystalline ingots are placed inside the crucible/ampoule depending on the materials. The ampoule containing the molten precursor materials is moved inside the furnace along the axis of a temperature gradient. CZT is grown at a hot zone

temperature of about 1120°C using stoichiometric $Cd_{0.9}Zn_{0.1}Te$ in atomic proportions [13]. The commonly used materials for use as crucibles are quartz and graphite, due to their resistance to high temperatures and pressures. Typical growth rates are in the range of 1mm/hour, with a temperature gradient of about 1.5°C/cm.

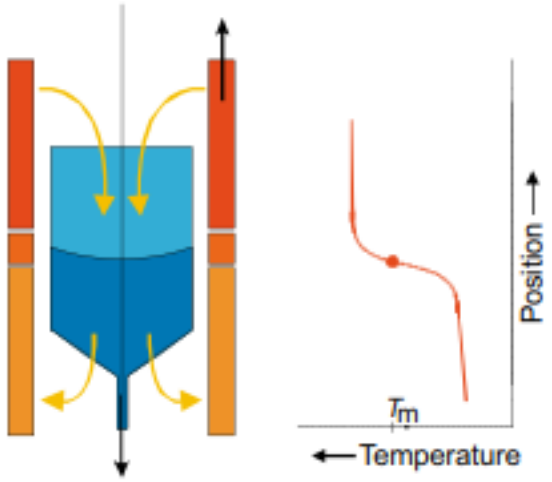

Figure 2.7: A schematic of the hot and cold zone of vertical Bridgman growth [68].

However, the Bridgman method is a high-temperature growth method at stoichiometric conditions. At a high temperature (excess of 1100 ºC), the Cd partial pressure is very high which creates the possibility of an explosion at high temperature. Besides, pre-synthesized precursors are not required for this growth method which makes the system cost-effective. In the case of a solvent growth where 50% excess Te is used, this melting temperature is kept ~980°C. Figure 2.8 shows the solution growth method steps [69].

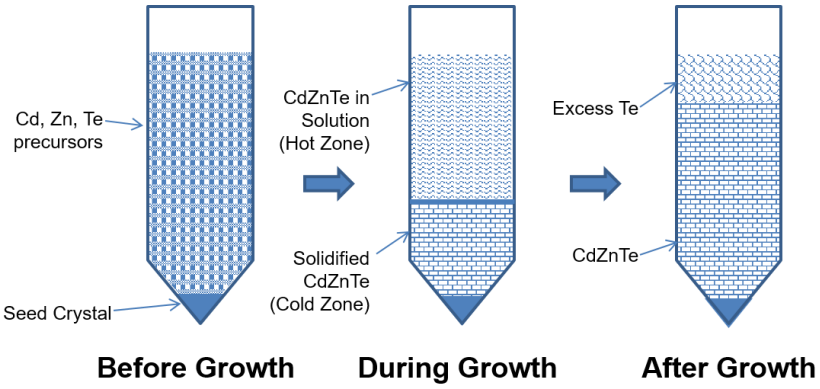

Figure 2.8: Solution growth method steps for CZT growth [69].

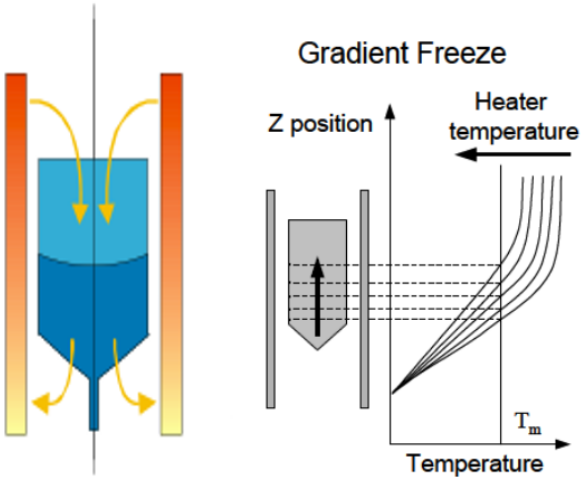

Figure 2.9: Schematic of the hot zone and cold zone of VGF growth [68].

In a classical Bridgman growth, it is difficult to achieve adequate long-term stability of the growth interface due to relative motion. The growth interface can be affected by temperature fluctuations and thermal drift. This can induce spurious nucleation. That is why the vertical gradient freeze (VGF) technique can also be applied to grow CZTS crystal. For VGF, the heat-transport control can be stabilized, where the growth ampoule and the heaters are stationary [68]. Figure 2.9 explains the vertical gradient freeze schematic. The

growth is accomplished by programmatically ramping down the temperatures of the hot and cold zones. Then keeping a constant temperature gradient, the melting point isotherm of the system is swept from the seeding position to the end of the growth ampoule. The same temperature gradient over the growth interface can be achieved by programming the furnace zones. The VGF growth rate is the fastest among others which makes it one of the most cost-effective ways of growing II-VI compound semiconductors.

2.5 Experimental Details of Crystal Growth

Figure 2.10 shows the modified vertical Bridgman crystal growth system at UofSC. It consists of a Lindberg Blue three-zone furnace. Each zone can be independently controlled. The vertical movement of the quartz ampoule is run by an actuator placed vertically along the growth axis. To prevent or to reduce radial/azimuthal inhomogeneity of the temperature, the quartz ampoule is rotated continuously during growth. This rotation is performed by a gear motor. The heaters, gear motor, and actuator are interfaced with a laboratory-developed software through an Arduino UNO which is a microcontroller board based on the ATmega328. The Arduino UNO has 20 digital input/output pins (of which 6 can be used as PWM outputs and 6 can be used as analog inputs) and a 16 MHz resonator. It also has an in-circuit system programming (ICSP) header, a USB connection, a power jack, and a reset button. A user interface software based on LabVIEW is developed for controlling the Arduino signals from a dedicated laboratory computer.

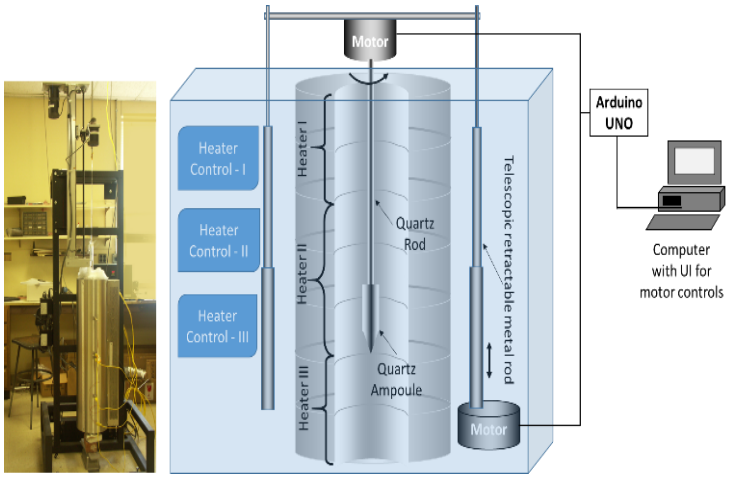

Figure 2.10: Modified vertical Bridgman growth system developed at our laboratory.

Figure 2.11: Quartz ampoule sealing system at our laboratory for growing crystals.

Zone refined (~7N purity) Cd, Zn, and Te precursor materials were weighed in stoichiometric amounts with 50% excess Te for $Cd_{0.9}Zn_{0.1}Te$ crystal growth. Then the precursors were sealed in carbon-coated quartz ampoules with 4 mm wall thickness under a vacuum of $<10^{-6}$ Torr. Figure 2.11 shows the sealing system of the quartz ampoule. It

consists of turbopump backed by a dry vacuum pump. After loading the ampoule inside the inlet line of the turbopump a high vacuum of $<10^{-6}$ Torr is achieved. Then the materials were heated at ~110 ºC for 12 hours for removing any moisture from the environment. The ampoule loaded with materials consists of a solid quartz rod plug (with a diameter equal to almost the inner diameter of the ampoule) at the open end. Then at the position of the plug, the wall of the ampoule is melted at ~2000 ºC using an oxyhydrogen flame. Hence, the ampoule gets sealed with the plug being melted and solidified with the ampoule.

After sealing, the ampoule was inserted into a horizontal 3 zone furnace which is simulated and modeled for large-volume CZT synthesis and growth. The temperature profile for the vertical Bridgman method is shown in Figure 2.12. The ampoule was slowly heated to a maximum temperature of ~1085º C to achieve the Te-rich CZT polycrystalline charge. The ampoule was constantly rotated at a speed of ~15 rpm to get the compositional homogeneity. The synthesized polycrystalline ingot was then placed in a conically tipped thick-walled (4-5 mm) quartz ampoule which holds a CZT seed crystal and sealed under a vacuum of $\sim 10^{-6}$ Torr. The ampoule was inserted into a three-zone vertical Bridgman furnace and was continuously rotated at a low speed of ~15 rpm. The axial temperature gradient of ~3 ºC/cm and heat flow pattern was programmed, controlled, and achieved inside the furnace for minimizing stress at the solid-liquid interface resulting from thermal expansion coefficients and reducing the evaporation of Cd. The grown crystal directionally solidified by moving the ampoule downward at a constant velocity of ~2 mm/hr. This cycle was repeated for at least three times to obtain a larger size single crystal. The growth process is followed by a controlled cooling to room temperature maintaining thermal stress

below the critical shear stress [38]. We have successfully grown a large diameter up to 3.0 inch and 4.8 inches in length detector grade CZT boules (~2.8 kg with ~75% singularity). Figure 2.13 shows ~1″ diameter CZT wafers with ~90% singularity of the grown ingot.

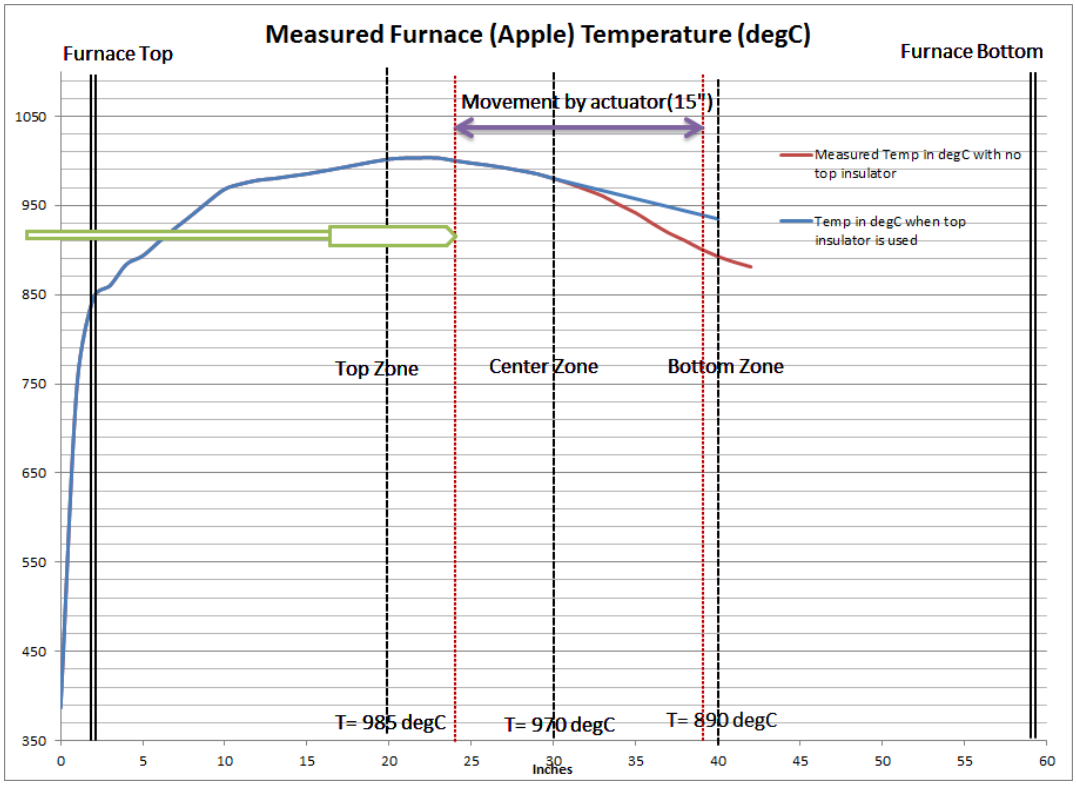

Figure 2.12: The temperature profile for the modified vertical Bridgman method used at our laboratory.

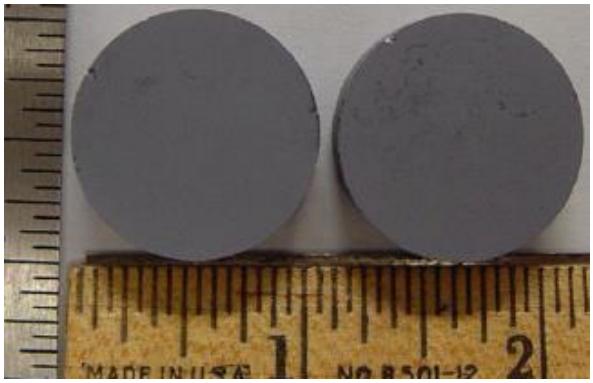

Figure 2.13: ~1″ dia CZT wafers showing ~90% singularity of the grown ingot.

CZTS with three different compositions were grown using vertical Bridgman method. The three compositions of CZTS are $Cd_{0.9}Zn_{0.1}Te_{0.97}Se_{0.03}$, $Cd_{0.9}Zn_{0.1}Te_{0.95}Se_{0.05}$, and $Cd_{0.9}Zn_{0.1}Te_{0.925}Se_{0.075}$. 10% excess Te was used as a solvent for each growth. Cd has low melting point (321 ºC) and high thermal conductivity (0.9 $W/cm^{-1}K^{-1}$), tends to adhere to the inside wall of quartz (SiO_2) ampoule (to be used for growing crystal). Besides, it can react with the SiO_2 material. Because of these reasons, the inner wall of the quartz ampoule needs to be coated with carbon, which can also trap any residual oxygen or water within the ampoule [45]. A conically tipped quartz ampoule (ID: 16 mm and OD: 20mm) with a wall thickness of 4 mm was selected for CZTS growth. At first, the bare quartz ampoule was annealed in a furnace at 1100 ºC for 8 hours. The temperature was ramped down to 800 ºC. The carbon coating was done by flowing n-Hexane vapors with a rate of 7 mL/min for 2 hours under argon flow at 800 ºC. After that, the carbon-coated ampoule was annealed at 1100 ºC for 1 hour.

Stoichiometric amounts of zone refined 7N purity precursor materials (Cd, Zn, Te, and Se) were loaded into the carbon-coated quartz ampoule with 10% excess Te. The loaded materials were heat-treated at 110 ºC for 12 hours to remove any moisture traces. After that, the ampoule was sealed under a vacuum of $<10^{-6}$ Torr. Then, it was loaded inside a three-zone vertical furnace which is simulated and modeled and developed for large-volume CZTS synthesis and growth. To reduce the off stoichiometry of CZTS polycrystalline charges, the materials were slowly heated and synthesized at three different temperatures. Heat treatments were performed at 750 ºC, 850 ºC, and 950 ºC for 3 hours each to synthesize the charges directly from the elements with the addition of excess Te

[70]. During synthesis, the ampoule was constantly rotated at a speed of ~15 rpm to get the radial compositional homogeneity.

The furnace was then programmed and controlled to achieve the desired temperature profile for vertical Bridgman growth. Figure 2.14 shows a simulated steady-state temperature distribution (using COMSOL) inside the three-zone vertical Bridgman growth furnace. The growth profile is designed for minimizing stress at the solid-liquid interface resulting from thermal expansion coefficients and reducing the evaporation of Cd. The furnace is ramped up to the peak growth temperature of 1000 ºC in stages, with progressively slower ramp rates. An axial temperature gradient of 2.5 ºC/cm was achieved. The ampoule was moved downward at a constant velocity of 2 mm/hour resulting in the directional solidification of the grown crystal. During this, the ampoule was constantly rotated at a speed of ~3 rpm. This cycle was repeated three times and then the furnace was slowly cooled down. Figure 2.15 shows the as-grown CZTS ingots. The cut pieces from the $Cd_{0.9}Zn_{0.1}Te_{0.95}Se_{0.05}$ (CZTS) ingot are shown in Figure 2.16.

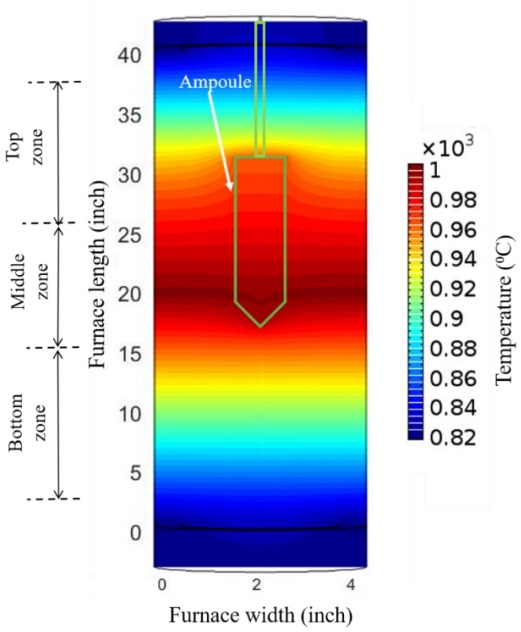

Figure 2.14: Cross-sectional view of the furnace showing simulated steady-state temperature distribution for growing CZTS.

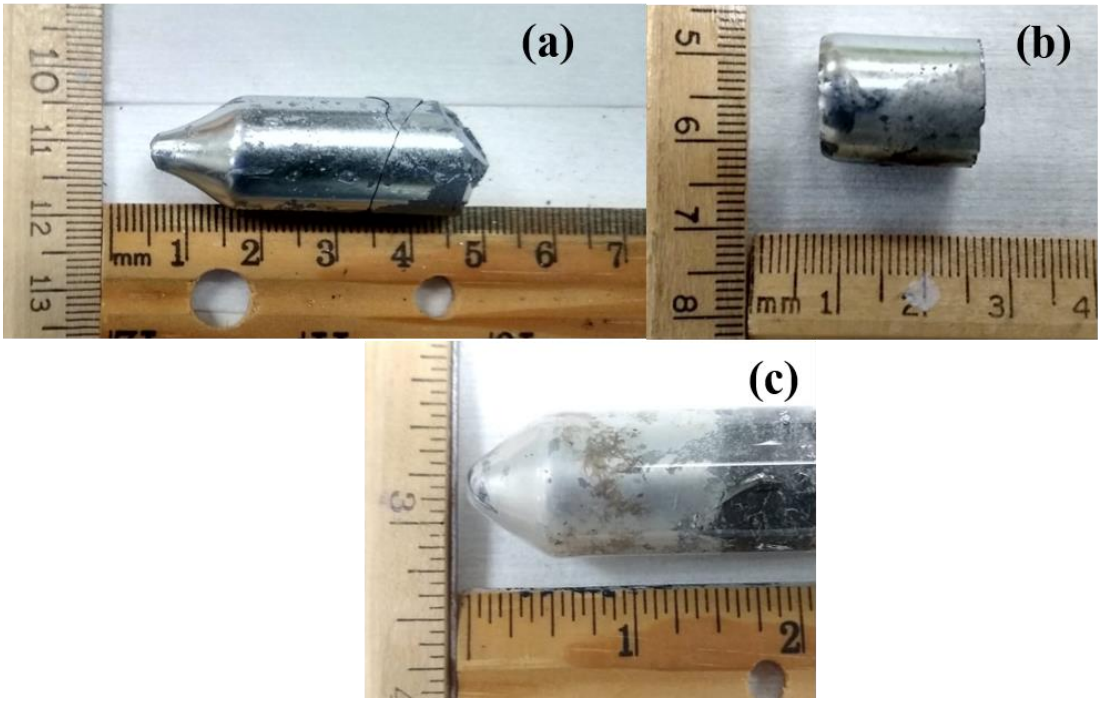

Figure 2.15: Picture of the as-grown ingots of (a) $Cd_{0.9}Zn_{0.1}Te_{0.97}Se_{0.03}$, (b) $Cd_{0.9}Zn_{0.1}Te_{0.95}Se_{0.05}$, and (c) $Cd_{0.9}Zn_{0.1}Te_{0.925}Se_{0.075}$.

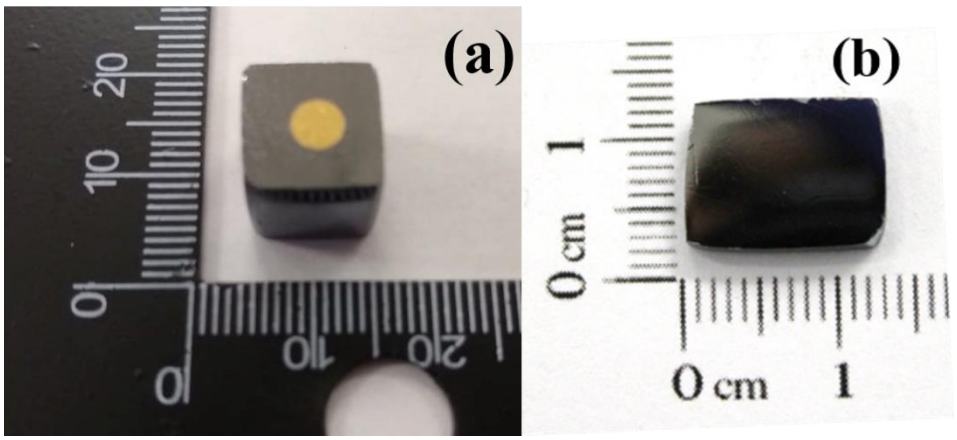

Figure 2.16: (a) Square-shaped and (b) rectangular-shaped sectioned pieces of the $Cd_{0.9}Zn_{0.1}Te_{0.95}Se_{0.05}$ ingot.

CHAPTER 3

CZT DETECTOR FABRICATION AND PERFORMANCE ANALYSIS

3.1 Introduction

In this study, large volume (~19.0 × 19.0 × 5.0 mm^3) 10 × 10 pixelated detectors are fabricated from cadmium zinc telluride, CdZnTe (CZT), crystals grown in our laboratory and investigated for its performance as a gamma-ray detector. Pulse height spectra (PHS) were obtained for each pixel using a ^{137}Cs (662 keV) gamma radiation source. Digitized charge pulses were recorded from the pixels using high bandwidth and high-resolution digitizer card. Biparametric (BP) plots and depth-dependent spectra were derived from the digitized pulses. Although the BP plots showed anomalous behavior of the 662 keV events when compared to that in planar detectors, they helped to extract pulse-height spectra free from the effect of extensive hole trapping.

3.2 CZT Crystal Processing

Unwanted surface features on the crystal can lead to higher leakage current and surface charge trapping centers. Hence, it is essential to polish the crystal surface to remove the defects, scratches, and other unwanted features. After the completion of CZT crystal growth, the CZT ingot was taken out and cut into square/rectangular shapes using a wafer cutter “Extec Labcut 150” at our lab with different dimensions. The cut crystals were grounded and lapped using a series of SiC sandpapers (up to 1500 grit sandpaper).

Sandpapers are used to get rid of varied landscapes, that are present after the wafer saw cutting procedure. Then the surface was polished with 0.3 µm and 0.05 µm alumina powder using microfiber pads. This gradual sanding and polishing help to work with decreasing ridges and certain other formations even smaller in depth till they disappear altogether. Then the surface was cleaned using an ultrasonicator for 1 minute. The crystal is then chemo-mechanically etched using a 5% Bromine-Methanol solution (Br_2-CH_3OH) for 1 minute and finally rinsed off with de-ionized water. The chemo-mechanical polishing reacts with Cd and helps to remove the cadmium oxide (CdO) on the surface by forming cadmium bromide ($CdBr_2$) and the surface layer are also enriched by Te [71-73].

3.3 Optical Characterizations

The bare polished crystals were characterized using a scanning electron microscope (SEM) for examining surface morphology. We used Tescan Vega3 SEM at the Nanocenter of UofSc. This is model of scanning electron microscope (SEM) is suitable for both material and biological inspections. The microscope is equipped with a backscattered electron detector and the capability for (Energy-dispersive x-ray spectroscopy) EDS. Figure 3.1 shows an SEM image of the surface of a CZT sample after polishing. SEM image confirms a very smooth surface morphology with minimal structural defects. A smooth surface finish ensures the deposition of quality metal contacts with a uniform thickness which in turn provides reliability and repeatability of the measurements.

One of the major issues which can affect CZT crystal quality grown using either stoichiometric or with excess Te is the presence of Te inclusions and precipitates uniformly distributed in the bulk crystal. The Te-rich regions can act as defects that degrade the

electrical properties of the CZT material. The Te inclusions/precipitations of the bare polished crystal were investigated through infra-red (IR) transmission imaging by using a 75 W high stability Xenon arc lamp. As the bandgap of Te is ~0.3 eV at 300K, which is much lower bandgap than that of CZT, the infrared light will pass through the sample except at the locations of Te-rich sites within the crystal. Figure 3.2 shows the IR transmission image of the bare crystal surface. The average Te inclusions/precipitations size was found to be less than ~9 µm in the crystal which confirms the growth of good detector grade crystals. Bigger sized Te inclusions act as charge trapping centers leading to permanent charge loss [74, 75].

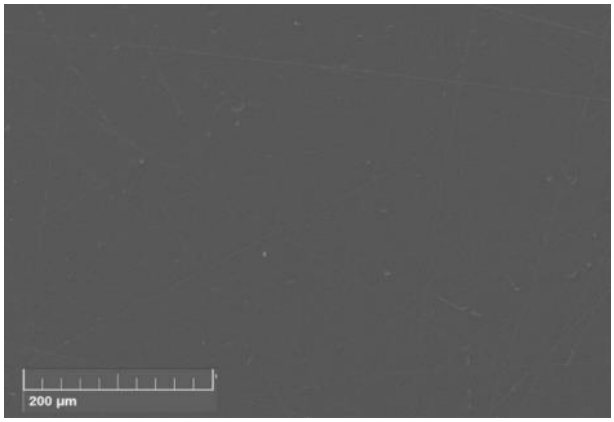

Figure 3.1: SEM image of the CZT wafer surface after cutting, polishing, and chemo-mechanical etching.

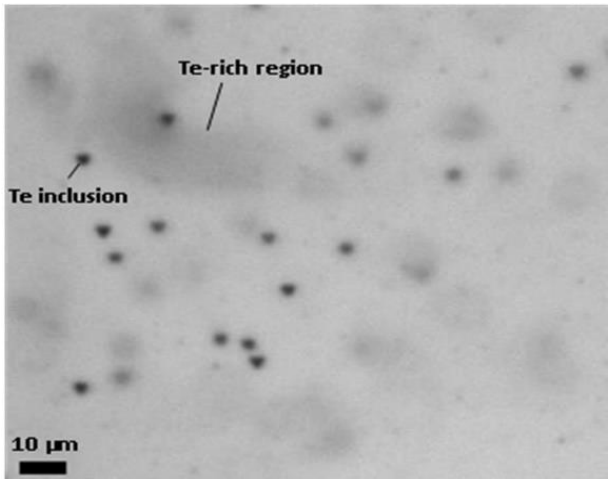

Figure 3.2: IR transmission image of the CZT crystal showing Te inclusions.

3.4 Compositional Characterizations

The composition of the ingot was analyzed by energy-dispersive x-ray spectroscopy (EDS). EDS mapping data were collected using a high-resolution Tescan Vega3 SBU scanning electron microscope (SEM) equipped with EDS integration software. The EDS mapping was carried out over a large surface area to study the compositional uniformity and elemental distribution. The surface is hit with high-energy electrons from the SEM using a very high voltage beam of 10 kV. The inner-shell electrons of the surface atoms may be excited and ejected from the material. This creates an electron-hole pair. As electrons from the outer shell fill the holes created by the excited inner-shell electrons, x-rays are generated. The x-ray energies are detected and measured by the system. The energy of these x-rays is the energy between the two shells and the characteristic of the atoms in which this occurred. Hence, these peaks on the EDS spectra appear based on those energies. By integrating the peaks corresponding to the major elements present and taking the ratio of the area under the peaks, the percent element concentration of a sample can be

determined. Figure 3.3 shows the position of the CZT samples on which EDS analysis was performed. Sample # (a) was collected from a location near the top of a solution-growth CZT ingot and sample # (b) was collected towards the tip of the ingot. The EDS spectrum shown in Figure 3.4 corresponds to that obtained from the top and close to the tip portion of the crystal. A thin layer (~5-7 µm) of gold was deposited on top of the sample as the SEM required a conductive surface and CZT is generally a non-conductive surface. So, Au was detected in the EDS spectra. Table 3.1 shows the obtained atomic and weight percentage of the elements without considering Au. A slightly Te rich composition was observed for the sample # (a), which is expected from the excess Te used during the growth. It can also be seen that Zn concentrations for samples 2 and 3 are close to 5%. the EDS data suggests that stoichiometric CZT crystals can be collected from the middle to lower region of the grown CZT ingot.

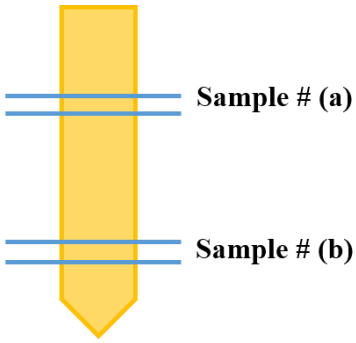

Figure 3.3: Sample positions inside the grown ingot for EDS analysis.

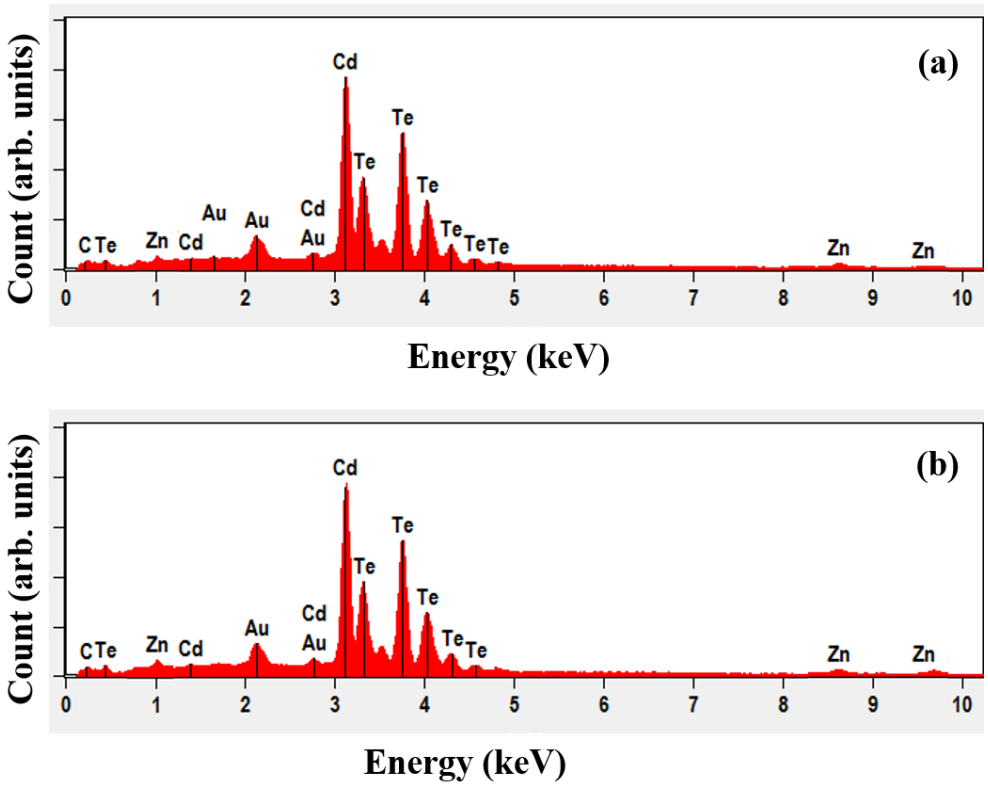

Figure 3.4: EDS spectrum of the two samples; (a) for the sample collected from the top side of the ingot, and (b) for the sample collected near the tip of the ingot.

Table 3.1: Summary of the EDS measurements on CZT.

		Zn	Cd	Te
Sample # (a)	Weight %	2.97	43.52	53.50
	Atom %	5.34	45.44	49.22
Sample # (b)	Weight %	3.12	43.61	53.26
	Atom %	5.60	45.47	48.93

X-ray photoelectron spectroscopy (XPS) measurements were performed to analyze the chemical composition of the grown CZT crystals. In this experiment, photons of known energy, are bombarded on the surface of the material. Once the energy is absorbed by the

material's atoms, this leads to ionization and emission of an inner shell electron into the vacuum environment. Every element exhibits specific binding energies associated with its atomic orbits. Hence, each element will give rise to specific peaks in the XPS spectrum depending on the photon energies and binding energies. The XPS system uses a monochromatic x-ray source which is AlKα x-ray source which has a wavelength of 0.83386 nm. The element and electron core level related to these counted photoelectrons can be determined by subtracting the binding energy of the detected photoelectrons from the kinetic energy.

Figure 3.5 shows the survey scan of a CZT crystal in the binding energy range 0 – 1300 eV. Except for the contaminants carbon and oxygen, no significant impurities were found. The high-resolution core-level spectra of Cd 3d, Zn 2p, and Te 3d orbitals were acquired to determine the oxidation states of the constituent elements and are shown in Figure 3.6(a)-(c). Cd 3d core-level spectra showed a doublet separated by 6.8 eV ($3d_{3/2}$ at 411.9 eV and $3d_{5/2}$ at 405.2 eV), which are consistent with the binding energy [76, 77]. Zn 2p core-level peaks appeared at 1044.7 eV and 1021.6 eV corresponding to $2p_{1/2}$ and $2p_{3/2}$ respectively with a 23.1 eV peak separation [78, 79]. A peak separation of 10.40 eV was found for Te 3d ($3d_{3/2}$ at 583.0 eV and $3d_{5/2}$ at 572.6 eV) [76, 77, 80].

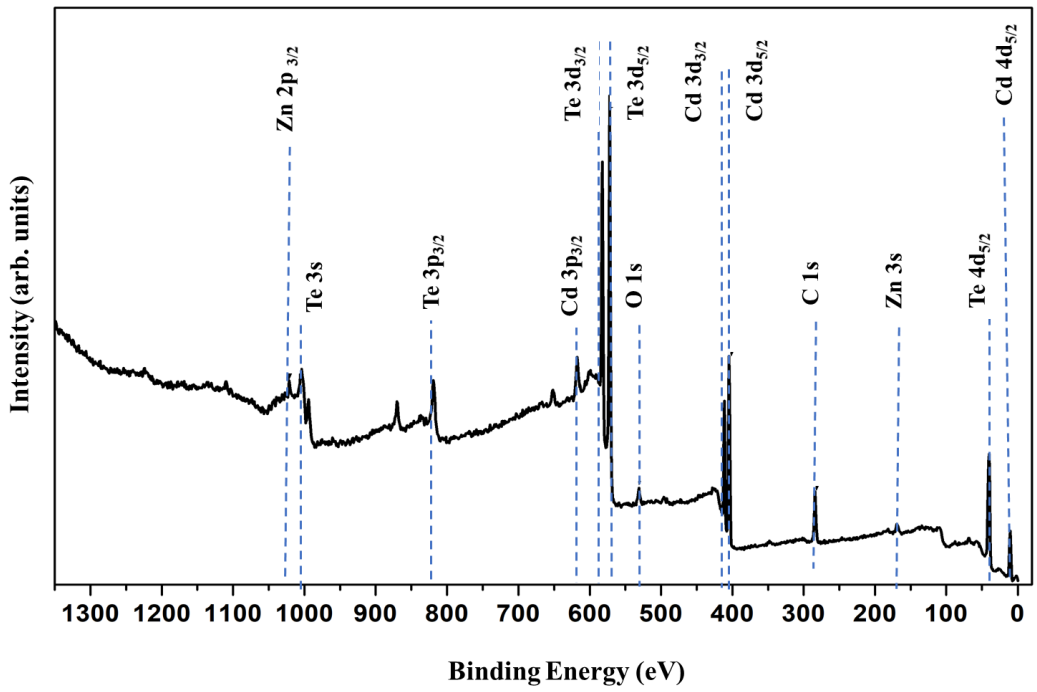

Figure 3.5: The survey scan of a CZT crystal in the binding energy range 0 – 1300 eV.

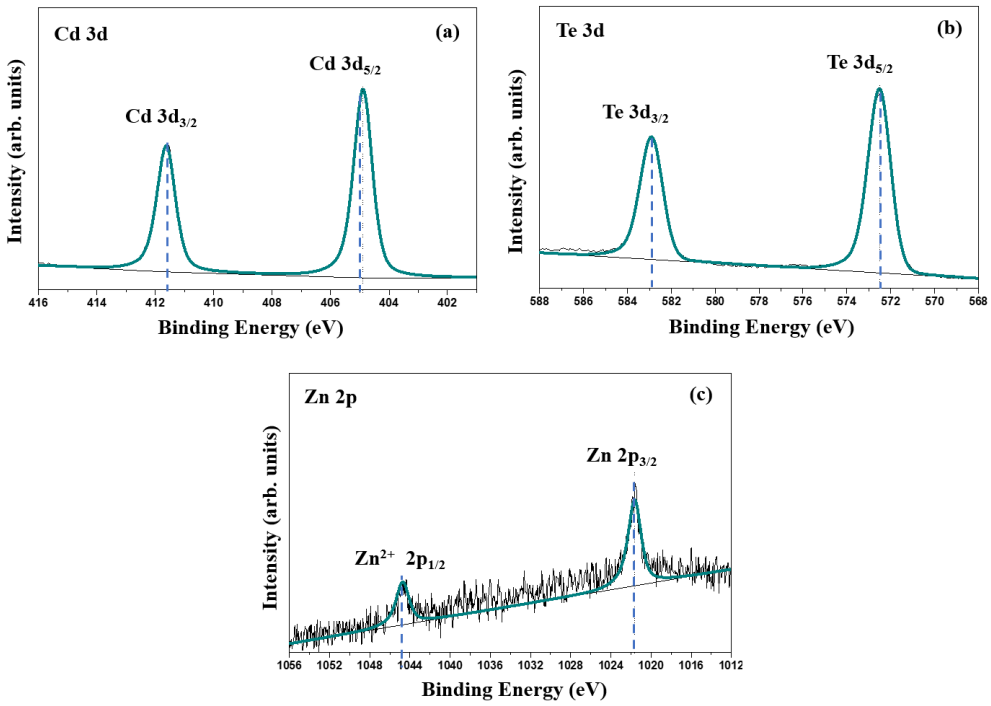

Figure 3.6: High resolution XPS spectra of (a) Cd 3d, (b) Te 3d, and (c) Zn 2p levels.

3.5 Electrical Characterizations

The current-voltage (I-V) characteristics of a metal-semiconductor junction are determined by the barrier height (ϕ_b) at the interface. An Ohmic contact produces a linear current-voltage response as it has no barrier. However, a rectifying contact produces a non-linear response. Very few metals will produce an Ohmic contact for p-type CZT, as CZT has a large semiconductor work function. For p-type Ohmic contacts on CZT, gold (Au) is one of the ideal choices due to high work functions of 4.8 eV. N-type CZT has higher compatibility with Ohmic contacts created by low work function (ϕ_m) metals such as Al and In, however n-type CZT does not commonly have the high resistivity required for nuclear detectors. The semiconductor work function (ϕ_s) and the barrier height (ϕ_b) can be found from the following equations:

$$\phi_b = \phi_m - \phi_s \qquad 3.1$$

$$\phi_s = \chi + (E_c - E_F) = \chi + \frac{E_g}{2} \qquad 3.2$$

where E_c is the conduction band level, E_F is the Fermi-level, E_g is the bandgap, and χ is the electron affinity.

The current-voltage (I-V) measurements for leakage current and resistivity determination were done using a Keithley 237 source-meter on planar gold contact (parallel to (111) crystallographic planes) deposited on the crystal. From the slope of the linear I-V plot, the resistance of the CZT material was determined. The resistivity from the I-V plot was calculated using the following equation:

$$\rho = R \,.\frac{A}{L} \qquad 3.3$$

where R is the resistance in Ohms (Ω), ρ is the resistivity of the crystal in Ω-cm, L is the thickness of the CZT crystal in cm, and A is the contact area (cm^2). From the inverse slope of the line using a linear fit of the Ohmic I-V plot, the resistance R was calculated.

Figure 3.7 shows the I-V characteristic on a planar configuration by applying the bias on the Te rich face. The planar device was fabricated by depositing the Au layer of 10 µm on the top surface and 50 µm on the bottom surface. The resulting curve revealed an asymmetric behavior to the bias polarity. The leakage current was found to be ~50 nA at +500 V and ~20 nA at -500V. In terms of leakage current density, the corresponding values translate to 2500 nA/cm^2 and 1000 nA/cm^2 respectively considering a pixel area of ~0.02 cm^2. The bulk resistivity was found to be ~5×10^{10} Ω-cm from a -1 to +1 V low range I-V measurement. Defect centers that act as carrier generation centers result in high leakage currents or low bulk resistivity of the detectors. The high bulk resistivity obtained for the present crystal suggests the growth of detector-grade crystals.

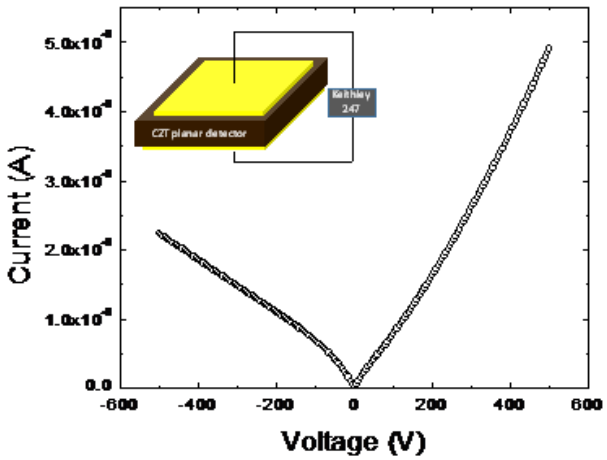

Figure 3.7: I-V characteristic of the CZT crystal in planar configuration with gold contacts.

3.6 Detector Structures

3.6.1 Planar Detector

Gamma-ray is electromagnetic radiation which has frequencies of above 10^{19} Hz and energies typically above 10 keV. For a radiation detector, the gamma photons interact with the detector material to produce fast-moving electrons within the detector. These electrons are collected by a front-end readout electronic circuit and converted into an electrical signal which provides the information about the radiation. Interaction between gamma-ray radiation and detector materials produce these fast electrons by one of three methods: photoelectric absorption, Compton scattering, and electron-positron pair production. The primary mechanism is photoelectric absorption where, a photoelectron is ejected from one of the atom's electron shell, with an energy E_{e-}, given by:

$$E_{e-} = h\nu - E_b \qquad 3.4$$

where h is the Planck's constant (~6.626×10^{-34} Js), ν is the frequency of the incident wave, and E_b is the binding energy of the electron ejected from the electron shell. A vacancy in the bound electron shell filled through either a free electron or rearrangement of electrons from the outer shells, which will cause the emission of x-ray photons. The x-ray photons will be absorbed within the detector material. The use of high Z materials increases the probability of interaction of the gamma-ray or x-ray with the material. Therefore, materials with high atomic number such as cadmium zinc telluride are highly considered for gamma-ray detection applications.

Compton scattering occurs due to the deflection of the incident x-ray or gamma-ray photon from its original path by an interaction with an electron. The photon loses energy as the electron is ejected from its orbital position. The deflected photon continues to travel through the material along an altered path. This resultant energy shift depends on the angle of scattering at the interaction. Energy and momentum are conserved here. The scattered x-ray photon has less energy and it has a longer wavelength which is less penetrating than the incident photon. The change in the wavelength of the photon due to scattering is given by:

$$\nu' - \nu = \frac{h}{m_e c}(1 - cos\theta) \qquad 3.5$$

where, ν' is the wavelength of scattered x-ray photon, ν is the wavelength of incident x-ray photon, m_e is the mass of an electron at rest, c is the speed of light, θ is the scattering angle and h is the Planck's constant. The rest-mass energy of an electron is 1.02 MeV. Gamma-rays that have energy above 1.02 MeV will undergo pair production which generates an electron-positron pair.

For a planar detector as shown in Figure 3.8, gamma-rays induce a charge, q, within the detector material. The charge seen at the readout electrode (anode), Q, differs from q due to movement of the charge within the semiconductor. Shockley-Ramo theorem relates the two charges by the electric potential (also known as weighting potential) and electric field [81]. The evolution of charge Q and current i on an electrode induced by a moving point charge q are given by:

$$Q = -q * \varphi_0(z) \qquad 3.6$$

$$i = qv \cdot E_0(z) \quad 3.7$$

where, $\varphi_0(z)$ and $E_0(z)$ are the electric potential and field that would exist at q's instantaneous position *z,and v* is instantaneous velocity. For a planar detector with no hole and electron trapping/loss, the charge can be found by [82]:

$$\Delta Q = -(ne_0)(0 - Z) + (ne_0)(1 - Z) = ne_0 \quad 3.8$$

where *Z* is the interaction depth, e_0 is the electronic charge, and *n* is the number of electron-hole pairs generated. The performance of CZT based detectors in a planar configuration is limited by the poor hole transport properties. As shown in Figure 3.9, when electron-hole pair is generated away from the cathode, some of the holes are lost due to the presence of defects before reaching the cathode. This leads to partial charge collection for the planar device. Hence, CZT planar devices exhibit low drift-mobility and short lifetimes for holes which lead to poor energy resolution.

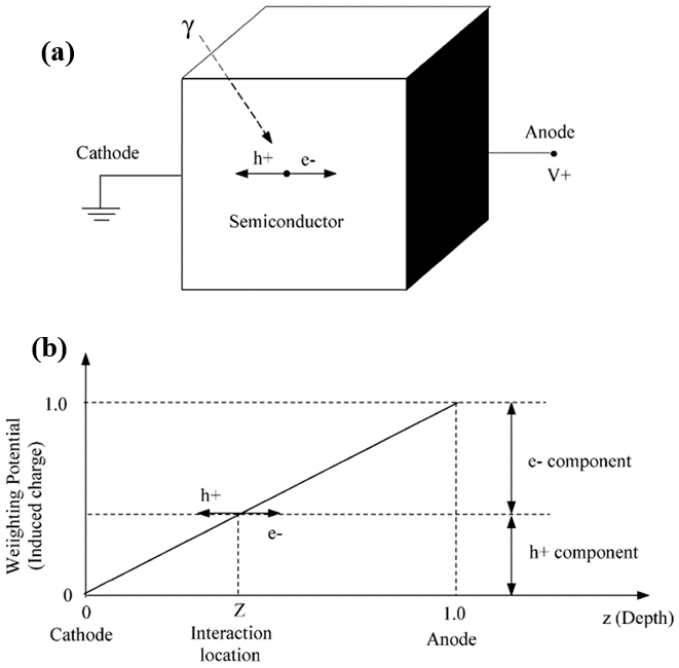

Figure 3.8: (a) Schematic of a planar detector working principle, and (b) the weighting potential distribution of planar detector [81].

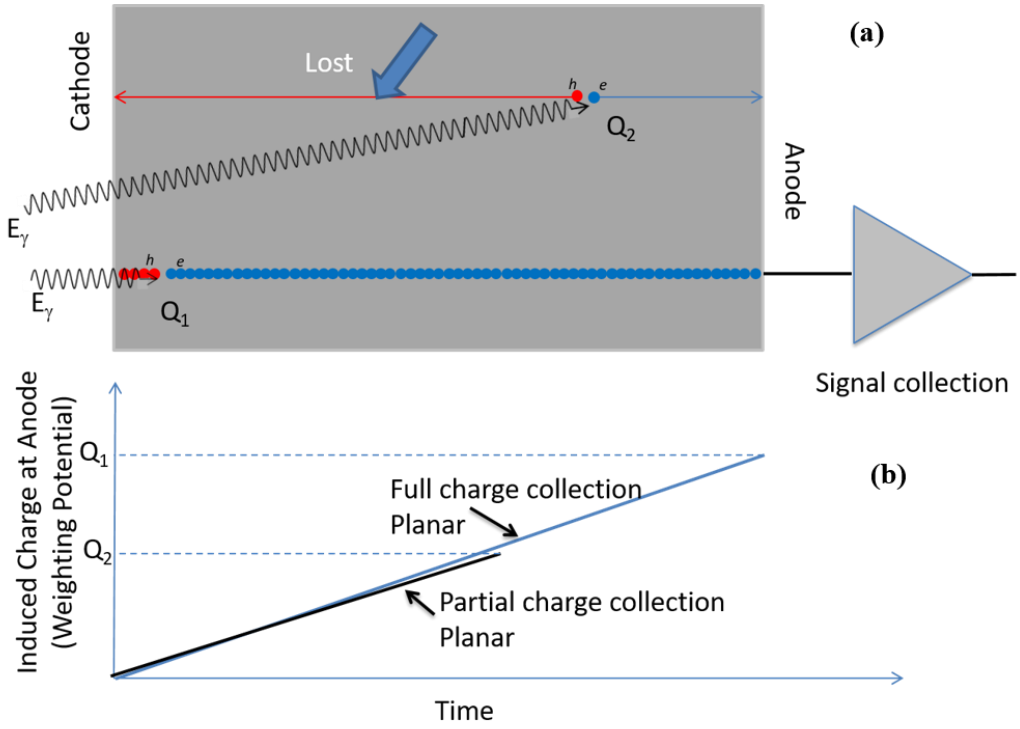

Figure 3.9: Limitations of planar detector: (a) holes can get lost before reaching the cathode, and (b) the weighting potential loss due to partial charge collection [81].

3.6.2 Pixelated Detector

To achieve a single-polarity charge sensing device, pixelated geometry can be applied as it can minimize the effect of poor hole transport properties [83]. In a small pixel detector, several smaller metal electrodes, separated by a gap, are placed on the detector in a geometric pattern. The induced charge Q and the weighting potential in a small pixel detector can be described by the following equation:

$$Q = q[1 - \frac{1-Z}{\sqrt{\alpha^2+(1-Z)^2}}) \quad 3.9$$

$$\varphi_0(z) = \frac{Q(Z=1-z)-Q(Z=0)}{Q(Z=1)-Q(Z=0)} \quad 3.10$$

where α is the ratio of the approximate pixel width to the detector thickness, Z is the distance the charge must travel to reach the anode, q is the electronic charge, and z is the interaction depth. When α is reduced, the weighting potential near the pixels at a distance of Z = 2α becomes far larger than 2α away from the pixels. This effect is referred as the small pixel effect.

To reduce the surface leakage current, a guard ring can be fabricated surrounding the pixels. Figure 3.10 (a) shows the fabricated pixelated structure on the CZT crystals. A 10 × 10 pixelated structure (anode) was fabricated on the Te rich faceusing photolithography as shown in Fig. 3.10 (b). The top contact (anode) is parallel to (111) crystallographic planes. Gold was evaporated to form 80 nm thick metallic electrical contacts. The dimension of each pixel is 1.3 × 1.3 mm^2 pitched at 1.9 mm. A square back contact (cathode) using gold was made on the opposite surface. To minimize the inter-pixel

and inter-electrode leakage current, a 0.05 mm wide grounding grid was fabricated on the anode side.

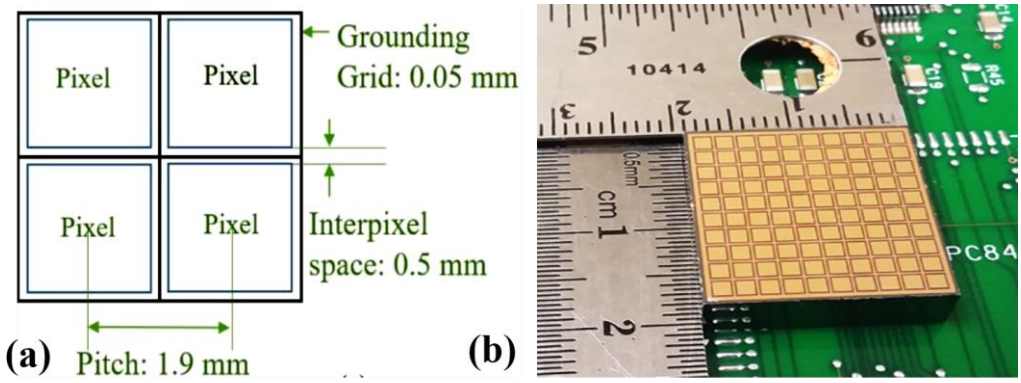

Figure 3.10: (a) Schematic of the pixelated detector showing four adjacent pixels and the various dimensions; (b) a photograph of the actual 10 x 10 pixelated detector fabricated in our lab on the grown polished crystal.

3.7 Radiation Detection

Pulse height spectroscopy (PHS) was performed to obtain ^{137}Cs gamma photon spectra. The guard ring was connected to the ground using a 25 µm (diameter) gold wire bonded using conductive epoxy. A movable arm was used to connect the pixels to the pre-amplifier in turns for collecting spectra from each pixel. The cathode was placed on a metallic pad on a PCB which was connected to a filter circuit for biasing. The radiation source was placed under the detector facing the cathode. The radiation detection measurement system is shown in the schematics of Figure 3.11, which is a hybrid system to record analog as well as digital data simultaneously. Both the system shares a charge sensitive CR110 (Cremat) preamplifier. The analog system uses an Ortec 671 shaping amplifier to filter the pre-amplifier pulses and obtain pulse-heights, which are then binned

using a Canberra Multiport II multichannel analyzer (MCA) driven by Genie 2000 user interface to obtain a pulse-height spectrum (PHS). The digital spectrometer on the other hand uses a fast NI digitizer card (PCI 5122) to digitize and store the raw pre-amplifier charge pulses. The digitizer card was controlled by a user interface program which allows us to acquire the pulses with the access to control the duration of the pulses, ADC resolution, etc. A program was developed in the LabVIEW platform to analyze the pre-amplifier pulses to determine the rise-times and filter the pulses with a CR-RC^4 shaping algorithm [84]. The pulse-heights were obtained from the shaped pulses.

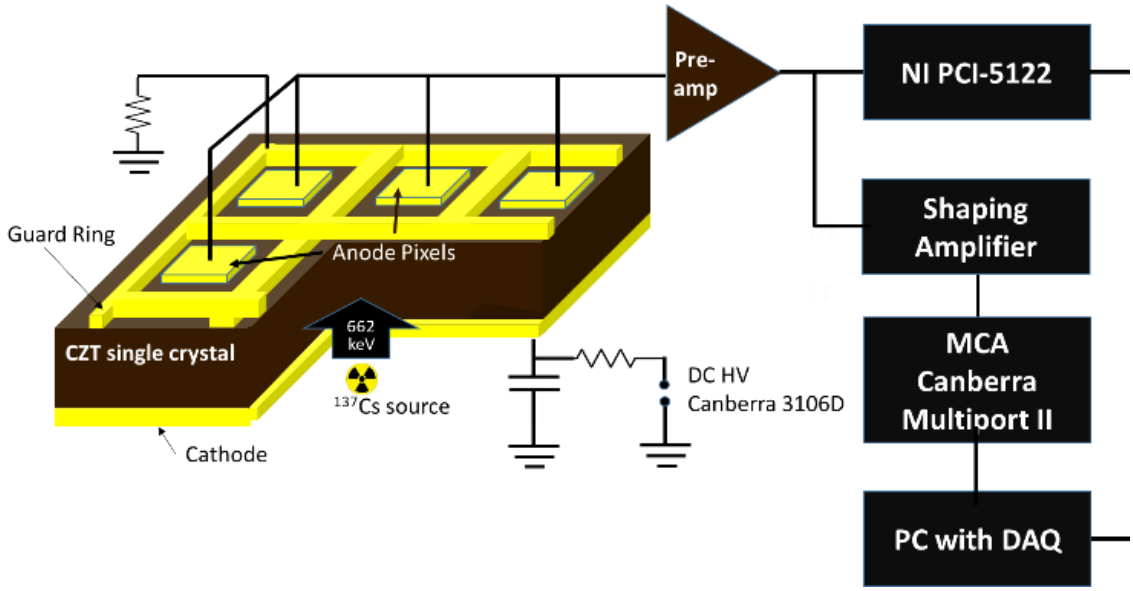

Figure 3.11: Schematic of the hybrid radiation detection set-up in our lab.

Figure 3.12 shows a pulse height spectrum obtained using a ^{137}Cs (662 keV) gamma source of a random pixel from the 10 × 10 arrays. A bias of -1500 V (3000 V/cm) was applied to the planar contact and the guard ring was connected to ground during

measurements. The photo-peak corresponding to the 662 keV gamma-ray was found to be well resolved from the Compton background. The Compton edge was well-defined, and the backscattered peak was also identified in the PHS. The energy resolution was calculated from the following equation:

$$\%\, Energy\ Resolution = \frac{FWHM\ (keV)}{Incident\ Energy\ (keV)} \times 100\% \qquad 3.11$$

where FWHM is the full width at half maxima of the photopeak and incident energy is the centroid of the photopeak observed. The energy resolution was found to be ~1.6% for 662 keV gamma-ray which can be categorized as a very high-resolution for CZT based detectors. The peak-to-background (P/B) and the peak-to-valley (P/V) ratio was calculated to be ~2 and ~10 respectively. In a separate study, the average electron mobility-lifetime ($\mu\tau$) product in planar configuration was calculated to be ~6×10^{-3} cm^2/V. All the above characteristics confirm the fabrication of a high-resolution detector. The photopeak, although well resolved, appears to be slightly asymmetric as a tailing at the lower energy side was observed. Figure 3.12 also shows the pulser peak recorded along-with the ^{137}Cs PHS. The FWHM of the pulser peak, which shows the overall electronic noise of the spectrometer, was calculated to be 3.6 keV for the above-mentioned pixel. The overall electronic noise was seen to vary from pixel-to-pixel with values ranging from 3.34 to 4.34 keV.

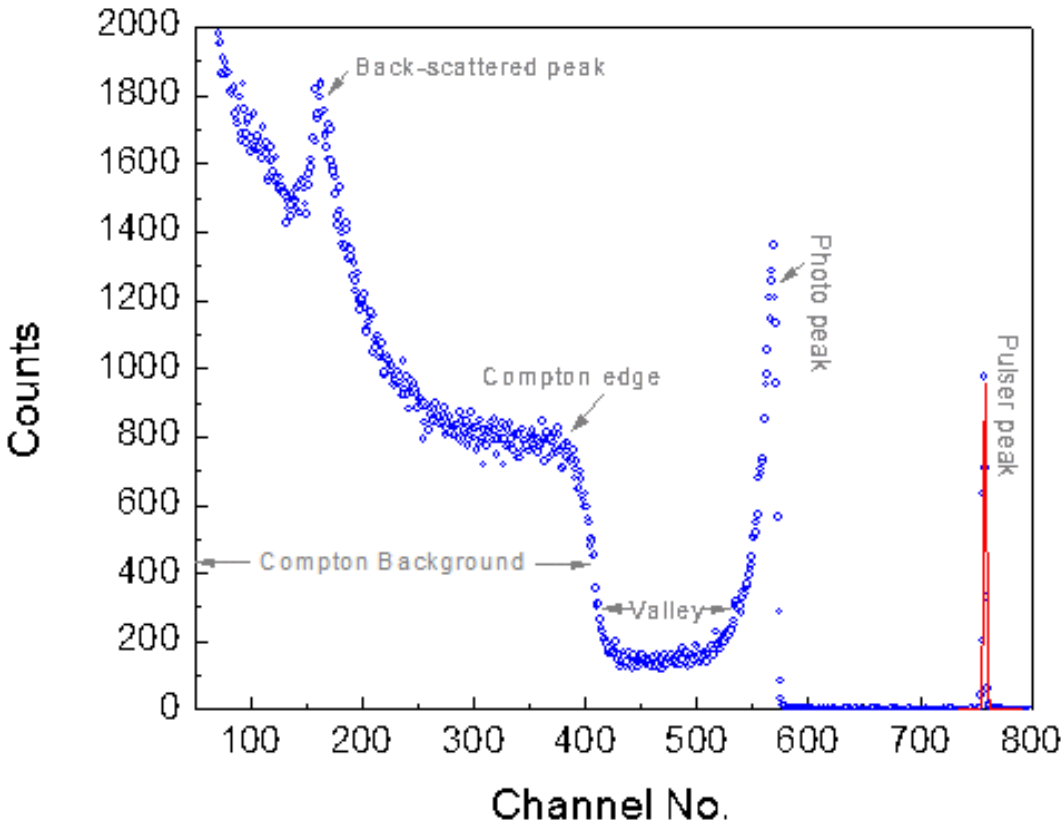

Figure 3.12: A ^{137}Cs pulse height spectrum obtained using one of the pixels with the cathode biased at -1500 V. A pulser peak was also acquired in the PHS.

Ideally, a gamma photon pulse-height spectrum should present a peak-to-valley ratio equal to the number of counts at the photo-peak position after proper background subtraction. An actual PHS obtained from CZT detectors however always shows a lower P-V ratio because of the tailing at the lower energy side of the photopeak. Such tailing of photopeaks is generally attributed to ballistic deficit due to trapping of holes in defect centers [4, 69]. It should be noted that in the present situation, the detector, being a single-polarity (electron) sensing device, is not supposed to be affected by the hole movement. With a pixel dimension of $\varepsilon \times \varepsilon$, a transiting electron is not supposed to induce any charge on the collecting pixel until it is within a distance $z \approx \varepsilon$, which in this case is 1.3 mm. The

degree to which a small-pixel effectively works depends on the pixel-dimension to the detector-width ratio (ε/L), L being the detector thickness. The smaller the ε/L ratio is, the higher is the effectiveness of the single-pixel effect [83]. For the present detector, the ε/L ratio is 0.26. According to the calculations [84], it can be estimated that with an ε/L ratio of 0.26, the charge induced by an electron created as close as 1 mm from the anode pixel is 90% of the total charge induced, the rest 10 % being due to the holes. Thus, a fraction of the signal induced at the anode, even though small, is due to hole transit also, which accounts for the tailing at the lower energy side of the 662 keV photopeak given in Figure 3.12.

Not all the pixels however produced the equal quality of gamma-ray spectra for ^{137}Cs source. Nonuniformity in CZT crystals is a common problem and is known to cause nonuniform charge collection efficiency [75], especially in large-area crystals [85]. The spatial variation of detector properties of large-area crystal grown under a similar growth condition has been published elsewhere [86]. In the present detector, the variation of pixel-to-pixel percentage resolution was observed to be in the range of 1.6 to 5.7 %. The pixels with lower resolution exhibited even higher tailing resulting in a low peak-to-valley ratio. Figure 3.13 shows such a pulse height spectrum from one of the pixels which exhibited relatively higher leakage current. The P/V ratio and the P/B ratio were found to be ~1.2 and ~6 respectively for this particular pixel. The prominent lower energy tailing of the photopeak is indicative of the even higher degree of hole trapping which in turn suggests a greater concentration of hole traps beneath this particular pixel. Which is why the leakage

current from this particular pixel was found to be higher. This also suggests a non-uniformity in the distribution of trap centers across the length and width of the detector.

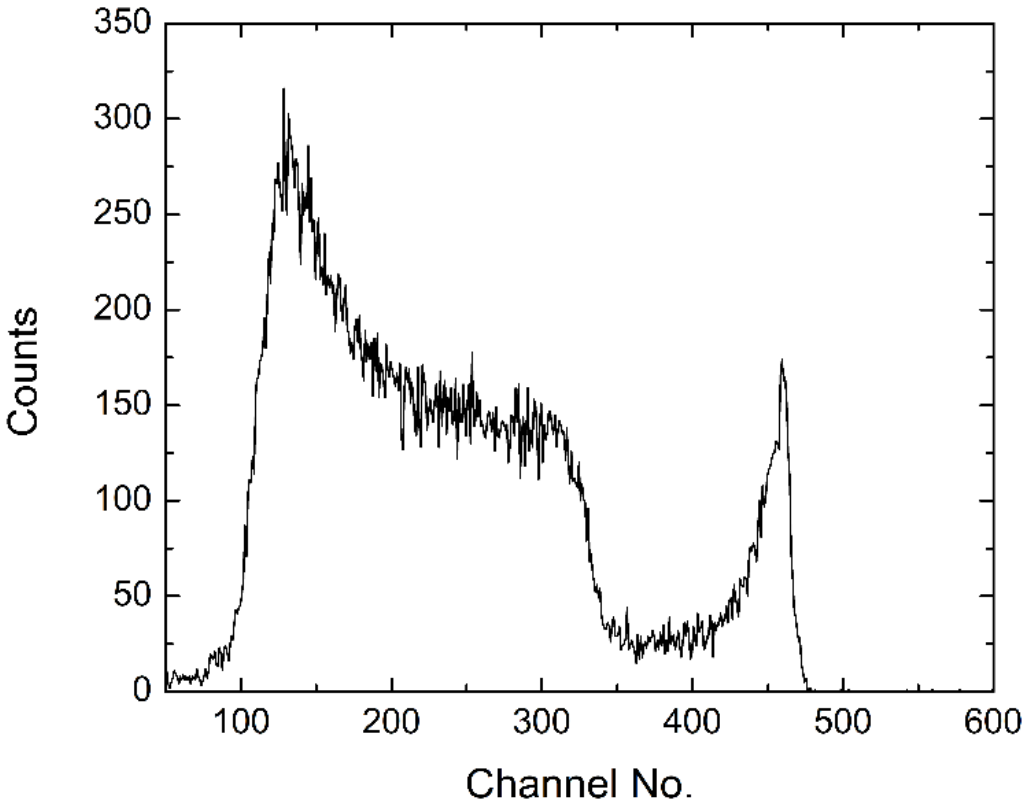

Figure 3.13: A ^{137}Cs pulse height spectrum obtained using one of the pixels with a lower P/V ratio, with the cathode biased at -1500 V.

3.8 Correction of Pulse-Height Spectra

Biparametric (BP) plots are a convenient way to correlate the pulse-heights to the rise-times of each pulse obtained from detectors in a planar configuration. In the present situation, however, the BP plot is obtained in a detector with a single polarity charge sensing configuration. But as has been argued in the previous section, the resultant signal still has some charge transition in the neutral region shown in Figure 3.13, a phenomenon

commonly referred to as grid inefficiency in virtual Frisch grid detectors [30]. Higher the grid inefficiency higher is the effect of the transit of charge carriers in the neutral region. Hence, the following discussion will be under the premise that the movement of electrons (and holes) affects the signals from this particular pixel throughout the detector thickness because of finite grid-inefficiency.

In a BP plot, the pulse-heights depict the amount of charge induced on the collecting electrode of the radiation-induced charges and hence reveal the degree of ballistic deficit. A complete charge collection occurs when there is either no trapping or trapping followed by de-trapping. Pulses obtained from such cases exhibit the highest pulse-heights. In the case of permanent trapping, the radiation-induced charge pairs induce a partial charge on the collecting electrode and hence charge pulses with lower pulse-heights are obtained. The pulse height depends on the position at which it recombines. The closer it comes to the collecting electrode before it recombines, the higher is the induced charge. The rise-times on the other hand give an estimate of the depth of interaction. Charge pairs produced close to the anode will be collected faster than the ones created near the cathode. Hence, the pulses in the former case will have much faster (short) rise-times than the ones in the latter case. The argument holds good only if the transport properties of the electrons and holes are comparable. In CZT, the hole transport properties viz. drift mobility and carrier lifetimes, are at least an order of magnitude lower than those of electrons [3, 87, 88].

Figure 3.14 shows the biparametric plot obtained from the pixel under consideration. The events from the 662 keV gamma photon interactions could be easily identified as the curved bunch of events visible at the right side of the plot. These events

are well distinguished from the rest of the points which are due to the Compton interaction within the detector volume. The 662 keV events show that a substantial portion of the collected pulse has lower rise-times as well as pulse-heights indicating permanent hole trapping. These events, in the bent portion of the correlated events, are responsible for the lower energy tailing.

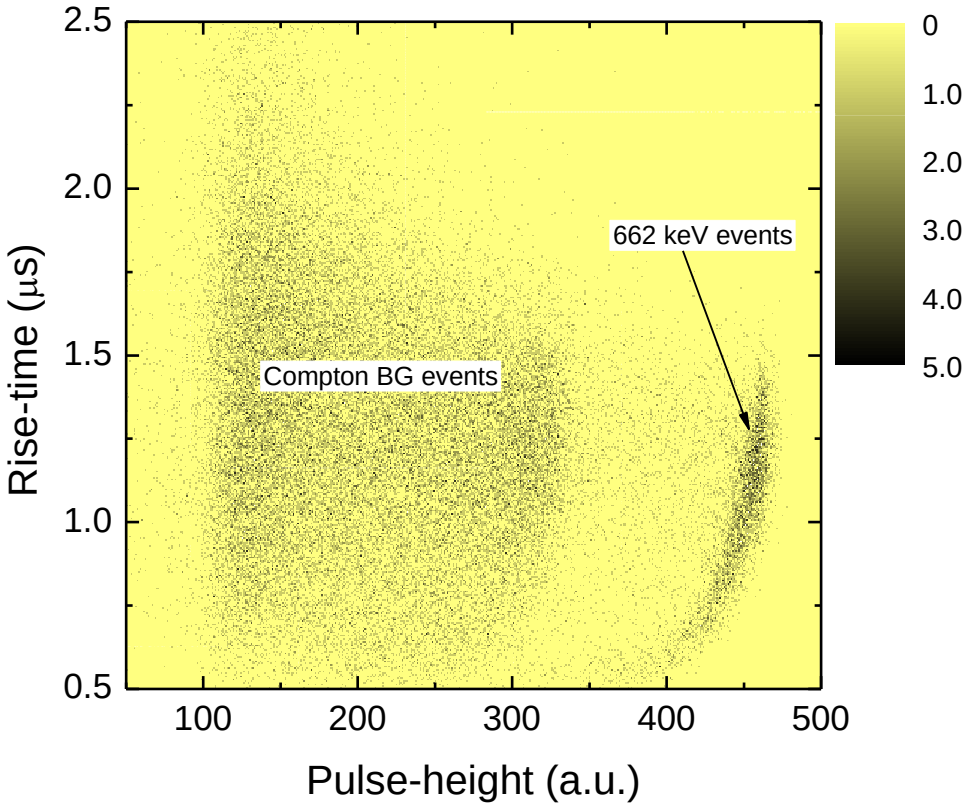

Figure 3.14: Biparametric plot obtained for a ^{137}Cs exposure from a pixel with a lower P/V ratio.

In BP plots obtained from CZT detectors it is generally seen that for the 662 keV events, the pulses with higher rise-times exhibit relatively lower pulse-heights. The higher rise-times are indicative of the low hole mobility and the corresponding lower pulse-

heights indicate ballistic deficit. In the present case, the 662 keV events however showed rather different behavior. The pulses with lower rise-times had lower pulse-heights for the 662 keV events. Such pulses could result from interactions in the active region and very close to the anode. In those cases, the charge pulses primarily consist of hole movements, that too in the active region only, resulting in pulses with very low pulse-heights and naturally short rise-times. The interactions of 662 keV gamma-rays in the active region is only natural as it could be estimated that a substantial fraction of these gamma photons could pass the entire 5 mm thickness of the detector without being completely stopped.

More insight into the trapping of charge carriers can be obtained from the depth-wise binning of pulse height spectra obtained from the BP plot. Figure 3.14 shows such a plot obtained for the present pixel. The BP plot was sliced into ten slices each for a certain interval of rise-times. Slice #10 represents the interval with the highest rise-times and slice # 1 represents the interval with the lowest ones. It could be seen from Figure 3.15 that slices # 1 and # 4 showed very broad photo-peaks with very low P/B ratios. The broadening of the photopeak in these slices could be attributed to the uncertainty in pulse-height measurement due to lower signal-to-noise ratio for pulses with lower pulse-heights. Besides, the average photopeak positions of these slices are also centered at lower channel numbers compared to the slices # 5-10, which can be attributed to the effect of the ballistic deficit. The slices # 2 and # 3 on the other hand showed only noise and Compton background but hardly any trace of photopeak. All these factors led to the lower energy tailing of the photopeak. Figure 3.16 shows the pulse-height plot of the slice # 9 which is indicative of the quality of ^{137}Cs spectra had there been no hole trapping. A percentage

resolution of 2% at 662 keV was found and the P/V and P/B ratio were calculated to be ~2 and ~14, respectively.

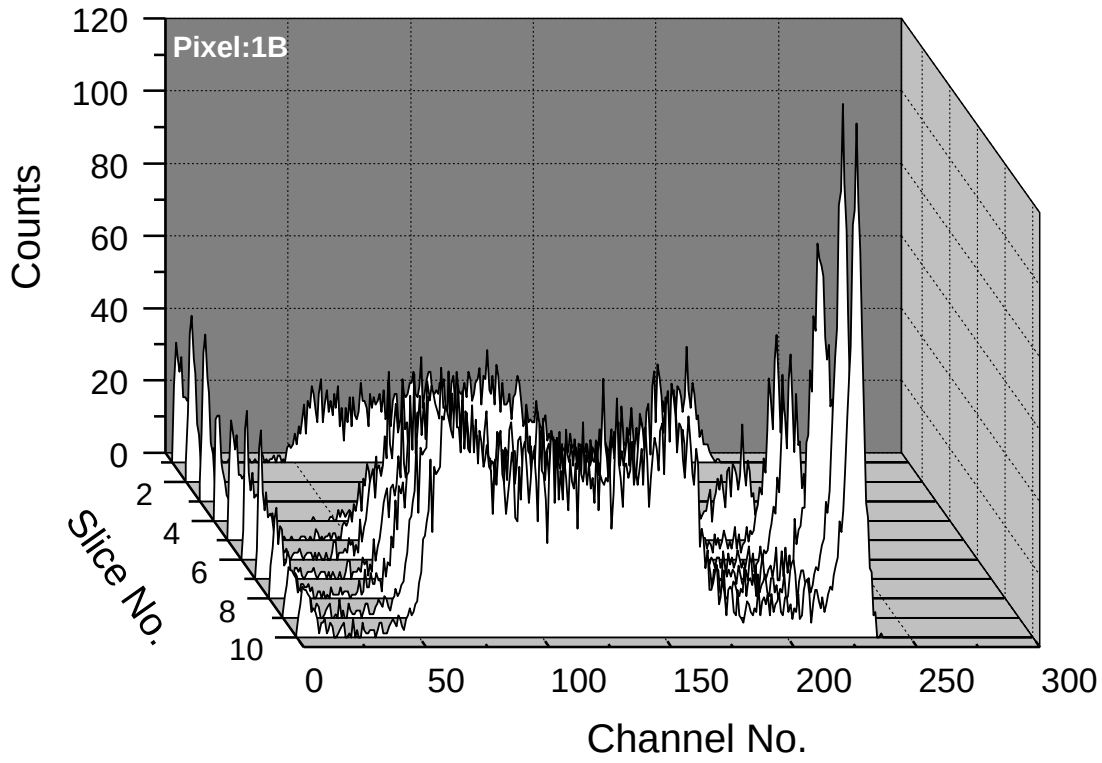

Figure 3.15: Depth dependent binning of ^{137}Cs pulse height spectra obtained from one of the pixels with high leakage currents.

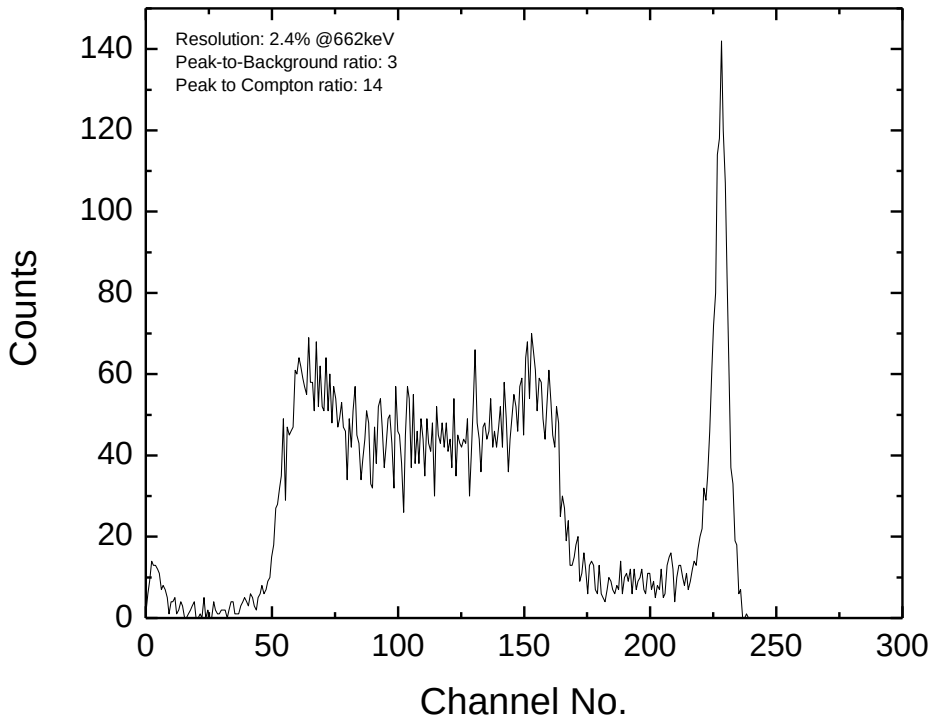

Figure 3.16: ^{137}Cs pulse height spectrum obtained from one of the slices of the depth-dependent binning shown in Figure 3.15.

CHAPTER 4

CZTS DETECTOR FABRICATION AND PERFORMANCE ANALYSIS

4.1 Introduction

Recent break-through studies in 2019 have shown that the inclusion of Se to the CZT matrix can lead to a reduction of the density of Te inclusions. It has also found to reduce the formation of subgrain boundaries [5, 6]. In this chapter, we will discuss the fabrication and characterization of $Cd_{0:9}Zn_{0:1}Te_{0:97}Se_{0:03}$ (CZTS) based planar gamma-ray detectors. The experimentally measured mobility-lifetime product and drift mobility for holes in CZTS based radiation detectors are shown. The investigations of the effect of charge carrier trapping on the overall detection performance are also presented by correlating the depth of interaction of a gamma photon in the detector to the height of the corresponding charge-pulse produced by the detector.

4.2 Crystal Surface Preparation

Unwanted surface features on the crystal can lead to higher leakage current and surface charge trapping centers. Hence, it is essential to polish the crystal surface to remove the defects, scratches, and other unwanted features. After the completion of CZTS crystal growth, the CZTS ingot was taken out and cut into square/rectangular shapes using a wafer cutter “Extec Labcut 150” with different dimensions. The cut crystals were grounded and lapped using a series of SiC sandpapers (up to 1500 grit sandpaper). Sandpapers are used

to get rid of varied landscapes, which are present after the wafer saw cutting procedure. Then the surface was polished with 0.3 µm and 0.05 µm alumina powder using microfiber pads. This gradual sanding and polishing help to work with decreasing ridges and certain other formations even smaller in depth till they disappear altogether. Then the surface was cleaned using an ultrasonicator for 1 minute. The crystal is then chemo-mechanically etched using a 5% Bromine-Methanol solution (Br_2-CH_3OH) for 1 minute and finally rinsed off with de-ionized water. The chemo-mechanical polishing reacts with Cd and helps to remove the cadmium oxide (CdO) on the surface by forming Cadmium bromide ($CdBr_2$) and the surface layer are also enriched by Te [73-75].

4.3 Optical Characterizations

The bare polished crystals were characterized using a scanning electron microscope (SEM) for examining surface morphology. Figure 4.1 shows an SEM image of the surface as an example of CZT sample after polishing. SEM image confirms a very smooth surface morphology with minimal structural defects. A smooth surface finish ensures the deposition of quality metal contacts with a uniform thickness which in turn provides reliability and repeatability of measurements.

One of the major issues which can affect CZTS crystal quality grown using either stoichiometric or with excess Te is the presence of Te inclusions and precipitates uniformly distributed in the bulk crystal. The Te-rich regions can act as defects that degrade the electrical properties of the CZTS material. The Te inclusions/precipitations of the bare polished crystal were investigated through infra-red (IR) transmission imaging by using a 75 W high stability Xenon arc lamp. As the bandgap of Te is ~0.3 eV, which is much lower

bandgap than that of CZTS, the infrared light will pass through the sample except at the locations of Te-rich sites within the crystal. Figure 4.2 shows the IR transmission image of the bare crystal surface. The average Te inclusions/precipitations size was found to be less than ~10 µm in the crystal which confirms the growth of good detector grade crystals. Bigger sized Te inclusions act as charge trapping centers leading to permanent charge loss [76, 77].

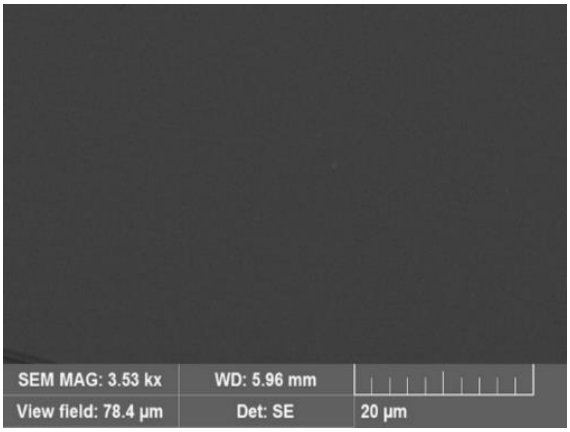

Figure 4.1: SEM image of the CZTS surface after cutting, polishing, and CMP etching.

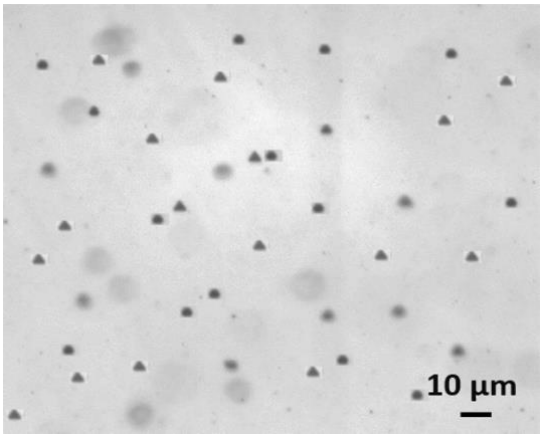

Figure 4.2: IR transmission image showing Te inclusions/precipitates.

4.4 Compositional Characterization

EDS measurements at different spots along the crystal growth direction were carried out. The EDS spectrum is shown in Figure 4.3 corresponds to that obtained from the middle portion of the crystal. A slightly Te rich composition was observed, which is expected from the excess Te used during the growth. The weight and atomic percentages of the individual elements are given in Table 4.1. The atomic ratio of Cd/Te was found to be 0.88, which is close to the expected value of 0.947 for the stoichiometric condition. The atomic ratio of (Cd+Zn)/(Te+Se) was calculated to be 0.903. The elemental composition was observed not to vary noticeably along the growth direction, which clearly implies higher crystal growth yield.

Table 4.1: Summary of the EDS measurements on CZTS

	Zn	Se	Cd	Te
Weight %	2.55	2.54	41.43	53.47
Atom %	4.54	3.75	42.92	48.79

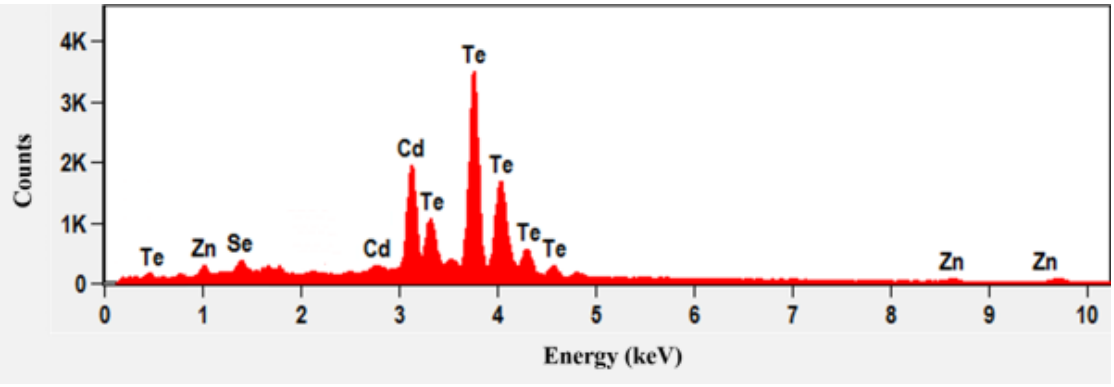

Figure 4.3: Energy dispersive x-ray spectroscopy of the grown CZTS crystal.

X-ray photoelectron spectroscopy (XPS) measurements were performed to analyze the chemical composition of the grown CZTS crystals. In this experiment, the XPS system uses a monochromatic x-ray source which is Al Kα x-ray source which has a wavelength of 0.83386 nm. the element and electron core level related to these counted photoelectrons can be determined by subtracting the binding energy of the detected photoelectrons from the kinetic energy. Figure 4.4 shows the survey scan of a CZTS crystal in the binding energy range 0 – 1300 eV. Except for the contaminants carbon and oxygen, no significant impurities were found. The high-resolution core-level spectra of Cd 3d, Zn 2p, Te 3d, and Se 3d orbitals were acquired to determine the oxidation states of the constituent elements and are shown in Figure 4.5(a)-(d). Cd 3d core-level spectra showed a doublet separated by 6.8 eV ($3d_{3/2}$ at 412.0 eV and $3d_{5/2}$ at 405.2 eV), which are consistent with the binding energy [78, 79]. Zn 2p core-level peaks appeared at 1044.7 eV and 1021.6 eV corresponding to $2p_{1/2}$ and $2p_{3/2}$ respectively with a 23.1 eV peak separation [80, 81]. A peak separation of 10.40 eV was found for Te 3d ($3d_{3/2}$ at 583.0 eV and $3d_{5/2}$ at 572.6 eV) [78, 79, 82]. Multiple peaks appeared for Se $3d_{5/2}$ core level (54.7 eV, 53.9 eV and 52.5 eV). These peaks can be attributed to the binding energy of the $3d_{5/2}$ level of Se [89-91].

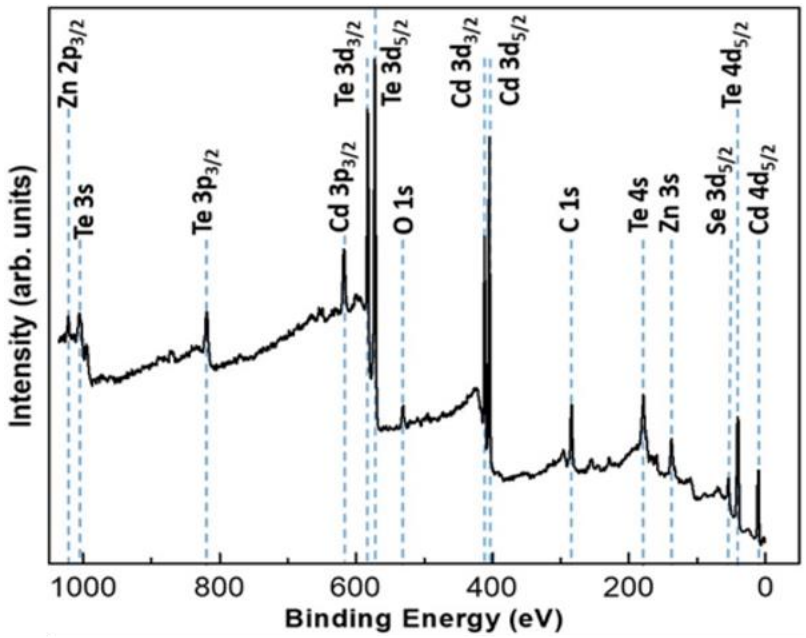

Figure 4.4: XPS survey scan of a CZTS crystal in the binding energy range 0 – 1050 eV.

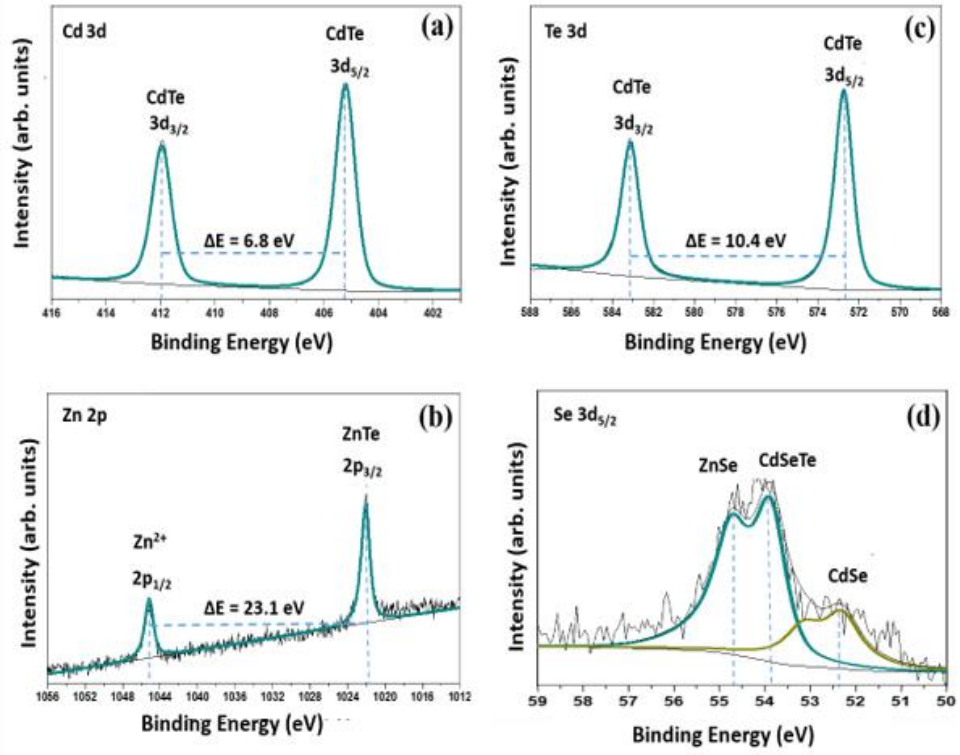

Figure 4.5: High resolution XPS spectra of (a) Cd 3d, (b) Zn 2p, (c) Te 3d and (d) Se $3d_{5/2}$ sub-levels.

To further investigate the CZTS crystal, the x-ray powder diffraction (XRD) analysis was performed. XRD is an analytical technique primarily used for phase identification of a crystalline material and can provide information on unit cell dimensions. The analyzed material is finely grounded, homogenized, and average bulk composition is determined. X-rays are generated in a cathode ray tube by heating a filament to produce electrons, accelerating the electrons toward a target by applying a voltage, and bombarding the target material with electrons. When electrons have sufficient energy to dislodge inner shell electrons of the target material, characteristic x-ray spectra are produced. The powder XRD pattern of the as-grown CZTS crystals is shown in Figure 4.6. Strong diffraction peaks at $2\theta = 24.01^{o}$, 39.71^{o} and 46.92^{o} corresponding to (111), (220) and (311) planes of CZTS structure were observed. As there was no reference to the particular stoichiometric composition for $Cd_{0.9}Zn_{0.1}Te_{0.95}Se_{0.05}$ in the JCPDS library, the obtained XRD peak planes were identified by comparing them with the XRD spectra of CdZnTe (JCPDS # 00-053-0552) and CdTeSe (JCPDS # 00-041-1324) as shown in Fig 4(b) and (c). Inset in Figure 4.6 shows the Gaussian fit of the strongest peak and the centroid position of (220) plane. From the Gaussian fit of the strongest peak (220) located at $2\theta = 39.71^{o}$, the full width at half-maximum (FWHM) was calculated to be $\sim 0.192^{o}$. The sharp diffraction peaks with small FWHM suggests high-quality single-crystal nature of the grown ingot. The lattice constant found from the XRD was a = 6.42 Å, which is very close to that obtained for CdZnTe (a = 6.424 Å) (JCPDS # 00-053-0552) and CdTeSe (a = 6.431 Å) (JCPDS # 00-041-1324).

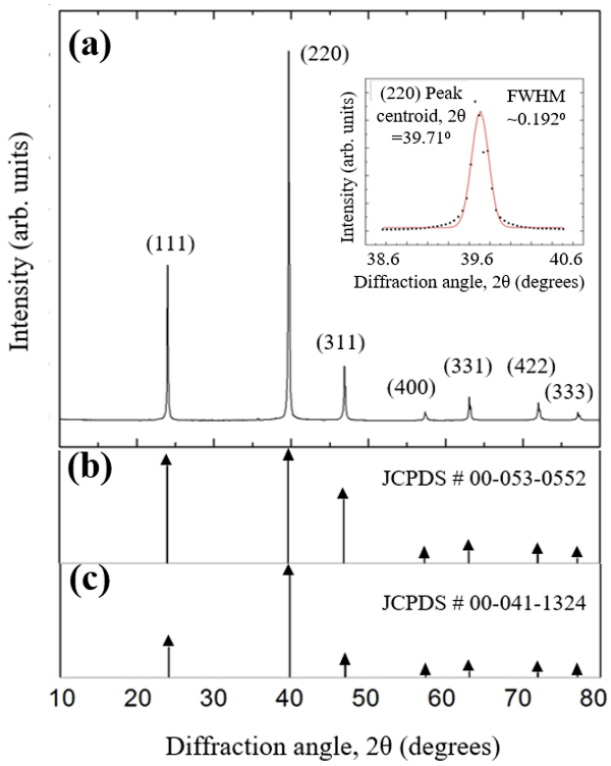

Figure 4.6: (a) Powder x-ray diffraction pattern of CZTSe ingot and JCPDS powder XRD peaks for (b) CdZnTe and (c) CdTeSe.

4.5 Electrical Characterizations

The nature of metal contacts regulates to a great extent the leakage current and the detector capacitance under operational conditions. Both these parameters affect the electronic noise performance of the pulse-height spectrometer. Regular current-voltage (*I-V*) and capacitance-voltage (*C-V*) measurements readily give information on these parameters. Circular gold contacts (20 nm thick and ~4 mm diameter) were deposited on each face (parallel to (111) crystallographic planes) of a $10\times10\times1$ mm^3 CZTS sample using a Quorum Q150T DC sputter coater. Figure 4.7 (a) shows a polished and cleaned crystal

with circular gold contact and Fig. 4.7 (b) shows a fabricated detector assembly mounted on a printed circuit board (PCB), that has been used for the present study.

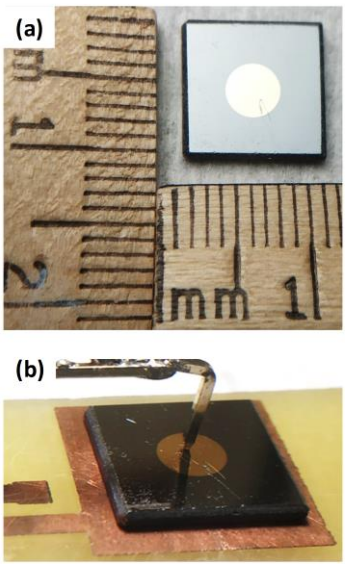

Figure 4.7: (a) A CZTS polished crystal with circular gold contact and (b) A planar CZTS detector mounted on a PCB.

The detectors in the planar configuration were tested for variation in leakage currents as a function of bias voltage (*I-V* characteristic) using a Keithley 237 source-meter. The detector was mounted on a PCB which enabled electrical contact with the gold contacts on both the surfaces. The detector-PCB assembly was plugged in on a motherboard providing the external electrical connections. The entire assembly was housed in an electromagnetic shielded test-box. Figure 4.8 shows a *I-V* characteristic of the CZTS detector in a planar configuration. The *I-V* characteristic although symmetric in both the bias polarity regions was not linear as expected for Ohmic contacts. A ln*I* vs ln*V* plot revealed a linear characteristic up to 6-7 V followed by another linear region with different slope (~2) indicating a transition from Ohmic type to a space-charge limited current of

Mott-Gurney type [92, 93]. The leakage current at +80 V applied bias on the Te face was found to be ~1 µA whereas the same leakage current was observed with a bias of -60 V on the same surface. The slight asymmetry could be due to the presence of different surface states on the different faces of the CZTS sample. The bulk resistivity was calculated to be 0.5×10^9 Ω-cm from a low range (-1 to +1 V) *I-V* measurement as shown in the inset of Figure 4.8.

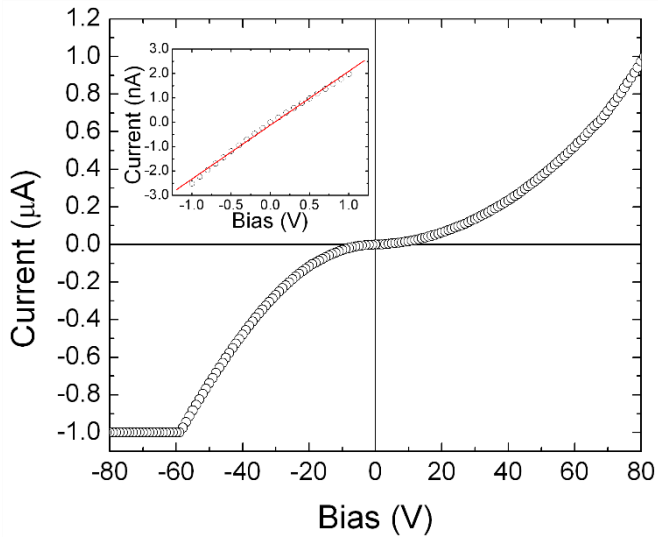

Figure 4.8: *I-V* characteristic of a CZTS planar detector. Inset shows the low range *I-V* curve with a straight-line fitting. The saturation effect beyond -60 V resulted from the compliance setting of 1 µm.

Figure 4.9 shows the measured capacitance as a function of bias voltage. The capacitance of the detector was found to be ~8.9 pF at 12 V. The C-V curve did not show much of a variation in the 0 V to +12 V range and hence the detector capacitance at an operating bias of 50 V was assumed to be of the order of few pF. The input capacitance of the A250CF is 8 pF which is why it was the most suitable for the present detector in terms of capacitance matching. A capacitance mismatch between the detector and the pre-

amplifier input capacitance is known to increase the noise of the system [94]. Despite the minimal change in capacitance with applied bias, a slight decreasing trend of the capacitor could be observed.

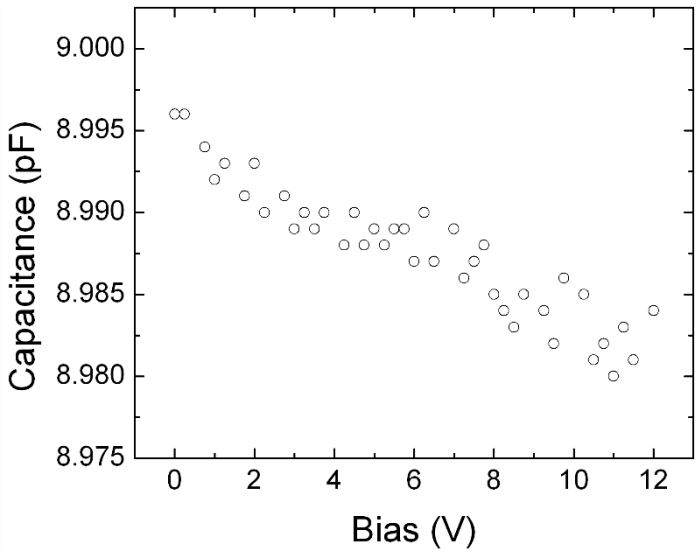

Figure 4.9: Variation of the capacitance of a planar CZTS detector as a function of bias voltage.

4.6 Radiation Measurements

4.6.1 Experimental Setup

The radiation detection testing was performed using a hybrid system that simultaneously allowed to acquire analog pulse height spectra and record digital pulses from a pre-amplifier connected to the detector. A 0.9 μCi ^{241}Am radiation source which primarily emits 5486 keV alpha particles was used for the transport property measurements and a ^{137}Cs source which emits 662 keV gamma photons was used for the gamma pulse height spectroscopy. The analog system consisted of an A250CF CoolFET charge sensitive pre-amplifier AC coupled to the detector. The charge pulses from the pre-amplifier were

fed to a shaping amplifier. The shaped pulses were digitized and binned using a Canberra Multiport II multichannel analyzer (MCA) resulting in pulse height spectra (PHS). The digital spectrometer on the other hand digitized and recorded the pre-amplifier pulses using a National Instruments PCI-5122 dual-channel fast digitizer card capable of acquiring pulses with a sampling rate of 100 MS/s and 14-bit vertical resolution. The output of the amplified signal from the shaping amplifier was used as a triggering pulse to ensure that no false triggering by noise pulses occur. Figure 4.10 (a) and (b) show the schematics of the radiation detection set-up and the detector mounting and connections inside the test box respectively. A graphical user interface was designed in the LabVIEW platform to acquire the digital pulses with the provision of controlling the data acquisition parameters like pulse duration, sampling rates, etc.

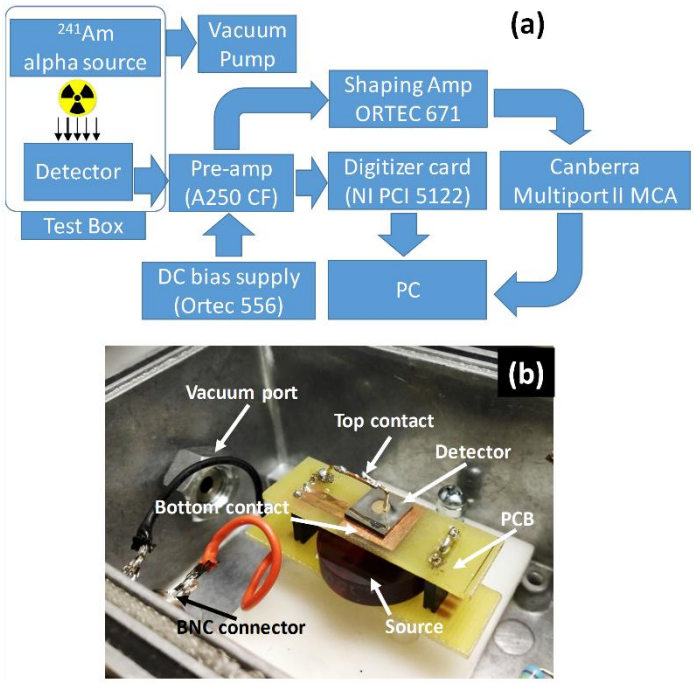

Figure 4.10: (a) A schematic of the radiation detection set-up and (b) Detector mounted on a PCB placed inside the test box along with a ^{137}Cs source.

4.6.2 Drift-Mobility Measurement

The alpha spectrometry measurements were carried out on the same planar configuration using a 0.9 μCi ^{241}Am radioactive source which emits 5486 keV alpha particles. The low penetration depth of alpha particles in CZTS ensures that the charge pairs were created just under the surface of the crystal exposed to the radiation. A data analysis program was developed using LabVIEW to digitally acquire 50000 pulses. The acquired pulses were analyzed using a data analysis program coded in LabVIEW. The program reads each pulse and determines the rise-time by calculating the time taken for the pulse to rise from 10% to 90% of the pulse-heights. A rise-time distribution was then obtained by plotting a histogram of the rise-times measured from all the pulses. The histograms followed a normal distribution. The average rise-time was calculated from the peak centroid of the Gaussian fit of the histogram. The average rise times thus obtained, were used to calculate the transit times for the charge carrier by linearly extrapolating the 80% rise times to 100%. These transit times were used for the drift-mobility calculations. The height of the pre-amplifier pulses was determined after shaping them using a digital semi-Gaussian CR-RC^4 shaping algorithm [27, 84].

Figure 4.11 shows two randomly selected charge pulses corresponding to electron (circles) and hole (squares) transits when the detector was biased at 40 V. It could be seen that the rise-times corresponding to the electron transits is faster by at least an order of magnitude compared to that of holes. Also, because of trapping and recombination, the amplitude of the hole signal is lower than that of the electrons typically by a factor of five.

The acquired rise-times of the pulses at different bias voltages were fitted into the Gaussian plot for calculating the mean transit time for each bias which is shown in Figure 4.12.

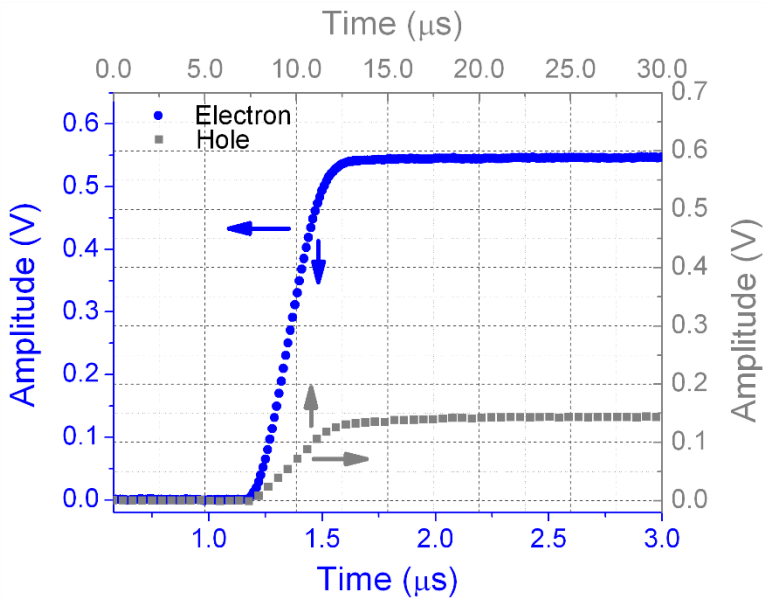

Figure 4.11: (a) Two randomly selected charge pulses corresponding to electron (circles) and hole (squares) transits when the detector was biased at 40 V.

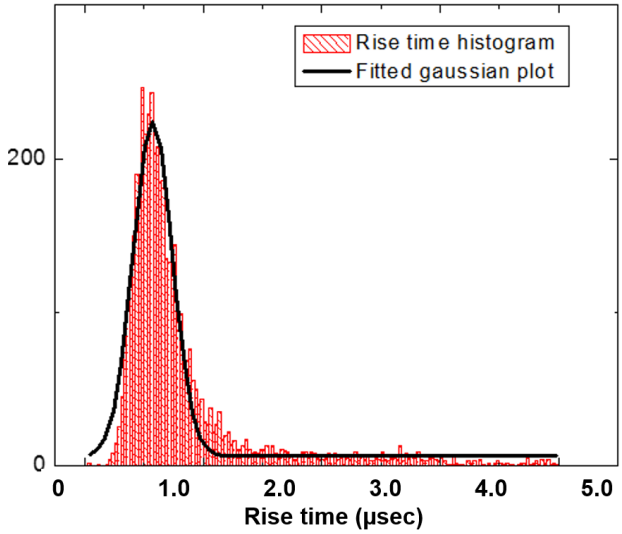

Figure 4.12: Histogram of the rise times of electron transits for +20V bias with a fitted Gaussian plot.

The relation between drift velocity (v_d) and electric field (E) can be calculated from the following equations:

$$v_d = \mu E \quad (4.1)$$

$$E = \frac{V}{d} \quad (4.2)$$

$$v_d = \frac{d}{t_r} \quad (4.3)$$

where μ is the mobility of the charge carrier, t_r is the transit time and d is the detector thickness. Therefore, from the slope of the drift velocity vs electric field plot, the mobility of the charge carrier can be calculated. The detector bias polarities were reversed to obtain the drift velocities of both the electrons and the holes. Figure 4.13 (a) and (b) show the drift velocity electric field plots for electrons and holes respectively. The drift mobility values calculated from the plots were found to be 692 $cm^2V^{-1}s^{-1}$ and 55 $cm^2V^{-1}s^{-1}$. It is noticeable that the slope changed abruptly beyond an electric field strength of 400 V/cm. This could be indicative of the field-assisted trapping. With an increase in bias voltage, the holes attain sufficient energy to be emitted from the valence band and trapped in a shallow defect level which permits detrapping at room temperature. Because of the trapping and subsequent detrapping, the holes subjected to an electric field strength of 400 V/cm and above exhibit reduced drift velocities which explains a lower drift mobility region in the mobility plot.

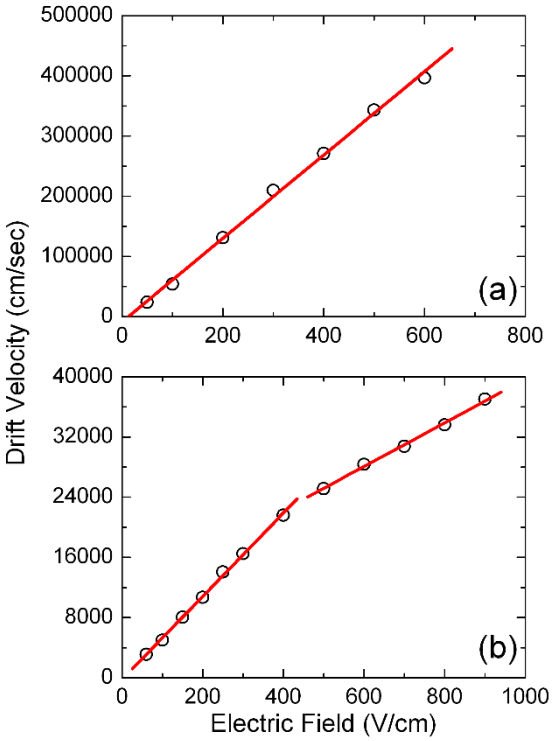

Figure 4.13: Variation of (a) electron and (b) hole drift velocities with bias voltages.

4.6.3 Mobility-Lifetime Product Measurement

For this experiment, charge pairs were created just beneath the detector surface using a low penetrating monoenergetic (5486 keV) alpha source (^{241}Am). With a proper choice of polarity on the collecting electrode, either electrons or holes can be made to drift hence producing a pure electron or hole signal. The position of the photopeak in the pulse height spectra recorded in a calibrated spectrometer gives the actual energy detected. The ratio of the actual energy detected and the full energy (5486 keV) gives the charge collection efficiency (CCE) of the detector. The CCE, denoted by Q_{CCE}, was measured as a function of bias voltages, and fitted with a single polarity Hecht equation as given below:

$$Q_{CCE} = \frac{\mu\tau V}{d^2}\left(1 - \exp\left(\frac{d^2}{\mu\tau V}\right)\right) \qquad 4.4$$

where μ is the drift mobility of either type of charge carrier, *V* is the applied bias, and *d* is the detector thickness. The mobility-lifetime product μτ of that charge carrier was obtained from the fitting parameters. The polarity of the bias voltage was then reversed to obtain the μτ product of the other charge carrier type. Figure 4.14 shows the variation of charge collection efficiency as a function of bias voltage for electrons and holes, respectively.

The μτ product for electrons was calculated to be 6.4×10^{-4} cm^2V^{-1} and that for holes was found to be 8.5×10^{-5} cm^2V^{-1}. The ratio of the μτ product of holes to electrons is ~0.13 which is significantly higher than that observed in CZT (0.03) and CdTe (0.06) [3]. Using these drift mobility values and the μτ product values, the electron and hole lifetimes were calculated to be ~1×10^{-6} s and ~1.5×10^{-6} s, respectively.

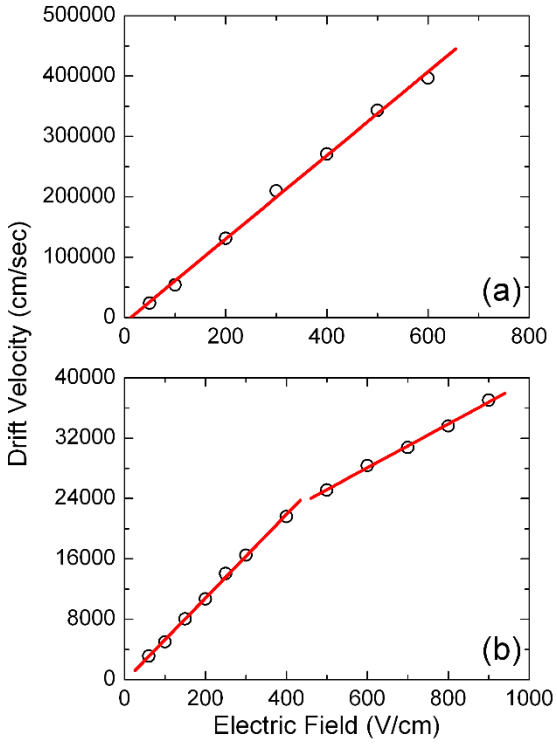

Figure 4.14: Variation of charge collection efficiency as a function of bias voltage for (a) electron transit and (b) hole transit. The solid lines show the Hecht fit plot.

4.6.4 Pulse-Height Spectroscopy

Figure 4.15 shows a gamma pulse height spectrum obtained from the CZTS detector using an analog spectrometer and a ^{137}Cs source. The 662 keV photopeak and the Compton edge were visible in the PHS. Unlike alpha particles, the interactions of the gamma photons are not restricted to a depth inside the detector. Gamma photons having the same incident energy can interact anywhere throughout the detector thickness. This causes the detector signal to be constituted of both electron and hole movements. Figure 4.16 shows a randomly selected pulse obtained from the CZTS detector exposed to the 662 keV gamma rays and resembles a typical gamma pulse obtained from detectors with widely different hole-transport property compared to that of an electron. The fast-initial rising part is due to the electronic transition and the following slower rising part corresponds to the slower hole movement. Thus, the ultimate rise-time of the pulse depends on the fraction of the signal evolution due to the hole movement. The closer the interactions of the incident gamma photon to the anode is, the higher will be the contribution of holes in the signal evolution and higher will be the rise-times. So, the rise-times of the pulses could be linked with the depth of interaction inside the planar detector. The heights of the charge pulses, measured after filtering the noise, gives the energy of the incident radiation interacting with the detector. As shown in Figure 4.15, the 662keV peak is affected by the hole trapping resulting in the bending of these events from a vertical line. This will result in longer pulse duration (higher rise time) and lower pulse-heights resulting in the bending of the correlated events with higher rise-times to the lower side of the pulse-height axis. Further investigation regarding this event is discussed in the next chapter.

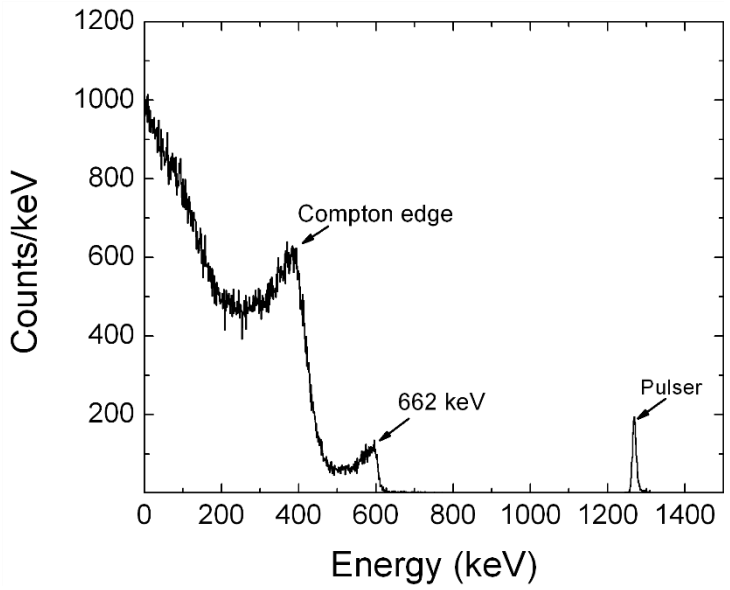

Figure 4.15: Pulse height spectrum obtained from the CZTS detector in a planar configuration. A pulser peak was recorded to monitor the energy resolution of the spectrometer.

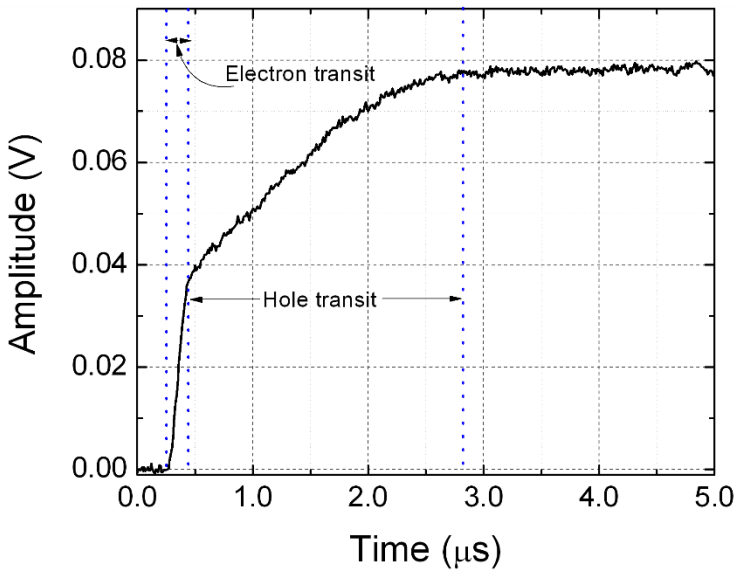

Figure 4.16: A randomly selected charge pulse from the CZTS detector exposed to 662 keV gamma-rays.

CHAPTER 5

PULSE-SHAPE ANALYSIS IN CZTS DETECTORS

5.1 Introduction

In this chapter, the results on the effect of trapping of charge carriers on the shape of the charge pulses from CZTS room temperature nuclear detectors have been presented. For a detector in the planar configuration (identical well-defined electrical contacts on either side), one can expect the induced charge to rise linearly as a function of the detector thickness, eventually equaling the actual charge created by an ionizing particle when the charges reach the collecting electrode physically. However, in a practical situation, the scenario gets complicated due to the presence of crystal deformities or defects. A charge carrier in transit may get trapped in these defects, may recombine, and maybe lost forever. A permanently trapped charge carrier deposits a partial charge on the collecting electrode, a phenomenon commonly referred to as ballistic deficit. A trapped charge might come out of the trap due to thermal excitation if the trap energy level is shallow enough and continue to drift toward the electrode. This process is commonly referred to as thermal detrapping. In this chapter a Biparametric (BP) correction scheme is discussed to evaluate the bending of 662 keV photoelectric effects. Later, a charge-trapping model that explains the pulse shapes for its entire duration from radiation detectors containing multiple defect types is developed and presented.

5.2 Ballistic Deficit in Pulse-Height Spectrum (PHS)

In the previous chapter, the pulse height spectra obtained from a planar CZTS detector exposed to the 662 keV gamma rays exhibited poor energy resolution (see Figure 5.1(a)). Gamma photons having the same incident energy can interact anywhere throughout the detector thickness. This causes the detector signal to be constituted of both electron and hole movements. Figure 5.1(b) shows a randomly selected pulse. The initial fast rising of the pulse is due to the electronic transition and the following slower rising part corresponds to the slower hole movement. Hence, the higher will be the contribution of holes in the signal evolution, and higher will be the rise-times.

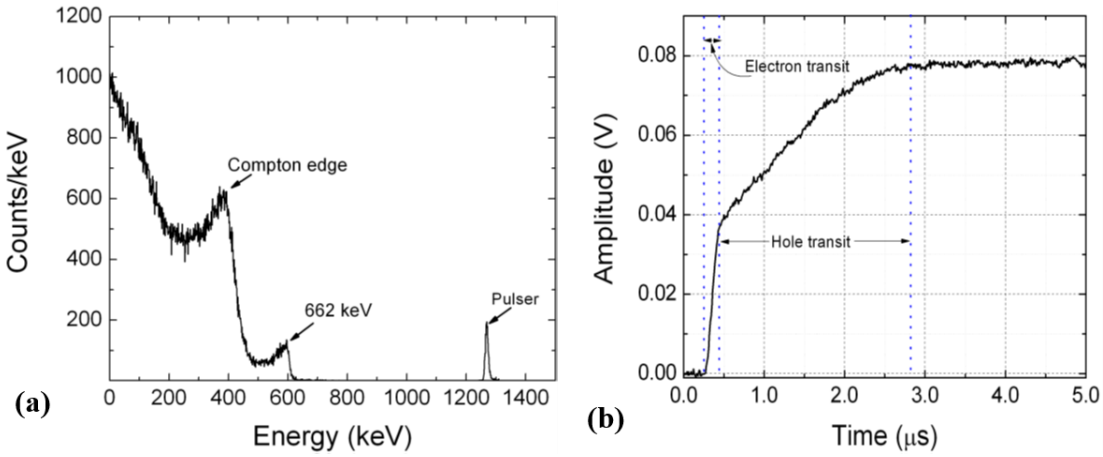

Figure 5.1: (a) Pulse height spectrum obtained from the CZTS detector in a planar configuration, and (b) a randomly selected charge pulse from CZTS detector exposed to 662 keV gamma-rays.

To investigate the correlated distribution of the rise-times and the pulse-heights, a 2D biparametric (BP) plot is presented in Figure 5.2. The bunch of events at the right-hand side of the plot corresponds to the 662 keV interacting via the photoelectric effect. These

events although very clearly distinguishable from the events due to the inelastic Compton scattering, are affected by the hole trapping resulting in the bending of these events from a vertical line expected for interactions of 662 keV photons via elastic photo-electric absorption. The events resulting from such events affected by hole trapping will result in longer pulse duration (higher rise time) and lower pulse-heights resulting in the bending of the correlated events with higher rise-times to the lower side of the pulse-height axis. The bending of the 662 keV photoelectric interactions explains the tailing of the photopeak at the lower energy side shown in Figure 5.1 (a).

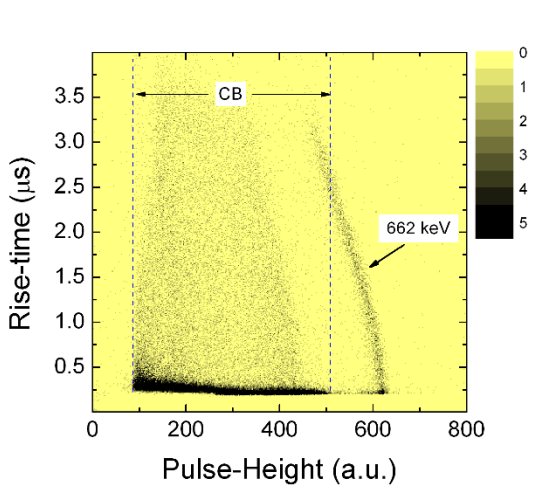

Figure 5.2: A biparametric plot obtained from the CZTS detector exposed to a ^{137}Cs source showing the bending of 662 keV photoelectric events.

More insight into the depth-dependent behavior of charge transport could be gained from the depth-dependent pulse-height spectra. Figure 5.3 shows a 3D plot of the depth dependent PHS regenerated from Figure 5.2. Ten different slices were taken out of the BP plot for a certain rise-time interval and the corresponding correlated events were projected onto the pulse-height axis to obtain the regenerated PHS. Each slice thus corresponds to a

different depth. The slices are numbered *A* through *J*. Slice *A* is the closest to cathode and *J* to the anode. It could be noticed that the 662 keV photo-peak became broader and lower as we move close to the anode. It can also be noticed that the peak centroid position shifted to almost 150 channels to the lower energy side. The photopeak was mostly constituted by the hole transits for the interactions close to the anode. The trapping of holes in defects caused ballistic deficit leading to the sliding of the peak position towards the lower energy side. Also because of the uncertainties involved with the trapping of holes transiting all the way from locations close to the anode to the cathode, the photopeak gets broadened and hence lowered. Thus, it could be observed from the slice plots that the broadening of the 662 keV photopeak was caused due to the trapping and recombination of holes.

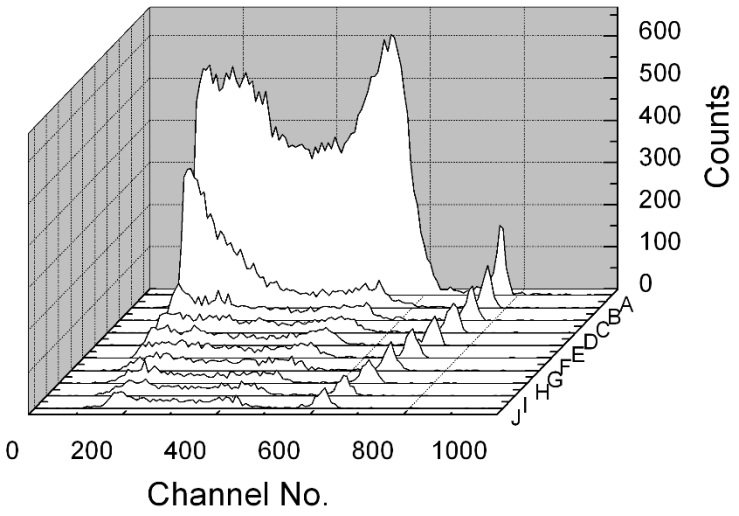

Figure 5.3: A depth-dependent pulse height spectra obtained from the BP plot presented in Figure 5.2.

From Figure 5.3, it can also be observed that the proportion of the gamma photons interacting through Compton scattering has substantially increased in slice *B* and even

more in slice *A*. This indicates that more and more photons interacted through inelastic scattering rather than depositing their full energy via elastic collision for the interactions that occurred closer to the anode. The excess interaction of gamma photons via Compton scattering is quite natural for thin (small volume) detectors.

5.3 Reconstruction of BP And PHS Plots

A digital correction is applied to the BP plot and is shown in Figure 5.4. The events which were inclined with a negative slope were selectively aligned to the 662 keV line. The corrected pulse-height spectrum regenerated from the corrected biparametric plot was shown in Figure 5.5. The quality of the pulse-height spectrum could be seen to improve remarkably with the appearance of a highly resolved and symmetric full energy photopeak corresponding to the 662 keV gamma photons. The energy resolution of the photopeak was calculated from a Gaussian fitting of the photopeak and the percentage resolution at 662 keV was found to be ~2%.

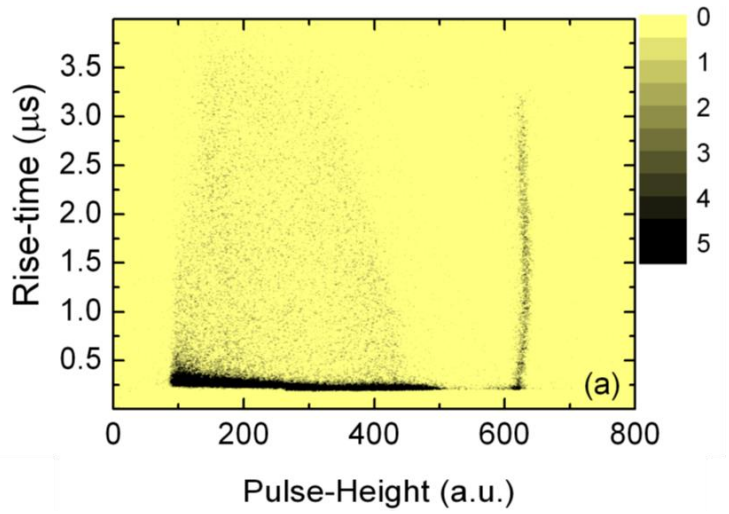

Figure 5.4: Corrected biparametric (BP) plot corresponding to Figure 5.2 shown above.

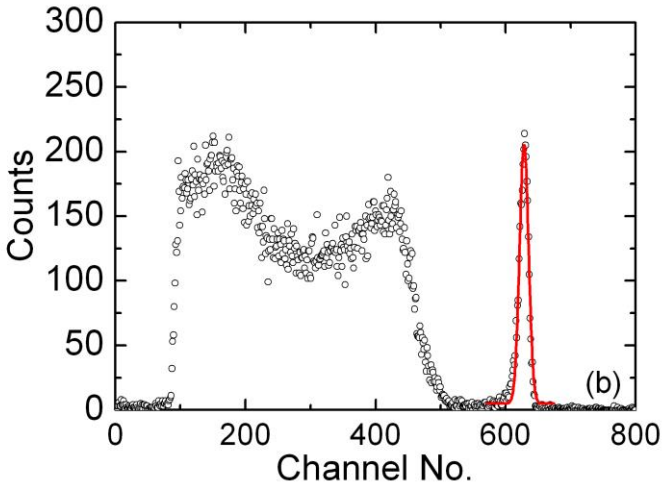

Figure 5.5: Reconstructed PHS showing the recovery of the photopeak.

5.4 Existing Charge-Trapping Model

The nature of the evolution of the charge pulse in the case of trapping and detrapping will be different from a linear function as obtained in the case of a defect-free ideal detector. Such pulse shapes have been theoretically modeled and explained by Martini and McMath [95]. This model applies to the transit of a single charge carrier with charge q_0, representing the total charge created by the incident ionization energy. This model will be referred to as a single-charge model henceforth. Figure 5.6 presents the schematics showing the evolution of charge *Q(t)* under different circumstances. Pulse 1 shows the ideal pulse when no trapping occurs. In the case of permanent trapping, the rise of the pulse gets curved and ballistic deficit causes the pulse to attenuate to reduced amplitude of q_0' as shown for pulse 2. It is worth mentioning here that the above model assumes that the trapping occurs in only one type of trapping center. The pulse shape can then be described by the piecewise equation given below:

$$Q(t) = \frac{q_0\tau_T}{t_{e,h}}\left(1 - e^{-t/\tau_T}\right) \text{ for } t \le t_{e,h} \; = \frac{q_0\tau_T}{t_{e,h}}\left(1 - e^{-t_{e,h}/\tau_T}\right) \text{ for } t > t_{e,h} \qquad 5.1$$

where, τ_T is the pre-trapping mean free drift time, i.e., the meantime a charge carrier drifts for before being trapped, and $t_{e,h}$ is the charge collection time of either electrons (subscript e) or holes (subscript h) depending on the experiment. In case detrapping occurs, the shape of the charge pulse resembles that of pulse 3 with a fast and a slow component. The fast component can be expressed as:

$$Q(t) = \frac{q_0\tau_e}{t_{e,h}}\left(\frac{t}{\tau_D} + \frac{\tau_e}{\tau_T}\left(1 - e^{-t/\tau_T}\right)\right) \text{ for } t \le t_{e,h} \qquad 5.2$$

$$\tau_e = \frac{\tau_T\tau_D}{\tau_T+\tau_D} \qquad 5.3$$

where τ_D is the mean lifetime of a trapped charge carrier before detrapping occurs.

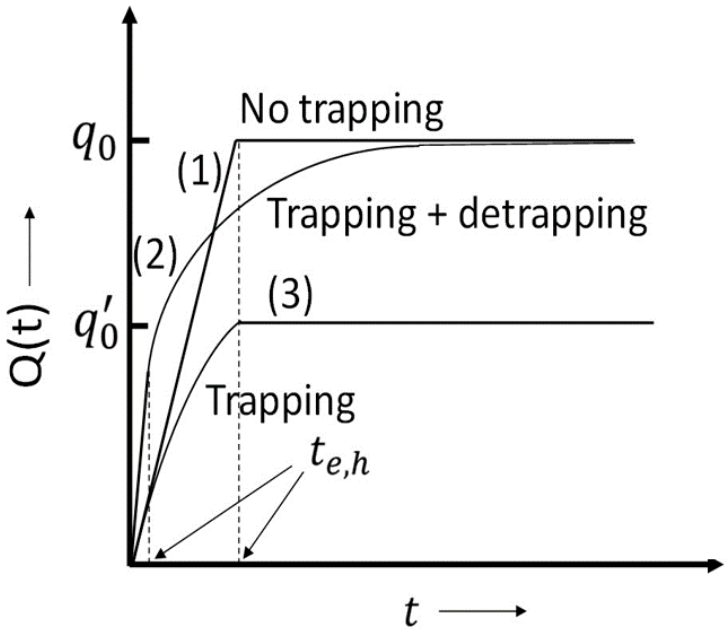

Figure 5.6: Schematic showing the pulse shape under a single charge model.

5.5 Limitations of Existing Model

The above model treats all the charge pairs collectively as a single point charge. In reality, the scenario could be completely different as numerous charge pairs are created from a single ionizing particle and the charge pulse obtained experimentally from such an event is due to the average behavior of the individual movement of each created charge particles. The model in Equation (5.2) does not provide any apparent analytic expression for the slow component for $t > t_{e,h}$ [95]. The collective charge created by the incident ionization energy is termed as q_0 and assumes that all the individual charges behave in the same fashion i.e., all of them either transits without trapping, or gets trapped, or gets trapped and then detrapped to reach the collective electrode eventually. Considering an electron-hole pair creation energy of 4.64 eV, which is the reported value for that in $Cd_{0.9}Zn_{0.1}Te$, there will be approximately 1×10^6 electrons or holes produced due to a single interaction of 5486 keV alpha particles [96]. It is quite reasonable to presume that the fate of all these charged particles will not be the same. Some of them might be permanently trapped, some will be detrapped while some might make it to the collecting electrode without being trapped at all. Therefore, the pulse shape obtained experimentally would reflect an average behavior of all these transiting charge carriers.

Figure 5.7 (a) shows such a pulse obtained from the movement of electrons with a detector biased at 6 V. It may be noted that 6 V is much lower than the operational bias voltage of 50 V for this detector. The pulse shape was fitted with the permanent trapping and detrapping model mentioned above in Equations (5.1) and (5.2). None of the models could fit the data appropriately. The black line in Figure 5.7 (a) corresponds to a function

mentioned below in Equation (5.4), which is a better fit of several possibilities tried in the present scenario.

$$y = y_0 + a\left(1 - e^{-t/b}\right) + c\left(1 - e^{-t/d}\right) \qquad 5.4$$

Here, y is the pulse height, y_0 is the offset on the y-axis and a, b, c, and d are the fitting parameters. Although the fitting in Figure 5.7 (a) appears to be better than the single-charge model, it is still not a completely satisfactory fit. Figure 5.7 (b) shows the same experimental data fitted again with Equation (5.4) except for fitting range beginning from a much later time and not from the beginning of the pulse. This resulted in a near-perfect fit. The same exercise was repeated for pulses obtained from the same detector by increasing the bias at steps. It was noticed that with the increase in bias voltage, the initial time for the fitting range had to be increased accordingly each time to obtain the best fit.

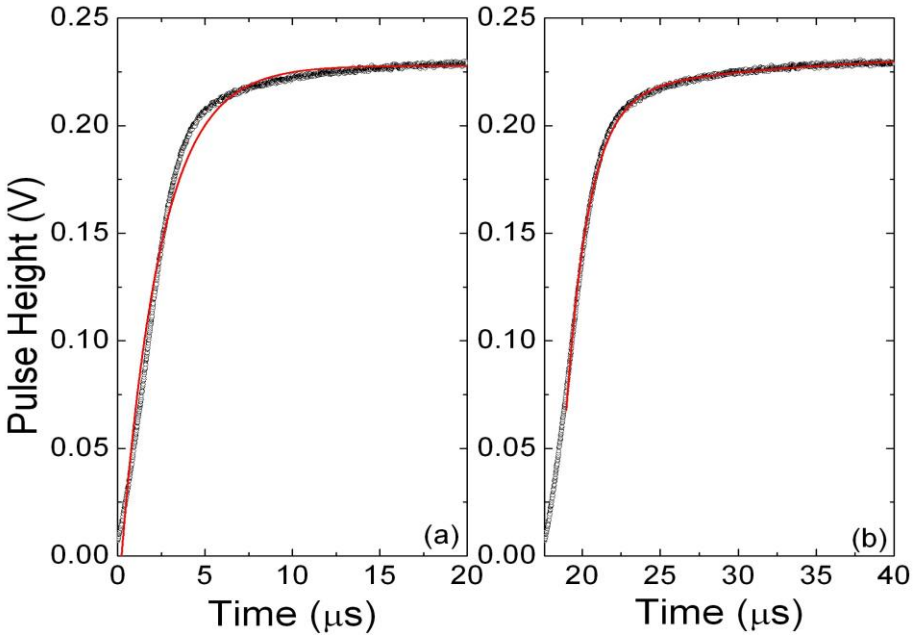

Figure 5.7: Experimentally obtained electron pulse (black line) and the fitted data (red line) for a CZTS detector biased at 6V for (a) full range fitting and (b) partial range fitting.

The dependence of the starting point of the fitting on the applied bias is summarized in Figure 5.8. The experimentally obtained pulses at different bias voltages and the corresponding fitted pulses were shown in Figure 5.8. The pre-fitting region of the pulses in the graphs was always found to be linear and has been shown as an inset in the final panel (detector biased at 50 V) with a solid line as a linear fit. As the bias voltage is increased, the drift velocity of the electrons increases, and the probability of an electron getting trapped decreases, resulting in an increase in the fraction of electrons not getting trapped which explains the increase in the duration of the linear region with bias. Figure 5.9 illustrates the above discussion which compares the charge collection from a single radiation interaction at two different bias.

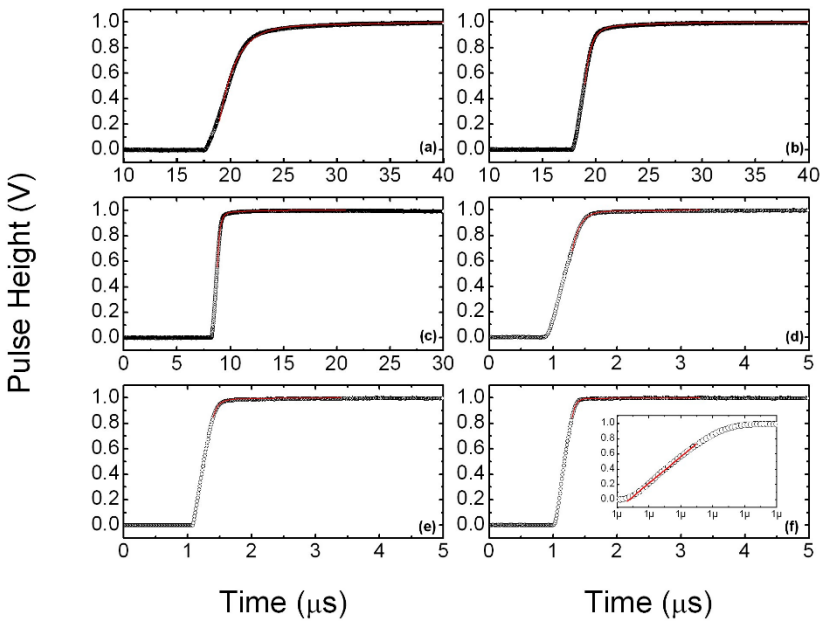

Figure 5.8: Variation of pulse shapes (open circle) along with the fitted data (solid line) as a function of time under (a) 6V, (b) 10V, (c) 20 V, (d) 30V, (e) 40V, and (f) 50 V. Each figure shows that the initial point of the fitting range has been delayed with an increase in bias to obtain the best fit. Inset in panel (f) shows the linear fit of the pre-fit (two exponential models) region. The pulse-heights were normalized to unity for ease of comparison.

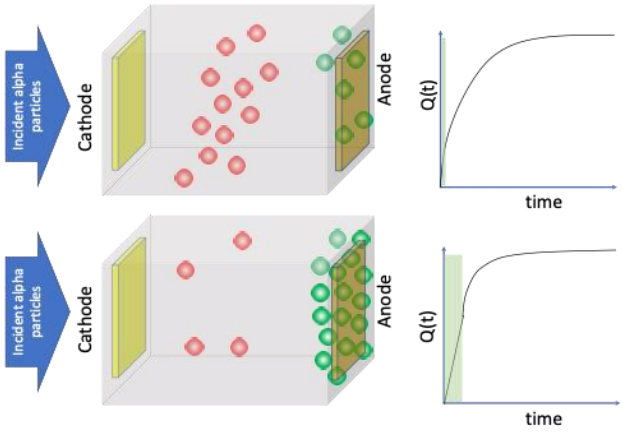

Figure 5.9: Comparison of the charge collection from a single radiation interaction at a lower bias (top) and a higher bias (bottom).

Equation 5.4 has two exponential parts which are like that in Equation 5.1. It was assumed in Equation 5.1 that the charge carriers were permanently trapped and lost in a particular type of trap center. The additional exponential term can thus be assumed to represent trapping in another type of defect. Hence, Equation 5.4 is effectively a time evolution equation of the charge pulse considering trapping in two different types of defects. However, it may not be appropriate to assume, there are only two types of trapping centers present in the sample. It rather indicates that the experimental set up can resolve the types of defect just so far.

5.6 Calculation of Mean Free Drift Time

By comparing Equation 5.1 and 5.4, the coefficients b and d can be identified as τ_{T1} and τ_{T2}, the pre-trapping mean free drift time in defect types 1 and 2 respectively. The parameters a and c can be weighting factors in charge units. The additional subscripts 1 and 2 refer to the two different types of trap centers. All the fitting parameters were set to

vary during the run. The fit returned the parameter values upon convergence. The values of τ_{T1} and τ_{T2} obtained from each pulses were used to obtain a histogram to see the distribution in these values. The average values of τ_{T1} and τ_{T2} were then calculated from the mean of the distribution. Figure 5.10 shows the variation of the average τ_{T1} and τ_{T2} values as a function of different bias voltage. Both the pre-trapping mean drift time was seen to decrease with the increase in the electric field strength, which is normal. However, the trend is not linear although the drift-time is expected to vary linearly with the electric field. It should be taken into consideration that the increase in field strength with bias not only increases the drift velocity but also increases the probability of a charge carrier not getting trapped, thereby increasing the mean free drift time. Hence, the observed variation in the pre-trapping mean drift time with bias voltage is affected by the interplay of both these effects.

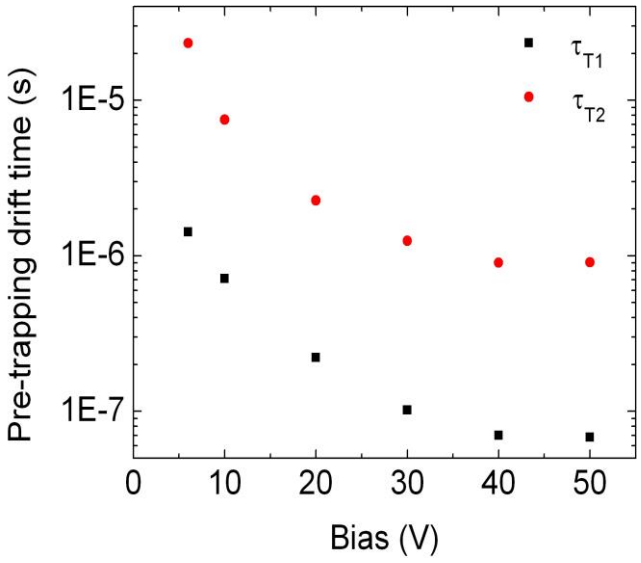

Figure 5.10: Variation of pre-trapping mean drift time of electrons as a function of bias voltage for a planar detector containing two different types of traps.

Figure 5.11 shows the variation of τ_{T1} and τ_{T2} for the case of hole movement as a function of the bias voltage. From the discussion in chapter 4, the average hole mobility-lifetime product was found to be much lower than that of electrons in these detectors. This suggests that a significantly smaller number of holes, could be collected by the collecting electrode in the lower operating bias region (< 30V). It could be observed that there is an apparent increase in the values of τ_{T1} above bias voltages of 15 V. Although it is plausible to ascribe the increase in τ_{T1} to the simple reason that the holes are moving freely for a longer duration before being trapped, the behavior can also be seen as a reduction in the difference between the τ_{T1} and τ_{T2}. The reduction in the difference can be explained as the phasing out of the effect of the defects corresponding to the time τ_{T1} with an increase in bias.

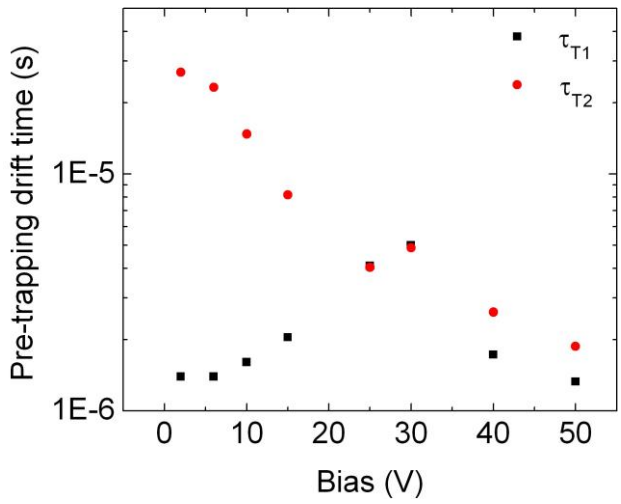

Figure 5.11: Variation of pre-trapping mean drift time of holes as a function of bias voltage for a planar detector containing two different types of traps.

5.7 Proposed Charge-Trapping Model

A piecewise continuous model, based on the movement of a large number of charge carriers rather than a single charge, has been proposed to explain the pulse shapes from planar room temperature nuclear detectors. The model is described by the following equation:

$$Q(t) = q_0 \frac{t}{t_{e,h}} \text{ for } t \leq t_f \; = \sum_i w_i q_0 \left(1 - e^{-t_{e,h_i}/\tau_{T_i}}\right) \text{ for } t > t_f \qquad 5.5$$

Here i represents each defect type that can be resolved experimentally and w_i are the corresponding weighting factors. For the present case i = 2. The time t_f in Equation 5.5 differentiates between these two regimes. The expression for $t \leq t_f$ is a linear term in time which is expected in the case of charge transit without trapping. The schematic of the pulse shape according to the model has been summarized in Figure 5.12. It may be noted that we did not explore the idea of a compact and continuous equation for the entire pulse duration. The above assumption that the initial portion of the observed charge pulses is due to the transit of the charges without being trapped is more apparent when the charge pulses due to the hole transit are observed. Figure 5.13 shows such a pulse obtained from the same detector when biased at just 2V. The fitting range according to the model (Equation 5.4), started right from the beginning of the pulse. The initial fitting range was not needed to increase until bias voltages of 30 V.

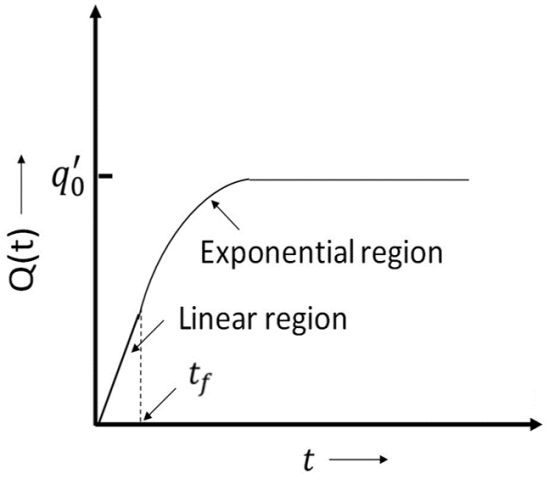

Figure 5.12: The pulse-shape under the proposed model.

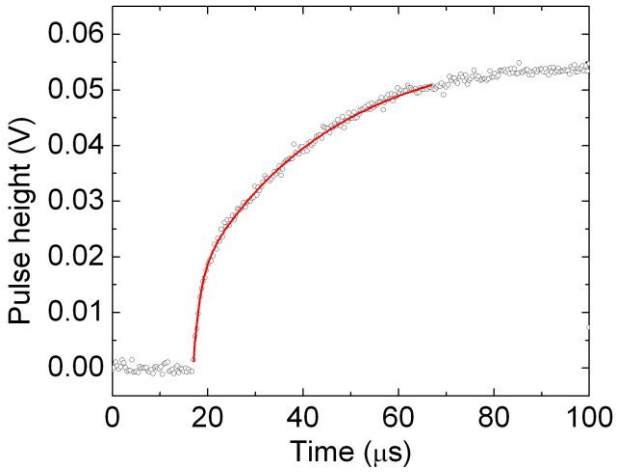

Figure 5.13: An experimentally obtained hole pulse (open circle) and the fitted data (solid line) for a CZTS detector biased at 2V.

CHAPTER 6

CONCLUSIONS, FUTURE WORK, AND BROADER SIGNIFICANCE

6.1 Conclusions

In this dissertation, a comprehensive investigation of CdZnTe (CZT) and CdZnTeSe (CZTS) for use as a room temperature gamma-ray nuclear detector was performed. At first, the advantages of using CZT as a radiation detection material were compared. Also, the potential of using another emerging material of CZTS was discussed. The successful growth of CZT, using our laboratory developed high yield modified Bridgman technique, was demonstrated. The details of pre-growth and post-growth preparations were explained. Various optical and compositional studies were performed to ensure the crystal quality. High bulk resistivity (~10^{10} Ω-cm) and high mobility-lifetime product (~10^{-2} cm^2/V) confirmed detector grade CZT. For achieving optimum performance, a 10×10 pixelated CZT detector was fabricated. The detector was examined by a ^{137}Cs gamma source and all the 100 pixels showed a well-resolved 662 keV peak with good resolution (~ 1.6%) without any charge loss correction. Besides, the tailing of the photopeak for a few pixels was explained as the transition of holes created from the radiation interactions in the active region using a Biparametric program developed at our laboratory.

The potential of a new emerging material CZTS over CZT was discussed. For the first time, the growth of $Cd_{0.9}Zn_{0.1}Te_{0.97}Se_{0.03}$ (CZTS) using a modified Bridgman technique was introduced for achieving higher yield and lower cost. The quality of the material was investigated by various optical, compositional, and electrical characterizations. It can be concluded from the investigations obtained in this dissertation that quaternary CZTS semiconductor has the potential to be a next-generation material for with significantly reduced production costs. A planar CZTS detector was fabricated and confirmed its effectiveness as a gamma-ray detector using a ^{137}Cs source. Besides, the effect of charge trapping was investigated and an energy resolution of ~2% for 662 keV gamma rays was obtained from the digitally corrected spectrum. Finally, a charge-trapping model was established that explains the pulse shapes for its entire duration from CZTS radiation detectors containing multiple defect types.

6.2 Future Work

Our future work will focus on the interaction of semiconductor-based materials specially CZT and CZTS with various radiations like x-rays and gamma-rays. Lower cost and higher yield growth processes are still under investigation due to the current high market price of these materials. In the future, identifying the optimum detector geometry as well as the front-end readout electronics for different applications for harsh environments will be very important. As CZTS is a new material, a large scope of research can be conducted on optimum Se concentrations, new growth techniques, and defect analysis for bringing this detector in the real-world applications.

6.3 Broader Significance

In 2020, the world has faced unforeseen challenges caused by the Covid-19 pandemic. A vast amount of research on treatments of patients affected by Covid-19 has been going on to reduce the mortality rate. Recently, some highly innovative trials to treat COVID-19 patients with low dose chest radiation therapy (LD-RT) are initiated [97-99]. Besides these, radiation therapy is applied to treat various life-threatening diseases like cancer, thyroid disease, blood disorders, and other noncancerous growths. Hence, the demand for developing low cost and higher resolution radiation detectors is increasing day-by-day.

We also need to acknowledge the impact of radiation detectors for other applications like high energy astrophysics, nuclear power plant monitoring, nuclear waste management, homeland security, etc. In the long run, the research will contribute to the development of public health safety, disease treatments, and the overall betterment of our human society.

REFERENCES

[1] H. B. Barber, "Applications of semiconductor detectors to nuclear medicine," *Nuclear Instruments and Methods in Physics Research Section A: Accelerators, Spectrometers, Detectors and Associated Equipment,* vol. 436, no. 1-2, pp. 102-110, 1999.

[2] L. Verger, M. Boitel, M. C. Gentet, R. Hamelin, C. Mestais, F. Mongellaz, J. Rustique, and G. Sanchez, "Characterization of CdTe and CdZnTe detectors for gamma-ray imaging applications," *Nuclear Instruments and Methods in Physics Research Section A: Accelerators, Spectrometers, Detectors and Associated Equipment,* vol. 458, no. 1-2, pp. 297-309, 2001.

[3] A. Owens, and A. Peacock, "Compound semiconductor radiation detectors," *Nuclear Instruments and Methods in Physics Research Section A: Accelerators, Spectrometers, Detectors and Associated Equipment,* vol. 531, no. 1-2, pp. 18-37, 2004.

[4] S. Del Sordo, L. Abbene, E. Caroli, A. M. Mancini, A. Zappettini, and P. Ubertini, "Progress in the development of CdTe and CdZnTe semiconductor radiation detectors for astrophysical and medical applications," *Sensors,* vol. 9, no. 5, pp. 3491-3526, 2009.

[5] U. N. Roy, G. S. Camarda, Y. Cui, R. Gul, G. Yang, J. Zazvorka, V. Dedic, J. Franc, and R. B. James, "Evaluation of CdZnTeSe as a high-quality gamma-ray

spectroscopic material with better compositional homogeneity and reduced defects," *Scientific reports,* vol. 9, no. 1, pp. 1-7, 2019.

[6] U. N. Roy, G. S. Camarda, Y. Cui, R. Gul, A. Hossain, G. Yang, J. Zazvorka, V. Dedic, J. Franc, and R. B. James, "Role of selenium addition to CdZnTe matrix for room-temperature radiation detector applications," *Scientific reports,* vol. 9, no. 1, pp. 1-7, 2019.

[7] L. Kaufman, J. Ewins, W. Rowan, K. Hosier, M. Okerlund, and D. Ortendahl, "Semiconductor gamma-cameras in nuclear medicine," *IEEE Transactions on Nuclear Science,* vol. 27, no. 3, pp. 1073-1079, 1980.

[8] S. K. Chaudhuri, R. O. Pak, K. V. Nguyen, L. Matei, V. Buliga, M. Groza, A. Burger, and K. C. Mandal, "Large Area $Cd_{0.9}Zn_{0.1}Te$ Pixelated Detector: Fabrication and Characterization," *IEEE Transactions on Nuclear Science,* vol. 61, no. 2, pp. 793-798, 2014.

[9] J. Zázvorka, J. Pekárek, R. Grill, E. Belas, K. Ridzoňová, J. Pipek, and J. Franc, "Inhomogeneous resistivity and its effect on CdZnTe-based radiation detectors operating at high radiation fluxes," *Journal of Physics D: Applied Physics,* vol. 52, no. 32, pp. 325109, 2019.

[10] E. Kim, Y. Kim, A. E. Bolotnikov, R. B. James, and K. Kim, "Detector performance and defect densities in CdZnTe after two-step annealing," *Nuclear Instruments and Methods in Physics Research Section A: Accelerators, Spectrometers, Detectors and Associated Equipment,* vol. 923, pp. 51-54, 2019.

[11] Y. Li, G. Zha, Y. Guo, S. Xi, L. Xu, and W. Jie, "Investigation on X-Ray photocurrent response of CdZnTe photon counting detectors," *Sensors*, vol. 20, no. 2, pp. 383, 2020.

[12] E. Gaubas, T. Ceponis, L. Deveikis, D. Dobrovolskas, V. Kalesinskas, J. Pavlov, V. Rumbauskas, and A. Mychko, "Spectroscopy of defects in CdZnTe structures," *Semiconductor Science and Technology*, vol. 34, no. 11, pp. 115012, 2019.

[13] T. E. Schlesinger, J. E. Toney, H. Yoon, E. Y. Lee, B. A. Brunett, L. Franks, and R. B. James, "Cadmium zinc telluride and its use as a nuclear radiation detector material," *Materials Science and Engineering: R: Reports*, vol. 32, no. 4-5, pp. 103-189, 2001.

[14] A. Hossain, A. E. Bolotnikov, G. S. Camarda, Y. Cui, R. Gul, U. N. Roy, G. Yang, and R. B. James, "Direct observation of influence of secondary-phase defects on CZT detector response," *Journal of Crystal Growth*, vol. 470, pp. 99-103, 2017.

[15] G. A. Carini, A. E. Bolotnikov, G. S. Camarda, and R. B. James, "High-resolution X-ray mapping of CdZnTe detectors," *Nuclear Instruments and Methods in Physics Research Section A: Accelerators, Spectrometers, Detectors and Associated Equipment*, vol. 579, no. 1, pp. 120-124, 2007.

[16] R. M. Krishna, S. K. Chaudhuri, K. J. Zavalla, and K. C. Mandal, "Characterization of $Cd_{0.9}Zn_{0.1}Te$ based virtual Frisch grid detectors for high energy gamma ray detection," *Nuclear Instruments and Methods in Physics Research Section A: Accelerators, Spectrometers, Detectors and Associated Equipment*, vol. 701, pp. 208-213, 2013.

[17] H. Chen, S. A. Awadalla, F. Harris, P. Lu, R. Redden, G. Bindley, A. Copete, J. Hong, J. Grindlay, and M. Amman, "Spectral response of THM grown CdZnTe crystals," *IEEE Transactions on Nuclear Science,* vol. 55, no. 3, pp. 1567-1572, 2008.

[18] T. Takahashi and S. Watanabe, "Recent progress in CdTe and CdZnTe detectors," *IEEE Transactions on Nuclear Science,* vol. 48, no. 4, pp. 950-959, 2001.

[19] J. R. Macri, L. A. Hamel, M. Julien, R. S. Miller, B. Donmez, M. L. McConnell, J. M. Ryan, and M. Widholm, "Single-sided CZT strip detectors," *IEEE Transactions on Nuclear Science,* vol. 51, no. 5, pp. 2453-2460, 2004.

[20] S. Zatschler, "Pulse-shape discrimination techniques for the COBRA double beta-decay experiment at LNGS," *Journal of Physics: Conference Series,* vol. 888, pp. 012076, 2017.

[21] J. M. Cardoso, J. B. Simoes, T. Menezes, and C. M. B. A. Correia, "CdZnTe spectra improvement through digital pulse amplitude correction using the linear sliding method," *Nuclear Instruments and Methods in Physics Research Section A: Accelerators, Spectrometers, Detectors and Associated Equipment,* vol. 505, no. 1-2, pp. 334-337, 2003.

[22] N. Auricchio, L. Amati, A. Basili, E. Caroli, A. Donati, T. Franceschini, F. Frontera, G. Landini, A. Roggio, and F. Schiavone, "Twin shaping filter techniques for compensating the signals in CZT/CdTe detectors." *2004 IEEE Symposium Conference Record,* pp. 4461-4465, 2004.

[23] L. Abbene, F. Principato, G. Gerardi, G. Benassi, N. Zambelli, A. Zappettini, M. Bettelli, P. Seller, and M. C. Veale, "Digital CZT detector system for high flux energy-resolved X-ray imaging," *2016 IEEE Symposium Conference Record*, pp. 1-7, 2016.

[24] M. Fritts, J. Tebrügge, J. Durst, J. Ebert, C. Gößling, T. Göpfert, D. Gehre, C. Hagner, N. Heidrich, and M. Homann, "Pulse-shape discrimination of surface events in CdZnTe detectors for the COBRA experiment," *Nuclear Instruments and Methods in Physics Research Section A: Accelerators, Spectrometers, Detectors and Associated Equipment*, vol. 749, pp. 27-34, 2014.

[25] E. Kamieniecki, "Effect of charge trapping on effective carrier lifetime in compound semiconductors: High resistivity CdZnTe," *Journal of Applied Physics*, vol. 116, no. 19, pp. 193702, 2014.

[26] A. E. Bolotnikov, G. De Geronimo, E. Vernon, G. Yang, G. Camarda, Y. Cui, A. Hossain, K. H. Kim, and R. B. James, "Radiation detector device for rejecting and excluding incomplete charge collection events," US Patent 9335423B2, May 10, 2016.

[27] S. K. Chaudhuri, K. J. Zavalla, R. M. Krishna, and K. C. Mandal, "Biparametric analyses of charge trapping in $Cd_{0.9}Zn_{0.1}Te$ based virtual Frisch grid detectors," *Journal of Applied Physics*, vol. 113, no. 7, pp. 074504, 2013.

[28] O. Frisch, *British Atomic Energy Report BR-49;* Harwell, UK, 1944.

[29] A. E. Bolotnikov, S. Babalola, G. S. Camarda, Y. Cui, S. Egarievwe, P. Fochuk, R. Hawrami, A. Hossain, J. James, I. Nakonechnyi, G. Yang, and R. B. James,

"Spectral responses of virtual Frisch-grid CdZnTe detectors and their relation to IR microscopy and X-ray diffraction topography data," *Proc SPIE*, vol. 7079, 2008.

[30] A. Göök, F. J. Hambsch, A. Oberstedt, and S. Oberstedt, "Application of the Shockley–Ramo theorem on the grid inefficiency of Frisch grid ionization chambers," *Nuclear Instruments and Methods in Physics Research Section A: Accelerators, Spectrometers, Detectors and Associated Equipment*, vol. 664, no. 1, pp. 289-293, 2012.

[31] Q. Zhang, C. Zhang, Y. Lu, K. Yang, and Q. Ren, "Progress in the development of CdZnTe unipolar detectors for different anode geometries and data corrections," *Sensors (Basel, Switzerland)*, vol. 13, no. 2, pp. 2447-2474, 2013.

[32] L. Ocampo Giraldo, A. E. Bolotnikov, G. S. Camarda, G. De Geronimo, J. Fried, D. Hodges, A. Hossain, E. Vernon, and R. B. James, "A linear array of position-sensitive virtual Frisch-grid CdZnTe for low-energy gamma rays," *Nuclear Instruments and Methods in Physics Research Section A: Accelerators, Spectrometers, Detectors and Associated Equipment*, vol. 903, pp. 204-214, 2018.

[33] A. E. Bolotnikov, G. S. Camarda, G. D. Geronimo, J. Fried, D. Hodges, A. Hossain, K. Kim, G. Mahler, L. O. Giraldo, E. Vernon, G. Yang, and R. B. James, "A 4×4 array module of position-sensitive virtual Frisch-grid CdZnTe detectors for gamma-ray imaging spectrometers," *Nuclear Instruments and Methods in Physics Research Section A: Accelerators, Spectrometers, Detectors and Associated Equipment*, vol. 954, pp. 161036, 2020.

[34] Y. Kim, T. Lee, and W. Lee, “Radiation measurement and imaging using 3D position sensitive pixelated CZT detector,” *Nuclear Engineering and Technology*, vol. 51, no. 5, pp. 1417-1427, 2019.

[35] D. Goodman, M. Streicher, Y. Zhu, S. Brown, and Z. He, “1-D fast neutron source localization using digital pixelated 3-D position-sensitive CdZnTe detectors,” *IEEE Transactions on Nuclear Science*, vol. 64, no. 9, pp. 2531-2535, 2017.

[36] A. E. Bolotnikov, G. S. Camarda, Y. Cui, G. De Geronimo, J. Eger, A. Emerick, J. Fried, A. Hossain, U. Roy, C. Salwen, S. Soldner, E. Vernon, G. Yang, and R. B. James, “Use of high-granularity CdZnTe pixelated detectors to correct response non-uniformities caused by defects in crystals,” *Nuclear Instruments and Methods in Physics Research Section A: Accelerators, Spectrometers, Detectors and Associated Equipment*, vol. 805, pp. 41-54, 2016.

[37] G. Montemont, M. C. Gentet, O. Monnet, J. Rustique, and L. Verger, “Simulation and design of orthogonal capacitive strip CdZnTe detectors,” *IEEE Transactions on Nuclear Science*, vol. 54, pp. 854-859, 2007.

[38] M. Sajjad, J. W. Kleppinger, and K. C. Mandal, "Crystal growth, characterization, and fabrication of $Cd_{0.9}Zn_{0.1}Te$ monolithic pixelated detectors for high-energy gamma-ray," *Proc. SPIE*, vol. 1114, pp. 111141T-1-12, 2019.

[39] P. Luke, “Single-polarity charge sensing in ionization detectors using coplanar electrodes,” *Applied Physics Letters*, vol. 65, pp. 2884-2886, 1994.

[40] P. N. Luke, “Unipolar charge sensing with coplanar electrodes-application to semiconductor detectors,” *IEEE Transactions on Nuclear Science,* vol. 42, no. 4, pp. 207-213, 1995.

[41] D. Maneuski, V. Gostilo, and A. Owens, “TCAD simulation studies of novel geometries for CZT ring-drift detectors,” *Journal of Physics D: Applied Physics,* vol. 53, no. 1, pp. 015114, 2019.

[42] A. Owens, R. den Hartog, F. Quarati, V. Gostilo, V. Kondratjev, A. Loupilov, A. G. Kozorezov, J. K. Wigmore, A. Webb, and E. Welter, “Hard x-ray response of a CdZnTe ring-drift detector,” *Journal of Applied Physics,* vol. 102, no. 5, pp. 054505, 2007.

[43] S. Hwang, H. Yu, A. E. Bolotnikov, R. B. James, and K. Kim, “Anomalous Te inclusion size and distribution in CdZnTeSe,” *IEEE Transactions on Nuclear Science,* vol. 66, no. 11, pp. 2329-2332, 2019.

[44] A. Yakimov, D. Smith, J. Choi, and S. Araujo, "Growth and characterization of detector-grade CdZnTeSe by horizontal Bridgman technique," *Proc. SPIE,* vol. 11114, pp. 111141N, 2019.

[45] M. Harrison, A. Graebner, W. McNeil, and D. McGregor, “Carbon coating of fused silica ampoules,” *Journal of Crystal Growth,* vol. 290, pp. 597-601, 2006.

[46] K. C. Mandal, S. H. Kang, M. Choi, A. Kargar, M. Harrison, D. McGregor, A. E. Bolotnikov, G. A. Carini, G. S. Camarda, and R. B. James, “Characterization of Low-defect $Cd_{0.9}Zn_{0.1}Te$ and CdTe crystals for high-Performance Frisch collar detectors,” *IEEE Transactions on Nuclear Science,* vol. 54, pp. 802-806, 2007.

[47] R. Pak, and K. Mandal, "Defect levels in nuclear detector grade $Cd_{0.9}$ $Zn_{0.1}$Te crystals," *ECS Journal of Solid State Science and Technology,* vol. 5, pp. P3037-P3040, 2016.

[48] A. Burger, D. O. Henderson, S. H. Morgan, J. Feng, and E. Silberman, "Purification of selenium by zone refining," *Journal of Crystal Growth,* vol. 106, no. 1, pp. 34-37, 1990.

[49] F. P. Doty, J. F. Butler, J. F. Schetzina, and K. A. Bowers, "Properties of CdZnTe crystals grown by a high pressure Bridgman method," *Journal of Vacuum Science & Technology B: Microelectronics and Nanometer Structures Processing, Measurement, and Phenomena,* vol. 10, no. 4, pp. 1418-1422, 1992.

[50] L. G. Casagrande, D. Di Marzio, M. B. Lee, D. J. Larson, M. Dudley, and T. Fanning, "Vertical Bridgman growth and characterization of large-diameter single-crystal CdTe," *Journal of Crystal Growth,* vol. 128, no. 1, Part 2, pp. 576-581, 1993.

[51] K. Y. Lay, D. Nichols, S. McDevitt, B. E. Dean, and C. J. Johnson, "High quality, single crystal CdTe grown by a modified horizontal Bridgman technique," *Journal of Crystal Growth,* vol. 86, no. 1, pp. 118-126, 1988.

[52] Q. Li, W. Jie, L. Fu, T. Wang, G. Yang, X. Bai, and G. Zha, "Optical and electrical properties of indium-doped $Cd_{0.9}Zn_{0.1}$Te crystal," *Journal of Crystal Growth,* vol. 295, no. 2, pp. 124-128, 2006.

[53] K. C. Mandal, S. H. Kang, M. Choi, J. Bello, L. Zheng, H. Zhang, M. Groza, U. N. Roy, A. Burger, G. E. Jellison, D. E. Holcomb, G. W. Wright, and J. A. Williams,

"Simulation, modeling, and crystal growth of $Cd_{0.9}Zn_{0.1}Te$ for nuclear spectrometers," *Journal of Electronic Materials,* vol. 35, no. 6, pp. 1251-1256, 2006.

[54] I. Jung, H. Krawczynski, A. Burger, M. Guo, and M. Groza, "Detailed studies of pixelated CZT detectors grown with the modified horizontal Bridgman method," *Astroparticle Physics,* vol. 28, no. 4, pp. 397-408, 2007.

[55] S. Csaba, B. Derek, G. Joseph, Jr., L. S. Gary, B. Michael, and E. John, "Fabrication of high-performance CdZnTe quasi-hemispherical gamma-ray CAPture plus detectors." *Proc. SPIE,* vol. 6319, pp. 6319-1-9, 2006.

[56] J. R. Heffelfinger, D. L. Medlin, and R. B. James, "Analysis of grain boundaries, twin boundaries and Te precipitates in $Cd_{1-x}Zn_xTe$ grown by high-pressure Bridgman method," *MRS Proc.*, vol. 484, pp. 247, 1997.

[57] T. Asahi, O. Oda, Y. Taniguchi, and A. Koyama, "Growth and characterization of 100 mm diameter CdZnTe single crystals by the vertical gradient freezing method," *Journal of Crystal Growth,* vol. 161, no. 1, pp. 20-27, 1996.

[58] J. Franc, P. Moravec, P. Hlídek, E. Belas, P. Höschl, R. Grill, and Z. Šourek, "Development of inclusion-free CdZnTe substrates from crystals grown by the vertical-gradient freeze method," *Journal of Electronic Materials,* vol. 32, no. 7, pp. 761-765, 2003.

[59] U. N. Roy, A. Burger, and R. B. James, "Growth of CdZnTe crystals by the traveling heater method," *Journal of Crystal Growth,* vol. 379, pp. 57-62, 2013.

[60] R. Triboulet, “Fundamentals of the CdTe and CdZnTe bulk growth,” *physica status solidi (c),* vol. 2, no. 5, pp. 1556-1565, 2005.

[61] A. Zappettini, M. Zha, L. Marchini, D. Calestani, R. Mosca, E. Gombia, L. Zanotti, M. Zanichelli, M. Pavesi, N. Auricchio, and E. Caroli, "Boron oxide encapsulated vertical Bridgman grown CdZnTe crystals as X-ray detector material." *2008 IEEE Nuclear Science Symposium Conference Record*, pp. 118-121, 2008.

[62] "FactSage 7.2 - list of stored phase diagrams (6100)," C. f. R. i. C. Thermochemistry, ed., 2020.

[63] J. Greenberg, “P-T-X phase equilibrium and vapor pressure scanning of non-stoichiometry in CdTe,” *Journal of Crystal Growth,* vol. 161, pp. 1-11, 04/01, 1996.

[64] A. El Mokri, R. Triboulet, A. Lusson, A. Tromson-Carli, and G. Didier, “Growth of large, high purity, low cost, uniform CdZnTe crystals by the “cold travelling heater method”,” *Journal of Crystal Growth,* vol. 138, no. 1, pp. 168-174, 1994.

[65] J. Peterson, M. Fiederle, and J. Derby, “Analysis of the traveling heater method for the growth of cadmium telluride,” *Journal of Crystal Growth,* vol. 454, 2016.

[66] Y. Wang, K. Kudo, Y. Inatomi, R. Ji, and T. Motegi, “Growth interface of CdZnTe grown from Te solution with THM technique under static magnetic field,” *Journal of Crystal Growth,* vol. 284, pp. 406-411, 2005.

[67] H. Chen, S. Awadalla, K. Iniewski, P. Lu, F. Harris, J. Mackenzie, T. Hasanen, W. Chen, R. Redden, G. Bindley, I. Kuvvetli, C. budtz-jørgensen, P. Luke, M. Amman, J. Lee, A. E. Bolotnikov, G. S. Camarda, Y. Cui, A. Hossain, and R. B. James,

"Characterization of large cadmium zinc telluride crystals grown by traveling heater method," *Journal of Applied Physics*, vol. 103, pp. 014903-014903, 2008.

[68] P. Rudolph, *Handbook of Crystal Growth*: Elsevier, 2015.

[69] R. M. Krishna, T. C. Hayes, P. G. Muzykov, and K. C. Mandal, "Low temperature crystal growth and characterization of $Cd_{0.9}Zn_{0.1}Te$ for radiation detection applications," *MRS Proc.*, vol. 1341, pp. 39-44, 2011.

[70] M. Zha, F. Bissoli, A. Zappettini, G. Zuccalli, L. Zanotti, and C. Paorici, "Heat treatment in semi-closed ampoule for obtaining stoichiometrically controlled cadmium telluride," *Journal of Crystal Growth*, vol. 237-239, pp. 1720-1725, 2002.

[71] J. P. Ponpon, "A review of ohmic and rectifying contacts on cadmium telluride," *Solid-State Electronics*, vol. 28, no. 7, pp. 689-706, 1985.

[72] H. Cordes, and R. Schmid-Fetzer, "The role of interfacial reactions in Pt/CdTe contact formation," *Semiconductor Science and Technology*, vol. 9, no. 11, pp. 2085-2096, 1994.

[73] H. Cordes, and R. Schmid-Fetzer, "Electrical properties and contact metallurgy of elemental (Cu, Ag, Au, Ni) and compound contacts on p-$Cd_{0.95}Zn_{0.05}Te$," *Semiconductor Science and Technology*, vol. 10, no. 1, pp. 77-86, 1995.

[74] A. E. Bolotnikov, G. S. Camarda, G. A. Carini, Y. Cui, L. Li, and R. B. James, "Cumulative effects of Te precipitates in CdZnTe radiation detectors," *Nuclear Instruments and Methods in Physics Research Section A: Accelerators, Spectrometers, Detectors and Associated Equipment*, vol. 571, no. 3, pp. 687-698, 2007.

[75] P. J. Sellin, A. W. Davies, S. Gkoumas, A. Lohstroh, M. E. Özsan, J. Parkin, V. Perumal, G. Prekas, and M. Veale, "Ion beam induced charge imaging of charge transport in CdTe and CdZnTe," *Nuclear Instruments and Methods in Physics Research Section B: Beam Interactions with Materials and Atoms,* vol. 266, no. 8, pp. 1300-1306, 2008.

[76] W. J. Danaher, L. E. Lyons, M. Marychurch, and G. C. Morris, "Chemical etching of crystal and thin film cadmium telluride," *Applied Surface Science,* vol. 27, no. 3, pp. 338-354, 1986.

[77] H. S. White, A. J. Ricco, and M. S. Wrighton, "Characterization of p-type cadmium telluride electrodes in acetonitrile/electrolyte solutions. Nearly ideal behavior from reductive surface pretreatments," *The Journal of Physical Chemistry,* vol. 87, no. 25, pp. 5140-5150, 1983.

[78] B. R. Strohmeier, "Zinc Aluminate ($ZnAl_2O_4$) by XPS," *Surface Science Spectra,* vol. 3, no. 2, pp. 128-134, 1994.

[79] D. W. Langer, and C. J. Vesely, "Electronic Core Levels of Zinc Chalcogenides," *Physical Review B,* vol. 2, no. 12, pp. 4885-4892, 1970.

[80] A. J. Ricco, H. S. White, and M. S. Wrighton, "X-ray photoelectron and Auger electron spectroscopic study of the CdTe surface resulting from various surface pretreatments: Correlation of photoelectrochemical and capacitance-potential behavior with surface chemical composition," *Journal of Vacuum Science & Technology A,* vol. 2, no. 2, pp. 910-915, 1984.

[81] Z. He, "Review of the Shockley–Ramo theorem and its application in semiconductor gamma-ray detectors," *Nuclear Instruments and Methods in Physics Research Section A: Accelerators, Spectrometers, Detectors and Associated Equipment,* vol. 463, no. 1, pp. 250-267, 2001.

[82] S. K. Chaudhuri, M. Sajjad, and K. C. Mandal, "Pulse-shape analysis in $Cd_{0.9}Zn_{0.1}Te_{0.98}Se_{0.02}$ room-temperature radiation detectors," Applied Physics Letters, vol. 116, no. 16, pp. 162107, 2020.

[83] H. H. Barrett, J. D. Eskin, and H. B. Barber, "Charge transport in arrays of semiconductor gamma-ray detectors," *Physical Review Letters,* vol. 75, no. 1, pp. 156-159, 1995.

[84] M. Nakhostin, "Recursive algorithms for real-time digital (CR)-$(RC)^n$ pulse shaping," *IEEE Transactions on Nuclear Science,* vol. 58, no. 5, pp. 2378-2381, 2011.

[85] Y. Yin, X. Chen, H. Wu, S. Komarov, A. Garson, Q. Li, Q. Guo, H. Krawczynski, L. Meng, and Y. Tai, "3-D spatial resolution of 350 /spl mu/m pitch pixelated CdZnTe detectors for imaging applications," *IEEE Transactions on Nuclear Science,* vol. 60, no. 1, pp. 9-15, 2013.

[86] S. K. Chaudhuri, R. Krishna, K. Zavalla, L. Matei, V. Buliga, M. Groza, A. Burger, and K. C. Mandal, "$Cd_{0.9}Zn_{0.1}Te$ crystal growth and fabrication of large volume single-polarity charge sensing gamma detectors," *IEEE Transactions on Nuclear Science,* vol. 60, no. 4, pp. 2853, 2013.

[87] B. Thomas, M. C. Veale, M. D. Wilson, P. Seller, A. Schneider, and K. Iniewski, "Characterisation of Redlen high-flux CdZnTe," *Journal of Instrumentation,* vol. 12, no. 12, pp. C12045-C12045, 2017.

[88] M. Prokesch, S. A. Soldner, and A. G. Sundaram, "CdZnTe detectors for gamma spectroscopy and x-ray photon counting at 250 × 106 photons/(mm^2 s)," *Journal of Applied Physics,* vol. 124, no. 4, 2018.

[89] M. Shenasa, S. Sainkar, and D. Lichtman, "XPS study of some selected selenium compounds," *Journal of Electron Spectroscopy and Related Phenomena,* vol. 40, no. 4, pp. 329-337, 1986.

[90] M. Polak, "X-ray photoelectron spectroscopic studies of $CdSe_{0.65}Te_{0.35}$," *Journal of Electron Spectroscopy and Related Phenomena,* vol. 28, no. 2, pp. 171-176, 1982.

[91] E. T. Yu, M. C. Phillips, J. O. McCaldin, and T. C. McGill, "Measurement of the CdSe/ZnTe valence band offset by x-ray photoelectron spectroscopy," *Journal of Vacuum Science & Technology B: Microelectronics and Nanometer Structures Processing, Measurement, and Phenomena,* vol. 9, no. 4, pp. 2233-2237, 1991.

[92] L. Pauling, "Electronic Processes in Ionic Crystals. By N. F. Mott and R. W. Gurney," *The Journal of Physical Chemistry,* vol. 45, no. 7, pp. 1142-1142, 1941.

[93] M. A. Lampert, "Simplified theory of space-charge-limited currents in an insulator with traps," *Physical Review,* vol. 103, no. 6, pp. 1648-1656, 1956.

[94] V. Radeka, "Low-noise techniques in detectors," *Annual Review of Nuclear and Particle Science,* vol. 38, no. 1, pp. 217-277, 1988.

[95] M. Martini, and T. A. McMath, "Trapping and detrapping effects in lithium-drifted germanium and silicon detectors," *Nuclear Instruments and Methods,* vol. 79, no. 2, pp. 259-276, 1970.

[96] A. Owens, and A. Peacock, "Compound semiconductor radiation detectors," *Nuclear Instruments and Methods in Physics Research Section A: Accelerators, Spectrometers, Detectors and Associated Equipment,* vol. 531, no. 1, pp. 18-37, 2004.

[97] F. Rödel, M. Arenas, O. J. Ott, C. Fournier, A. G. Georgakilas, S. Tapio, K.-R. Trott, and U. S. Gaipl, "Low-dose radiation therapy for COVID-19 pneumopathy: what is the evidence?," *Strahlentherapie und Onkologie*, 2020/05/09, 2020.

[98] C. Kirkby, and M. Mackenzie, "Is low dose radiation therapy a potential treatment for COVID-19 pneumonia?," *Radiotherapy and oncology : journal of the European Society for Therapeutic Radiology and Oncology*, pp. S0167-8140(20)30185-7, 2020.

[99] A. Kefayat, and F. Ghahremani, "Low dose radiation therapy for COVID-19 pneumonia: A double-edged sword," *Radiotherapy and oncology : journal of the European Society for Therapeutic Radiology and Oncology*, pp. S0167-8140(20)30207-3, 2020.